Analytical Investigation of Gas Production from Methane Hydrates upon Thermal Stimulation

by

Mohammad Roostaie

A thesis
presented to the University of Waterloo
in fulfillment of the
thesis requirement for the degree of
Master of Science
in
Earth Sciences

Waterloo, Ontario, Canada, 2020

AUTHOR'S DECLARATION

I hereby declare that I am the sole author of this thesis. This is a true copy of the thesis, including any required final revisions, as accepted by my examiners.

I understand that my thesis may be made electronically available to the public.

Abstract

In this study, analytical models are developed to investigate methane hydrate dissociation in porous media upon thermal stimulation employing wellbore heating. This work investigates how the wellbore's external and internal structure affect the dissociation process. The models are based on both Radial (2D) and Cartesian coordinates (1D) to couple the wellbore heating process and the associated methane response in the hydrate dissociation in the reservoir. Different types of heat-sources are studied: i) a flat heat-source in the 1D cases with a constant temperature; ii) line heat-source in radial cases with a constant temperature; iii) wellbore heat-source in radial cases, employing both a constant temperature and a coaxial wellbore. Wellbore's external layers consist of casing, gravel, and cement. In the coaxial wellbore heat-source, both conduction and convection heat transfers are considered. It consists of an inner tube and an outer structure (casing, gravel, and cement layers).

The analytical solution employed a similarity solution, in which a moving boundary to separate the dissociated (containing produced gas and water) and undissociated (containing only methane hydrate) zones is assumed, to model the dissociation in the reservoir. Two different operating schemes have been studied for water inlet of the coaxial wellbore heat-source: i) inner tube; and ii) annulus section of the wellbore.

The results of temperature distribution along the wellbore (for the coaxial heat-source), temperature and pressure distributions in the reservoir, hydrate dissociation rate, and energy efficiency considering various initial and boundary conditions and reservoir properties are presented and compared with those of the previous studies. Direct heat transfer from the heat source to the reservoir in the case with a line heat-source higher dissociation rate and gas production compared to those of the wellbore-heat-source models, considering the heat conduction in the wellbore thickness causes. Decreasing the heat-source pressure and increasing its temperature increases the dissociation rate and gas production. Employing them simultaneously also increases gas production but reduces energy efficiency.

The wellbore thickness affects the energy efficiency of the process negatively. The two different operating schemes affect the process in almost the same way with slightly higher gas production in the case with annulus hot-water inlet because the annulus is in direct

contact with the reservoir. Increasing the inlet water temperature and decreasing the wellbore pressure simultaneously results in a greater gas production and energy efficiency. Porosity, thermal diffusivity, thermal conductivity, and thickness of the reservoir have direct relation with the dissociation rate, but the permeability and gas viscosity of reservoir almost do not impact the process. The wellbore parameters, such as water flow rate, inlet temperature, and wellbore radius except the inner tube radius, directly impact the wellbore mean temperature and the dissociation process.

The findings of this study make a major contribution to research on methane hydrate dissociation upon thermal stimulation with wellbore heating by analytically demonstrating, for the first time, how the wellbore structure affect the process.

Acknowledgements

First of all, I want to express my most appreciation to Professor Yuri Leonenko for providing me the opportunity to perform this investigation and for all his support and understanding throughout my study, which made this time to be a professional and personal growth period.

I also greatly appreciate the time, meticulous editorial input, and scientific guidance contributed by my committee members, Professor Maurice Dusseault and Professor André Unger.

Finally, I must express my very profound sense of gratitude to my family for providing me with unfailing support and continuous encouragement throughout my study and research. This accomplishment would not have been possible without them. The completion of this research and thesis has been assisted by many people. Thank you.

I would like to acknowledge the financial supports for this research, provided by the Natural Science and Engineering Research Council (NSERC) of Canada, University of Waterloo Graduate Entrance Scholarships, and University of Waterloo Graduate Student Bursary.

Dedication

I dedicated this to my family whom I am truly grateful having in my life. Also to my friends.

Table of Contents

List of Figures

List of Tables

Chapter 1
Introduction

Some parts of the thesis are published in two journals: i) the Journal of Petroleum Science and Engineering (Roostaie and Leonenko 2019b) with DOI: 10.1016/j.petrol.2019.106505 and License: CC-BY-NC-ND; and ii) the Energy Journal (Roostaie and Leonenko 2019a) with DOI: 10.1016/j.energy.2019.116815 and License: CC-BY-NC-ND. This thesis has resulted in another paper (Roostaie and Leonenko 2020) (arXiv preprint: arXiv:2001.04900) and submitted to the Energy Conversion and Management Journal.

1.1 Methane hydrates

Methane hydrates (MH) are cage-like substances in which a large amount of gas molecules is trapped by crystalline water molecules. Gas hydrates contain about 170 to 180 std m^3 natural gas/m^3 hydrate (Kamath and Godbole 1987). The high pressure and low temperature underground with sufficient methane gas induce the MH formation (Davie and Buffett 2001). The estimation of the volume of the gas hydrates exceeds the whole volume of conventional gas resources worldwide (Englezos 1993; Makogon 1981). However, considering the hydrates as a reliable source of energy depends on the availability of hydrates and the cost of gas production process from them.

1.2 MH classification

Natural hydrate deposits can be divided into four main classes (Li et al. 2016c): i) class 1 deposits include two layers of the hydrate and an underlying two-phase fluid (mobile gas and liquid water) zone; ii) class 2 deposits include a hydrate layer underlain by a zone of mobile water; iii) class 3 deposits include only a hydrate layer, without mobile fluid zones (usually between a low-permeability overburden and an under-burden); and iv) class 4 deposits that are oceanic hydrates without confining boundaries, also they have a very low gas production potential.

1.3 MH reservoirs in Canadian regions

MH reservoirs are mainly formed beneath the permafrost in arctic regions and in marine shelf sediments due to the appropriate pressure and temperature conditions (Collett 2001). Collet et al. (Collett 1999) reported the existence of MH reservoirs with a thickness of approximately 113 m in different intervals from 897.25 m to 1109.8 m depth in Mallik site, located in Mackenzie Delta, Northwest Territories, Canada. They reported that in an area of 1 km^2 around the drilling site in the Mallik field, between 2.93×10^9 and 4.15×10^9 m^3 of gas exist. Some other properties for Mallik field, which are reported by Moridis et al. (Moridis et al. 2004), are as follows: i) porosity (ϕ) about 0.28; ii) intrinsic permeability (k) of about 2×10^{-14} m^2; iii) composite thermal conductivity of the rock hydrate reservoir fluids system of about 1.5 W/m$^\circ$C; iv) rock specific heat of about 800 J/kg$^\circ$C; and v) hydrate specific heat of about 1600 J/kg$^\circ$C. They also mentioned that the best time for performance of field tests in Malik site is in the winter, since the ice roads can be built in order to access the site. This time period is about 4-6 weeks, so the operation time in Arctic conditions would be less than 30 days.

Majorowicz et al. (Majorowicz and Osadetz 2001) studied the regions with gas production potential from MH reservoirs in the vast continental shelves and Arctic permafrost of Canada. They revealed the existence of 10^{10}-10^{12} m^3 of gas hydrates in these regions with an associated methane gas potential in the range of 10^{12}-10^{14} m^3. The volume distribution of methane gas in MH reservoirs in Canada are geographically as follows: i) 0.24–8.7×10^{13} m^3 in the Mackenzie Delta–the Beaufort Sea; ii) 0.19–6.2×10^{14} m^3 in the Arctic Archipelago; iii) 1.9–7.8×10^{13} m^3 on the Atlantic margin; and iv) 0.32–2.4×10^{13} m^3 on the Pacific margin. The total in-situ amount of methane gas trapped in MH reservoirs of Canada is estimated to be 0.44–8.1×10^{14} m^3, while the conventional Canadian in-situ hydrocarbon gas resource is approximately 0.27×10^{14} m^3. The minimum hydrate depth in Canada is 0.2 km. Some measurements related to Majorowicz et al. (Majorowicz and Osadetz 2001) work: i) The gas hydrate maximum stability depth is up to 1.4 and 1.8 km in the Mackenzie delta-Beaufort Sea and in the Arctic Archipelago, respectively; ii) The gas hydrate inferred area in the Mackenzie delta–Beaufort Sea field is estimated to be approximately 125,000 km^2, where the

hydrate stability thickness is between 0.2 km and 1.4 km; iii) In the Arctic Archipelago, the total hydrate inferred area is estimated to be 770,000 km^2, which has a mean thickness of 65 m; iv) The area of stability of MH on the Atlantic margin is estimated to be 400,000 km^2, where the mean thickness of hydrates is estimated to be 79 m; and v) The hydrate stability area in the Pacific offshore is approximately 30,000 km^2, and the average hydrates thickness that has concentrations in pores in the range of 10% to 35% is around 110 m.

Judge (Judge 1982) reported that the eastern part of the Mackenzie Delta, including Richards Island and the Tuktoyaktuk Peninsula, has the greatest MH reservoir's depth. He also represented the depth range of potential hydrate resource of the northern areas as shown in Table 1.

Table 1. Depth range of methane hydrates in Arctic regions. (Judge 1982)

Area	Minimum depth (m)	Maximum depth (m)	Thickness of hydrate zone (m)
Arctic Islands (Western)	140	1100	960
Arctic Islands (Eastern)	140	960	820
Sverdrup Basin	140	1270	1130
Arctic Platform	140	1400	1260
Mackenzie Delta (Eastern)	190	1860	1670
Mackenzie Delta (Western)	340	730	390
Mackenzie Valley and Yukon Territory	-	-	-

1.4 MH dissociation methods

Considering that the entrapped gas and water are bonded through physical interaction in MH, which is weaker than the chemical interactions, any change in MH equilibrium temperature or pressure would easily induce MH instability and dissociation. Main methods of MH

dissociation that have been reported so far are as follows (Feng et al. 2015; Li et al. 2016c): i) thermal stimulation by increasing the temperature of the reservoir above the equilibrium temperature (Fitzgerald et al. 2012; Li et al. 2011b); ii) depressurization by decreasing the pressure inside the MH reservoir below the equilibrium pressure of the hydrate (Ji et al. 2001; Yousif et al. 1990); iii) depressurization in conjunction with thermal stimulation that is reported to have a better efficiency compared to the two previous methods (Wang et al. 2014b); iv) inhibitor injection by injecting fluids, such as methanol, that will induce instability of the MH formation (Sung et al. 2002; Yousif 1996). Compared to depressurization and thermal stimulation methods, there are fewer studies in the field of chemical inhibitors (Ross and Toczylkin 1992); and v) replacement of methane by CO_2 in MH reservoirs, which also helps global warming and climate change mitigations (Khlebnikov et al. 2016; Maruyama et al. 2012; Nishikawa et al. 1992; Saji et al. 1992; Yuan et al. 2012). Despite several findings regarding the hydrate dissociation methods, further investigation is required to shed more light on the potential of different methods and their aspects.

Figure 1 shows a schematic of the temperature and pressure changes during depressurization (A-B-C-D), thermal stimulation (A-E-F), depressurization in conjunction with thermal stimulation (A-B-C-G) (the black line in this figure displays the boundary between stable and unstable zones of the hydrate).

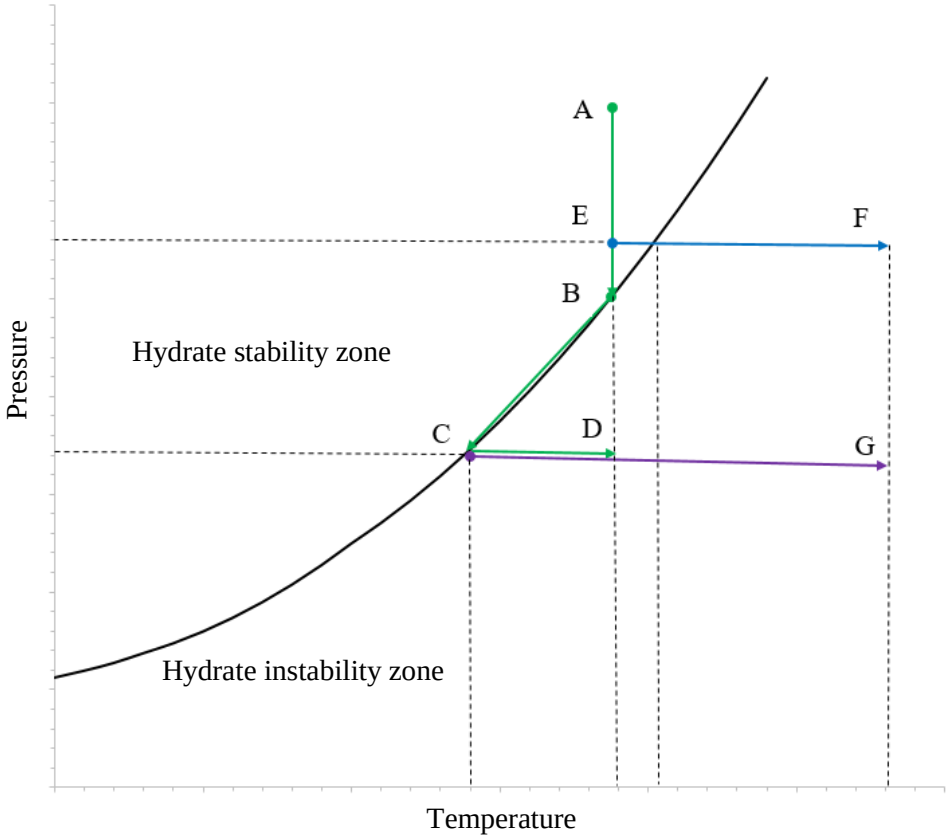

Figure 1. Schematic of depressurization, thermal stimulation, and depressurization in conjunction with thermal stimulation methods.

In the depressurization method, due to the endothermic reaction of hydrate dissociation, the process adsorbs heat from the overburden/underburden and the surrounding undissociated hydrate, and it may stop as the temperature of the reservoir drops to the equilibrium temperature of the local pressure. Hence, the appropriate heat transfer or existence of a heat source is important (Chen et al. 2014). The diffusion of pressure, the hydrate saturation, and effective permeability are the factors affecting the dissociation in depressurization method (Chen et al. 2010).

There are different ways for increasing the temperature of the reservoir in the thermal stimulation method, including hot water circulation, wellbore heating (Li et al. 2010), and hot water huff and puff (Li et al. 2012a), electrical heating, microwave radiation, etc. Hot water/steam circulation and wellbore heating are common ways of thermal stimulation

method (Moridis and Reagan 2007). Hot water/steam circulation process consists of two wells: i) the inner one for hot water/steam injection; and ii) the outer one for gas/water production (Moridis and Reagan 2007). In the wellbore heating case, only the wellbore is heated using hot water/steam, electrical or other methods (Moridis and Reagan 2007). The huff and puff method can be described as three sections: i) hot water injection in the reservoir (huff); then ii) stopping for a time to transfer the heat to the hydrate (soak); and iii) producing gas and water from the well (puff) (Li et al. 2012a).

1.5 Environmental effects of MH

Another important aspect of methane hydrates is their influence on the environment and vice versa. The main environmental challenges for the methane hydrates could be continental margin sediment instability caused by the dissociation of hydrate deposits and the global warming induced by a large amount of CH4 released from methane hydrates (TREHU 2006). It should be mentioned that greenhouse effect of CH_4 is about 25 times more than CO_2 (STOCKER et al. 2013), so the methane release from hydrates is a positive feedback to the global warming issue, which accelerates the hydrate dissociation and methane emission. The researches on MH revealed that the oceanic hydrates in seafloor and sediments are dynamic, and the decomposition of these hydrates could be a reason for global warming (Reeburgh 2007). Also, the seismic activities (earthquakes) and volcanic activities could induce instability in the methane hydrate reservoirs (Fischer et al. 2013). The abovementioned assumptions has not been proved yet, because there is not any real report or evidence of the effects of hydrates and environment on each other (Ruppel and Kessler 2017).

1.6 Research background

1.6.1 Mathematical studies

There have been many mathematical studies of hydrate dissociation employing both analytical and numerical methods. Analytical solutions provide fast answers with a better mechanistic understanding of the phenomena. However, numerical methods are more comprehensive and complicated, requiring fewer assumptions. In 1982, a 3D numerical

model consisting of an MH layer with a free gas zone was developed to study MH dissociation upon depressurization by considering the effect of conduction heat transfer and gas flow (Holder and Angert 1982). In 1986, this work was extended by considering the effect of the water flow produced during the dissociation (Burshears et al. 1986). In 1991, a numerical model investigated MH dissociation by depressurization in porous media with gas-water flow considering three phases of water, gas, and MH without the effect of heat transfer (Yousif et al. 1991). Then, the previous work was extended by taking into account the water-gas flow and convective-conductive heat transfer (Masuda 1997; MASUDA 1999). MH dissociation upon thermal stimulation was simulated by assuming an impermeable moving dissociation boundary, which separates the dissociated and undissociated zones, and considering different media permeabilities (Tsypkin 2000). Another numerical work by employing finite difference method and considering the effect of heat transfer in depressurization method showed that the process is a function of well pressure (Ahmadi et al. 2004). In the same year, TOUGH2 simulator, which is capable of simulation of different dissociation methods considering four components and up to nine phases in either kinetic or equilibrium models, was employed to show the possibility of gas production from MH using both depressurization and thermal stimulation (Moridis 2002). Results retrieved from TOUGH2 showed the feasibility of gas production from MH reservoirs in in the Mackenzie Delta, Northwest Territories, Canada, upon depressurization and thermal stimulation with higher efficiencies achieved by using both methods together (Moridis et al. 2004). Another numerical work reported that the kinetic reaction models should be taken into account in order to avoid under-prediction of recoverable MH, while, requiring more computational effort compared to the equilibrium reaction models (Kowalsky and Moridis 2007). A numerical work using TOUGH-Fx/HYDRATE simulator showed low gas production upon depressurization with high amount of water production from disperse oceanic MH reservoirs with low hydrate saturation (Moridis and Sloan 2007).

In 1990, Selim et al. (Selim and Sloan 1990) investigated MH dissociation upon thermal stimulation by using an analytical 1D model by assuming a moving dissociation boundary. They also studied the effect of gas convection heat transfer and its flow, while assuming the

produced water to remain motionless in the pores. In 1982, a study on hydrate dissociation upon both thermal stimulation using hot water injection and depressurization by employing two models (the frontal-sweep model, and the fracture-flow model) was performed (McGuire 1982). The results showed that the depressurization is more feasible compared to thermal stimulation. Makogon (Makogon 1997) provided analytical expressions for the temperature and pressure distributions during MH dissociation upon depressurization including the effect of the throttling process in the energy equation and assuming a moving dissociation boundary. This work was extended by considering the water and gas movement and similarity solutions for temperature and pressure (Tsypkin 2001). In 2001, another model was generated based on Makogon's model (Ji et al. 2001) including the heat conduction. An analytical work using depressurization reported that the effect of the gas-water two-phase flow on MH dissociation is smaller than the effect of heat transfer and the intrinsic kinetics of MH decomposition (Hong et al. 2003). Recently, an analytical work was designed based on experimental conditions (i.e., the reservoir was assumed to be finite, and there was heat transfer from outside of the reservoir into the hydrate zone) to study the MH dissociation by depressurization, thermal stimulation, and the combination of both methods (Wang et al. 2015).

1.6.2 Experimental studies

In the experimental investigations on MH dissociation upon different methods, the size of the setup significantly affects the outcome of tests and is reported as one of the major challenges in experimental works (Wang et al. 2016c). For instance, the scale of the experiment's setup determines the main involving mechanism in the hydrate dissociation in porous media (Wang et al. 2016c), which is one of the followings: i) heat transfer in the decomposing zone; ii) the intrinsic kinetics of hydrate decomposition; or iii) the multiphase flow (i.e., gas-water flow) during gas production (Hong et al. 2003). Tang et al. (Tang et al. 2007) showed that the determining factor in the core-scale experiments is the intrinsic kinetics of hydrate decomposition; while, in larger scale experiments or field works, the controlling mechanism is heat transfer in the decomposing zone. An experimental work showed that MH dissociation using thermal stimulation is a moving boundary ablation process in a 3D cubic

hydrate simulator (CHS) (Li et al. 2011b). Li et al. (Li et al. 2012b) employed two hydrate simulators with different scales to experimentally investigate the MH dissociation upon depressurization. They reported that the gas production period is longer for the larger scale simulator. Conduction heat transfer was shown to be the main mechanism for heat transfer to the dissociating zone in an experimental work on MH dissociation (Zhao et al. 2012). Wang et al. (Wang et al. 2016c) by employing a 3D Pilot-Scale Hydrate Simulator (PHS) reported that ice formation in pores during MH dissociation below the quadruple point in the sandy sediment increases the dissociation rate. Another experimental work studied the dissociation of water-saturated hydrate samples using a pilot-scale hydrate simulator via different methods and reported that depressurization in conjunction with thermal stimulation is the optimum method (Wang et al. 2018). Nowadays, this field of investigation has attracted the researchers' interest to perform more mathematical studies as well as real field or experimental works or employing parameters from real reservoirs (Chen and Hartman 2018; Konno et al. 2017; Mardani et al. 2018; Wang et al. 2019b; Wang et al. 2016b; Zhao et al. 2016).

1.6.3 Field works

Researchers have performed field trials on different hydrate reservoirs based on the experimental and numerical works to study the gas production. In the following, some of the field tests are presented.

1.6.3.1 Messoyakha field test

Messoyakha gas hydrate resources is located in the Arctic on the eastern border of West Siberia, Russia, with the area of about 19.5×12 km, which is consisted of a free gas zone overlaid by a hydrate layer and underlain by an unknown aquifer. The first field gas production test carried out in Messoyakha was in 1969–1970 (Makogon and Omelchenko 2013). Since 1969–2011, many field tests were carried out by depressurization as the main method. The initial gas for production before the beginning of the field development in the area could be up to 36×10^9 m^3, which 24×10^9 m^3 of that could be in the free gas phase, and up to $9–12\times10^9$ m^3 in hydrate phase. It is reported that at the end of 2011, the totally

accumulative gas produced from the field was 12.9×10^9 m^3, which 5.4×10^9 m^3 of that was obtained upon hydrate decomposition. 48×10^3 m^3 water was produced of which 45×10^6 m^3 was due to hydrate decomposition.

1.6.3.2 Mallik field test

The Mallik gas hydrate field are located at the northeastern edge of Mackenzie Delta, Canada. The gas hydrates exist within a sequence of Tertiary sediments underlain by over 600 m of permafrost. During 1971–1972, the discovery step was performed by drilling a discovery well, then, the consortium of Canada, Japan, and U.S was formed to perform the first research well program in 1998. It was found that there are discrete gas hydrate layers distributed in different depths from around 890 to 1106 m, which is approximately 110 m in total thickness. Also, the measurements revealed that the hydrate saturation exceeds 80% in some cases ranking Malik field among the most concentrated gas hydrate reservoirs in the world. From December 2001 to March 2002, the consortium completed a production research well program by drilling a main production research well with the depth of 1200 m and nearby two wells for science observation (Dallimore 2002). They studied production state using depressurization and thermal stimulation methods. Another field test was performed in April 2007 and March 2008 by the consortium of Canada and Japan using depressurization (Kurihara et al. 2010). It should be mentioned that the produced gas was accumulated at the top of the casing for the irregular (on–off) pumping and was not transferred directly to the surface probably due to the excessive sand production. The biggest issue, in 2007 winter test, was the sand production, which caused significant reduction of the pumping efficiency, besides the gas and water production. The only purpose of the 2008 winter test was to perform gas production for a longer time. The winter test lasted 6 days during which the gas and water production were approximately 13000 m^3 and 70 m^3, respectively. In addition, Compared to the 2007 winter test, in 2008 winter test, the produced sands were prevented from flowing into the wellbore by a screen, and the produced gas and water were transferred directly to the surface. It was found that the water production was far lower than that estimated amount probably due to the reverse flow of a large amount of water from the injection zone to wellhead when the pump was idle during the test. The pump efficiency was

also lower compared to the estimation. The main issue in 2008 winter test was the well suffering from the collapsed and/or deformed conduits with high permeability created in 2007 winter test.

1.6.3.3 Mount Elbert field test

The Alaska North Slope (ANS) is reported to contain a large amount of methane hydrates. U.S. Geological Survey (USGS) reported that technically, around 2.4 tcm (trillion cubic meters) gas could be produced from the ANS gas hydrates (Moridis et al. 2011). During February 3-19, 2007, the test well was drilled within the ANS Milne Point Unit (MPU). BP Exploration (Alaska), Inc. (BPXA) and the U.S. Department of Energy (DOE) co-sponsored the project as part of a Cooperative Research Agreement (CRA) since 2001. The study results estimated that up to 0.34 tcm gas could be technically produced from total 0.92 tcm gas-in-place within Eileen gas hydrate reservoir, near the industry infrastructure ANS MPU, Prudho Bay Unit (PBU), and Kuparuk River Unit (KRU) area (Collett 2008). Finally, the USGS selected ‘‘Mount Elbert” site for drilling a test well. The analysis of the acquired data showed that the high saturation gas hydrates occur with mobile formation water in this site. In the Mount Elbert site, the depressurization was shown to be the possible gas production method for the future field work test.

1.6.3.4 Ignik Sikumi field tests

Ignik Sikumi field is also located in the ANS within the Eileen gas hydrate reservoir region. The CO_2–CH_4 replacement in hydrate was used in the gas production process (Hauge et al. 2014; Schoderbek et al. 2013). In 2011, a 792.5 m well was logged at the Ignik Sikumi site. The tests were continued to 2012. The injection lasted for 14 days during which a total of 6.1 metric standard cubic meter (MSm^3) of fluid (liquefied CO_2/N_2) was injected into the reservoir, and 4.7 MSm^3 of N_2 and 1.4 MSm^3 of CO_2 were injected at the end of the injection. The production process was divided into two parts of unassisted flow-back and assisted flow-back, depending on the bottom-hole pressure, the assisted flow-back was also divided into another three phases (Hauge et al. 2014). Finally, total 24 MSm^3 CH_4 was produced, 70% and 40% of the injected N_2 and CO_2 were recovered, the remaining 60%

injected CO_2 stayed in the hydrate reservoir. There were total of 180 m^3 produced water. Total 11.1 m^3 of sands were produced. Ignik Sikumi field test was the first trial of gas production using CO_2–CH_4 replacement method, and CH_4 was successfully produced.

1.6.3.5 QTPP production trial

During 2008–2013, the China Geological Survey (CGS) conducted some gas hydrae scientific drillings in the South Syncline of the Juhugeng mine in the QTPP. The depressurization in conjunction with thermal stimulation was employed as the production method, and a single vertical well system was considered as the well configuration (Wang et al. 2014a). The average gas production rate was around 30 m^3/day for 3.5 days by depressurization method. The thermal stimulation is not suitable for gas production from hydrate reservoirs with low hydrate saturation in the QTPP due to the low heat conductivity, and the production by depressurization is the optimal choice for the next field production (Sun et al. 2014).

1.6.3.6 Nankai Trough field test

In 2013, JOGMEC and National Institute of Advanced Industrial Science and Technology (AIST) carried out the first field test in naturally marine gas hydrate deposits in Nankai Trough with the funding support from the Ministry of Economy, Trade and Industry (MEIT) of Japan (Yamamoto 2015). A single well system was considered as the well configuration. The flow test was very short, started on March 12, 2013, and ended on March 18, 2013, because of the sand production. More than 30 m^3 of produced sand filled the bottom production hole, made the downhole production device disabled. After 6 days production, the total produced CH_4 was approximately 119,500 m^3. It should be mentioned that the gas production rate was larger than that estimated by numerical simulations.

1.7 Thesis objectives

Studies over the past decades have provided substantial information about MH dissociation and the associated consequences in the reservoirs. However, it should be noted that the wellbore structure can affect the process, such as the heat transfer mechanism during thermal

stimulation method. Furthermore, data from several studies suggest that the wellbores in the production region mainly consisted of three layers: casing, cement, and gravel (Florez Anaya and Osorio 2014; Pucknell and Mason 1992; Xu et al. 2014). The analytical works conducted about the hydrate dissociation to present (Li et al. 2010; Li et al. 2012a; Wan et al. 2018; Zhao et al. 2016) have not considered the impact of wellbore geometry and the associated structure (i.e., wellbore radius and the associated outer layers) on MH dissociation upon thermal stimulation by wellbore heating, which might induce unreliability while comparing to experiments or field works.

In investigations related to geothermal energy, ground-source heat pumps are employed as a heat source/sink to derive heat transfer process to/from underground (Beier et al. 2013; Holmberg et al. 2016; Phirani et al. 2009; Sun et al. 2017; Wang et al. 2016a). Heat pumps come in two types (Lamarche et al. 2010): i) Coaxial boreholes heat exchangers; and ii) U-tube heat exchangers. These heat exchangers do not inject water directly into reservoirs, but rather they indirectly transfer heat through both their own and the wellbore's structure. The coaxial boreholes heat exchangers have been used and investigated since decades ago (Braud et al. 1983; Mei and Fischer 1983; Morita et al. 1992). They also have higher efficiencies in terms of heat transfer to the reservoir compared to those of U-tube heat exchangers (Hellström 1998, 2002; Yavuzturk and Chiasson 2002). It should also be noted that employing radial coordinates, the mechanism and operational schemes of wellbore heating in the previous analytical studies of thermal stimulation have not been treated. These assumptions make the outcomes closer to the real operational conditions.

The present study aims to address the mentioned gaps in the field of MH dissociation upon wellbore heating by modeling analytically: 1) a semi-infinite 1D hydrate reservoir in Cartesian coordinates using a flat heat source considering three main layers: casing, cement, and gravel; 2) a raidal infinite hydrate reservoir in radial coordinates considering two different heat sources: i) line heat source (no thickness); and ii) wellbore heat source consists of three main completion layers of casing, cement, and gravel; and 3) a radial infinite hydrate reservoir in the radial coordinates considering a coaxial heat exchanger with an inside tube

and a surrounding annulus heat source as the heat source, through which the hot water is injected. Three main completion outside layers -the casing, cement, and gravel- of the wellbore are also considered. Different operating schemes of the heat exchanger (e.g., hot water injection into the inner tube or annulus) and reservoir characteristics are also studied. The energy efficiency, gas production, and temperature and pressure distributions are calculated and verified against the previous experimental and mathematical studies.

The results of this study, for the first time, provides an important opportunity to advance the understanding of the effect of wellbore's structure, composition, and performance on the gas production from MH reservoirs upon thermal stimulation. Furthermore, the heat-source operational schemes (i.e., the coaxial heat-source) and the inside thermal interactions are coupled to MH dissociation in the reservoir. Thus, the present work facilitates further and more concise optimization and analysis on the heat-source to improve gas production form MH and the associated energy efficiency. Therefore, the findings should make an important contribution to the field of gas production from MH reservoirs by providing the outcomes obtained using conditions that are closer to the real-condition tests, which make them more valuable and reliable.

Chapter 2
Modeling method

Some parts of the thesis are published in two journals: i) the Journal of Petroleum Science and Engineering (Roostaie and Leonenko 2019b) with DOI: 10.1016/j.petrol.2019.106505 and License: CC-BY-NC-ND; and ii) the Energy Journal (Roostaie and Leonenko 2019a) with DOI: 10.1016/j.energy.2019.116815 and License: CC-BY-NC-ND. This thesis has resulted in another paper (Roostaie and Leonenko 2020) (arXiv preprint: arXiv:2001.04900) and submitted to the Energy Conversion and Management Journal.

2.1 One-dimensional MH dissociation in Cartesian coordinates using a flat heat source

Figure 1 shows a schematic of hydrate dissociation using thermal stimulation method in the proposed 1D flat case. It should be mentioned that the reservoir is semi-infinite, and L denotes the overall well thickness including, cement, gravel, and casing layers. The fundamental steps of MH dissociation are as follows: in the beginning of the process, the reservoir with the porosity of ϕ is filled with MH in equilibrium conditions with initial temperature T_0. At time $t = 0$, the temperature of the heat source at $x = 0$, increases to a new temperature of T_i , which is above the equilibrium temperature of the hydrate, and is kept constant during the process. Subsequently, MH starts dissociating and a sharp moving boundary surface is created as shown by dashed lines in Figure 1, indicating the rate of hydrate dissociation and separates the water and gas produced in the dissociated zone (Zone I) from the un-dissociated zone (Zone II). The temperature of the dissociated zone is higher than the temperature in the hydrate zone inducing heat conduction from the dissociated zone to the hydrate zone and hydrate dissociation. The rate of hydrate dissociation is determined by the speed of moving interface, which decreases as the process continues and the dissociated zone thickens. Actually, it consumes a larger part of input heat to increase the temperature of the matrix material in the dissociated zone as well as the produced water and gas at the dissociation front as the dissociation interface moves forward. The remaining input energy is consumed for hydrate dissociation and temperature increase of the matrix materials

in Zone II. As shown in Figure 2, the temperature and pressure distributions in Zone I (T_I and P) are respectively $T_s < T_I < T_i$ and $P_i < P < P_s$, and in Zone II, the temperature distribution is $T_0 < T_{II} < T_s$ and the pressure is in the equilibrium condition of the hydrate. The dissociation interface is shown by the dashed line and the associated pressure and temperature change due to time. It should be noted that T_I at the outer surface of the well changes with time, but it is always lower than T_i.

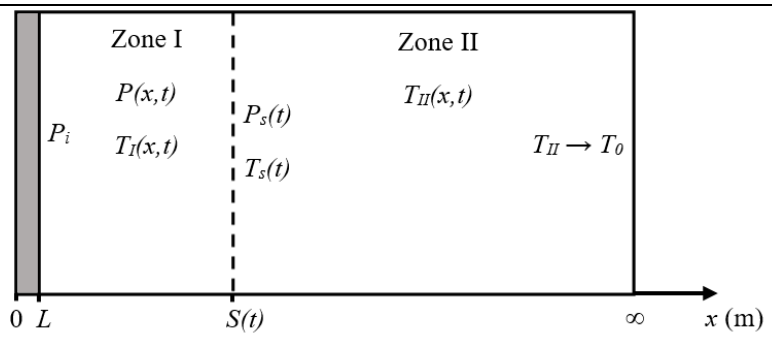

Figure 2. Schematic of hydrate dissociation in the semi-infinite flat reservoir. The dissociation interface is identified by the dashed line, and the grey region shows well thickness.

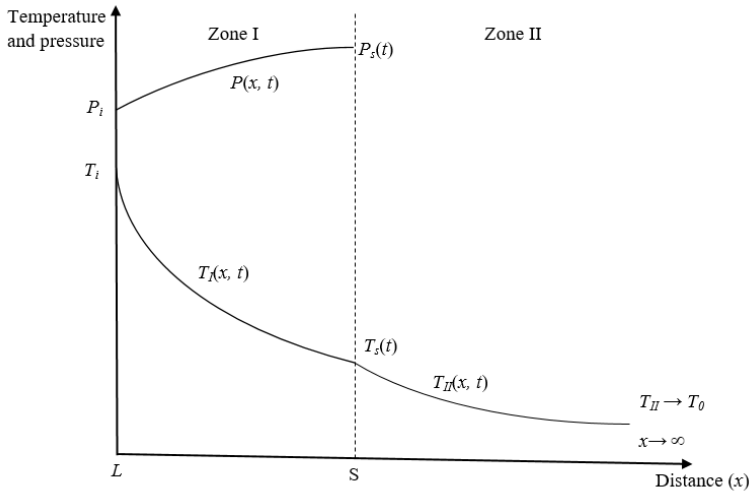

Figure 3. Schematic of pressure and temperature distribution in the reservoir upon hydrate dissociation.

According to the mass conservation law and the sudden change in density at the dissociation front due to gas production, the produced gas will be streaming towards the heat source. The assumptions considered in this part, which were in accordance with the previous analytical works (Selim and Sloan 1990; Tsimpanogiannis and Lichtner 2007), are as follows: i) hydrates filled the entire pores of the media; ii) temperature and pressure at the dissociation interface are at the thermodynamic equilibrium; iii) the produced water from the dissociation remains motionless in the pores; iv) thermophysical properties of the phases are constant; v) ideal behavior of gas is applied in the equation of state of gas; vi) the produced gas is in thermal equilibrium with the local sediments (with the same temperature); vii) viscous dissipation and inertia effects are neglected. It should be noted that the thermal properties of the system are assumed to remain constant during dissociation.

Another point that should be mentioned is that the volume of generated water from MH dissociation is negligible compared to that of generated gas (Kamath and Godbole 1987; Majorowicz and Osadetz 2001; Max and Dillon 1998) implying that the convection heat transfer by water has insignificant impact on MH dissociation. Furthermore, previous investigations on MH dissociation showed weak influence of water flow on gas production. For example, Zhao et al. (Zhao et al. 2015) by developing and validating 2D axisymmetric numerical model, showed that the influence of convection heat transfer of the generated water and gas on hydrate dissociation using thermal stimulation method is weak. In another numerical work (Zhao et al. 2014), they reported that the effect of convective heat transfer of water on dissociation upon depressurization is weaker compared to that of the produced gas. Sparrow et al. (Sparrow et al. 1977) numerically studied the convection and conduction heat transfers involved in melting of a solid by a vertical tubed-heater. Their analysis showed that for conduction only, the heat transfer rate decreased consistently. However, convection heat transfer by water movement caused a decrease in the heat transfer rate in early stages until attaining a minimum, then raised to a maximum, and finally decreased consistently. This behavior is due to weak convection heat transfer at early stages, then as the melt region grows, convection heat transfer becomes stronger and increased the overall heat transfer rate, however as the melt region thickness grows sufficiently, a boundary layer mechanism

induces no direct conduction heat transfer through the melt region, and only convection heat transfer by circulating fluid caused consistent drop in the heat transfer rate. They also revealed that the thickness of the melt region varies along the vertical tube, with maximum thickness at the top due to the convection heat transfer by water movement. Hence, due to the weak effect of water movement on heat transfer and eventually the dissociation process, assuming motionless water produced from dissociation causes negligible error in the final outcome. However, the convection heat transfer by gas is taken into account. Furthermore, in analytical approaches, if effect of a term dominates, the other terms may be ignored to reduce the complexity of the solution and the computation costs (Claisse 2014; Rapp 2016). It should be mentioned that previous analytical studies on MH dissociation did not consider convection heat transfer by dissociated water (Azizi et al. 2016; Kamath and Godbole 1987; Li et al. 2015; Li et al. 2016b; Selim and Sloan 1990; Tsimpanogiannis and Lichtner 2007).

The fundamental set of equations and the solution procedure for the flat case by considering a wellbore heat source are presented by the following expression:

The continuity equation of gas in Zone I is:

$$\phi\left(\frac{\partial \rho_g}{\partial t}\right)+\left(\frac{\partial \rho_g v_g}{\partial x}\right)=0,\ L<x<S,t>0 \tag{1}$$

where, ϕ is porosity, ρ_g is gas density (kg/m^3), and v_g is gas velocity (m/s). The gas velocity in Zone I is calculated by the multiphase Darcy's law, which is as follows:

$$v_g=-\left(\frac{k}{\mu}\right)\left(\frac{\partial P}{\partial x}\right),\ L<x<S,t>0 \tag{2}$$

where k is relative permeability of gas (md), μ is gas viscosity (mPa.s), and P is gas pressure (Pa). Equations 3 and 4 show the energy balance in Zones I and II, respectively:

$$\rho_I C_{pI}\frac{\partial T_I}{\partial t}+\frac{\partial \rho_g C_{pg} v_g T_I}{\partial x}=k_1\frac{\partial^2 T_I}{\partial x^2},\ L<x<S,t>0 \tag{3}$$

$$\frac{\partial T_{II}}{\partial t}=\alpha_{II}\frac{\partial^2 T_{II}}{\partial x^2},\ S<x<\infty,t>0 \tag{4}$$

where ρ_I is density (kg/m^3) of zone I, ρ_g is gas density (kg/m^3), C_{pI} is specific heat capacity (J/(kg.K)) of Zone I, C_{pg} is specific heat capacity of gas (J/(kg.K)), T_I is the temperature (K) in Zone I, T_{II} is the temperature (K) in Zone II, α_{II} is thermal diffusivity (m^2/s) of Zone II, and k_I is the thermal conductivity (W/(m.K)) of Zone I. In equation 3, the gas temperature in each location in Zone I is assumed to be equal to the local sediment temperature. This assumption has been proved by Weinbaum and Wheeler (Weinbaum and Wheeler Jr 1949) and also employed in another work by Selim and Sloan (Selim and Sloan 1990).

The gas behavior is assumed to obey the ideal gas law. So, the gas density in Zone I can be evaluated by the following equation:

$$\rho_g = \frac{mP}{RT_I},\ L < x < S, t > 0 \tag{5}$$

where m is gas molecular mass (kg/mol), and R is the universal gas constant (J/(mol.K)). The above set of equations represents the fundamental concept of the process. In the following, the associated initial and boundary conditions are stated. Temperature and pressure at the inner wall of the well (x = 0) are kept constant and respectively equal to T_i and P_i. It is assumed that there is no pressure drop in the well wall so the pressure at the outer surface of the well (x=L) is P_i as well.

The assumed wellbore schematic in the production region is shown in Figure 3, in which the thickness of each of the casings is 0.7 cm, and the thickness for the cement and gravel respectively is 2.5 cm and 1.5 cm. Hence, the heat transfer equation in the wellbore could be stated by equation 6:

$$-k_I A_w \frac{\partial T_I}{\partial x} = \frac{(T_i - T_I)}{R_w},\ x = L, t > 0 \tag{6}$$

$$R_w = \frac{1}{A_w}\left(\frac{L_s}{k_s} + \frac{L_c}{k_c} + \frac{L_g}{k_g}\right) \tag{7}$$

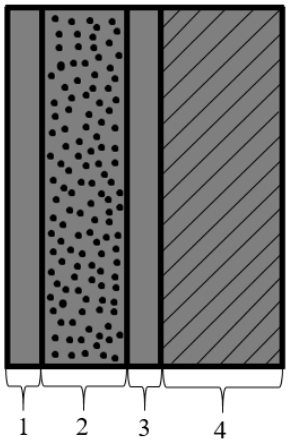

Figure 4. Schematic of the proposed wellbore structure. Different parts are as follows: 1) casing, 2) gravel pack, 3) casing, and 4) cement

where A_w is the wellbore area (m^2), R_w is thermal resistivity of the wellbore (W/K), k_x and L_x are respectively the thermal conductivity (J/(s.m.K)) and thickness (m) with *s*, *c*, and *g* subscripts respectively stands for steel (casing), cement, and gravel. It should be noted that this proposed structure for wellbore is a general geometry and model, and there are many of the wellbore structures and the associated geometries in the literature that are different from this model.

The pressure at the dissociation interface is calculated from the Antoine equation, which is a thermodynamic relationship with the interface temperature:

$$P_s = \mathrm{e}^{(A_a - B_a/T_s)},\ x = S, t > 0 \tag{8}$$

where P_s is the pressure (Pa) and temperature (K) at the moving interface, and A_a and B_a are constants.

The Antoine equation represents the relation between temperature and pressure of pure vapor (Araujo-Lopez et al. 2018; Khosravi Ghasemi et al. 2019; Thomson 1946). We employed this equation to calculate the pressure distribution in the dissociated zone (Zone I) of the reservoir. Actually, this zone consists of matrix sediments of the porous media and the produced gas and water from dissociation. However, as mentioned in the assumptions of the

modelling, the produced water from dissociation is assumed to remain motionless in the pores. Furthermore, the volume of generated water from MH dissociation is negligible compared to that of generated gas (Kamath and Godbole 1987; Majorowicz and Osadetz 2001; Max and Dillon 1998). Hence, due to the weak effect of water movement on heat transfer and eventually the dissociation (mentioned earlier in assumption section) along with small amount of produced water during the process, assuming motionless water produced from dissociation along with assuming pure-gas flow in the dissociated zone for the application of Antoine equation causes negligible error in the final outcome. The convection heat transfer by gas induces temperature and pressure distribution through the dissociated zone.

The mass and energy balances at the dissociation interface are respectively represented in equations 9 and 10. Also, the heat of MH dissociation is calculated by equation 11 (Selim and Sloan 1990), and equations 12-14 represent the boundary conditions:

$$F_{gH}\rho_H\left(\frac{dS}{dt}\right)+\rho_g v_g=0,\ x=S,t>0 \tag{9}$$

$$k_{II}\frac{\partial T_{II}}{\partial x}-k_I\frac{\partial T_I}{\partial x}=\phi\rho_H Q_{Hd}\frac{dS}{dt},\ x=S,t>0 \tag{10}$$

$$Q_{hyd}=c+dT_s \tag{11}$$

$$T_I=T_{II}=T_s(t),\ x=S,t>0 \tag{12}$$

$$T_{II}=T_0,\ x\to\infty,t>0 \tag{13}$$

$$T_{II}=T_0,0<x<\infty,t=0,\ S=L \tag{14}$$

where ρ_H is the hydrate density (kg/m^3), k_{II} is the thermal conductivity (W/(m.K)) of Zone II, Q_{Hd} is heat of MH dissociation (J/kg), and *c* and *d* are constants. F_{gH} in equation 8 is a constant, representing the ratio of mass of the methane gas trapped inside the MH to the mass of hydrate. In this work, the value of 0.1265 kg CH_4/kg hydrate is chosen for F_{gH}, which has been used in a previous study by Selim et al.(Selim and Sloan 1990).

The following equations 15-17 are obtained respectively from equations 1, 3, and 8 by employing equations 2 and 5 in order to eliminate the gas velocity and density.

$$\phi \frac{\partial}{\partial t}\left(\frac{P}{T_I}\right)-\frac{k}{\mu}\frac{\partial}{\partial x}\left(\frac{P}{T_I}\frac{\partial P}{\partial x}\right)=0 \tag{15}$$

$$\rho_I C_{pI}\frac{\partial T_I}{\partial t}+\frac{kmC_{pg}}{\mu R}\frac{\partial}{\partial x}\left(P\frac{\partial P}{\partial x}\right)=k_1\frac{\partial^2 T_I}{\partial x^2},\ L<x<S, t>0 \tag{16}$$

$$F_{gH}\phi\sigma_H\left(\frac{dS}{dt}\right)-\frac{kmP}{\mu R T_I}\frac{\partial P}{\partial x}=0,\ x=S, t>0 \tag{17}$$

To solve the above set of equations, the similarity solution introduced by Neumann (Ã–zisik et al. 1993; Carslaw and Jaeger 1959) is employed. In this solution, the movement of the dissociation interface is assumed to be proportional with the square root of time ($t^{1/2}$). This assumption satisfies the initial and boundary conditions, and the following dimensionless transformation, shown in equation 17, is employed to simplify and solve the abovementioned equations.

$$\lambda=\frac{x}{\sqrt{4\alpha_{II}t}} \tag{18}$$

So, on the moving dissociation front, equation 18 becomes:

$$\beta=\frac{S}{\sqrt{4\alpha_{II}t}},\ x=S, t>0 \tag{19}$$

Also, on the outer surface of the well:

$$\lambda_{os}=\frac{L}{\sqrt{4\alpha_{II}t}},\ x=L, t>0 \tag{20}$$

The transformation of the above equations using equation 17 is developed and presented in the Appendix A.

By considering the procedure suggested by Özışık et al.(Ã–zisik et al. 1993), Carslaw et al.(Carslaw and Jaeger 1959), and Selim et al.(Selim and Sloan 1990), error function is employed to choose the following solutions for the temperature distributions:

$$\begin{cases} T_I = A\,erf\,(a\lambda+b)-A\,erf\,(b)+B \\ T_{II}=T_0+C\,erfc(\lambda) \end{cases} \tag{21}$$

A, *B*, *a*, and *b* constants are introduced in Appendix A. The parameter “b” in equations S13 and S20 defines the convection heat transfer for gas by taking into account the specific heat

capacity of gas. The gas produced from dissociation will absorb some of the transferred heat from the wellbore to the dissociation interface. This definition is in line with previous analytical studies (Azizi et al. 2016; Selim and Sloan 1990; Tsimpanogiannis and Lichtner 2007). Furthermore, Selim and Sloan (Selim and Sloan 1990) in their analytical investigation on MH dissociation upon thermal stimulation reported that the convection heat transfer by gas flow decreased the dissociation rate about 6% meaning that it does not have a significant impact on the process.

The pressure distribution (Pa) in Zone I can be calculated from equation S7 as follows:

$$P(\lambda)=\left(P_0^2+\frac{4F_{gH}\phi\rho_H\alpha_{II}\mu R\beta}{km}\int_{\lambda_{os}}^{\lambda}T_I d\lambda\right)^{1/2} \tag{22}$$

That by replacing and integrating T_I from equation 21, becomes:

$$P=\left(P_0^2+J(\beta)K(\beta)(\lambda-\lambda_{os})+AJ(\beta)(L_1(\lambda)-L_1(\lambda_{os}))\right)^{1/2} \tag{23}$$

where $J(\beta)$, $K(\beta)$, and $L_1(\lambda)$ are defined in Appendix A.

Heat flux at the boundary (J/(s.m^2)) as a function of time is calculated from the following formula:

$$u_f=-k_I\frac{\partial T_I}{\partial x},\ x=L \tag{24}$$

The transformed version of equation 24 considering equation 18 is provided in Appendix A.

Cumulative heat input into the reservoir from the heat source (J/m^2) is calculated by integrating equation 23 with regard to time as follows:

$$Q_{ft}=-k_I\int_0^t\frac{\partial T_I}{\partial x}dt\ ,\ x=L \tag{25}$$

In order to calculate the total volume at standard temperature and pressure (STP) of dry gas, equation 26 is employed, where V_{fp} is the total volume of produced gas per surface area of the moving interface up to time t (m^3/m^2), n_{ft} is the total moles of gas produced per surface area of the moving interface up to time t (mole/m^2), and T_{STP} and P_{STP} are temperature and pressure of gas at STP conditions, respectively.

$$V_{fp} = \frac{n_{ft} R T_{STP}}{P_{STP}} \tag{26}$$

More details of total volume calculation are provided in Appendix A.

For the efficiency evaluation of gas production during the dissociation process using thermal stimulation method, the energy efficiency ratio is introduced as follows (Song et al. 2015):

$$\eta_f = \frac{V_{fp} Q_g}{Q_{ft}} \tag{27}$$

where η_f is the energy efficiency ratio in this case, and Q_g is the heating value of the gas at STP conditions (J/m^3). Actually, η_f represents the amount of energy that would be produced from combustion of the produced gas to the amount of input energy to the system from the heat source. It becomes apparent that an energy efficiency higher than one is preferred. It should be mentioned that the surface area of the well that is in contact with the reservoir is equal to 1m^2.

The obtained solution for temperature and pressure distributions can satisfy the abovementioned basic equations and boundary conditions (equations 1-17) by direct substitution.

2.2 MH dissociation in Radial coordinates employing line and wellbore heat sources

Figure 5 shows a schematic of the hydrate dissociation in the proposed radial geometry. The dashed circle shows the moving dissociation boundary, and the grey region denotes the wellbore thickness consisting of a cement, gravel, and two layers of casing. There are many different wellbore structures and geometries assumed in the literature for different purposes, such as rock fracturing (Wang et al. 2019a), SAGD steam injection (Xiong et al. 2015), and oil recovery (Sun et al. 2018). The proposed wellbore structure in this part is taken as a general model as understood to the best of our knowledge from the previous studies about gravel-packing technique (Florez Anaya and Osorio 2014), sand-control purpose (Pucknell and Mason 1992), wellbore's thermal resistance (Wang et al. 2016a), and gas extraction from the MH reservoirs by depressurization (Florez Anaya and Osorio 2014; Xu et al. 2014).

The geometry of the other case using a line heat-source is exactly the same as Figure 5, but it uses a line heat-source without thickness in the center of the reservoir instead of a wellbore with a specific thickness. The following steps are assumed as the basics of MH dissociation: i) before the dissociation begins, the reservoir has a porosity of ϕ and is filled with MH in equilibrium conditions of temperature T_0; ii) at time t=0, the heat source warms up by increasing its temperature (the inner surface of the heat source for the wellbore-heat-source case) to a new temperature T_i, which is higher than the hydrate equilibrium temperature, and is kept constant afterward; iii) MH dissociation begins with a sharp moving boundary surface showing the rate of hydrate dissociation and separating the water and gas produced in the dissociated zone (Zone I) from the undissociated zone (Zone II).

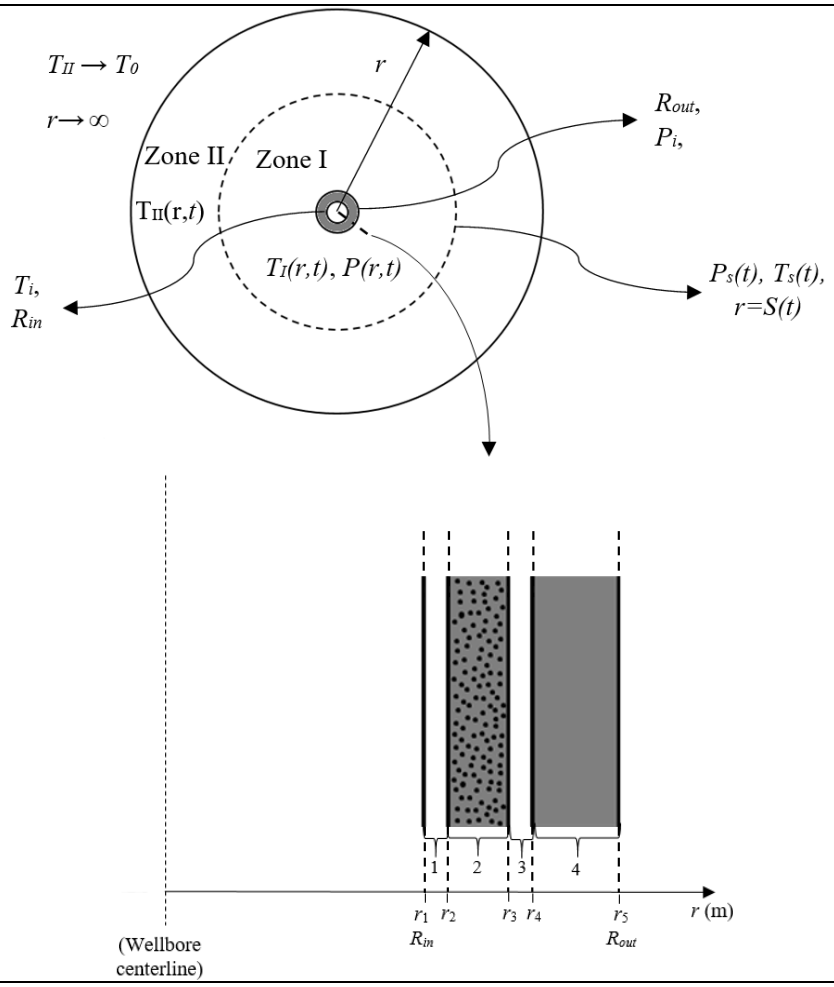

Figure 5. Schematic of hydrate dissociation model in infinite radial model. The dissociation interface is identified by the dashed circle. The grey region shows the wellbore thickness. Different parts of the wellbore structure are: 1) casing I, 2) gravel pack, 3) casing II, and 4) cement

During dissociation, Zone I's temperature is higher than that of Zone II inducing heat transfer from the Zone I to Zone II. Principally, the heat input from the heat source is consumed in two different ways: i) temperature increment of the matrix sediments and the produced water and gas in Zone I; and ii) hydrate dissociation and the temperature increment of the matrix materials in Zone II. Over time, Zone I becomes larger and absorbs higher amount of input heat (the first way mentioned above) reducing the dissociation rate and the moving interface speed.

Figure 6 shows the temperature and pressure distributions in the system after dissociation begins. The temperature and pressure distributions in Zone I (T_I and P) are respectively $T_s < T_I < T_i$ and $P_i < P < P_s$, and the temperature distribution in Zone II (T_{II}) is $T_0 < T_{II} < T_s$ by assuming a constant hydrate pressure equal to the equilibrium pressure in this zone. It should be noted that T_I at the outer surface of the well changes over time, but it is always lower than T_i.

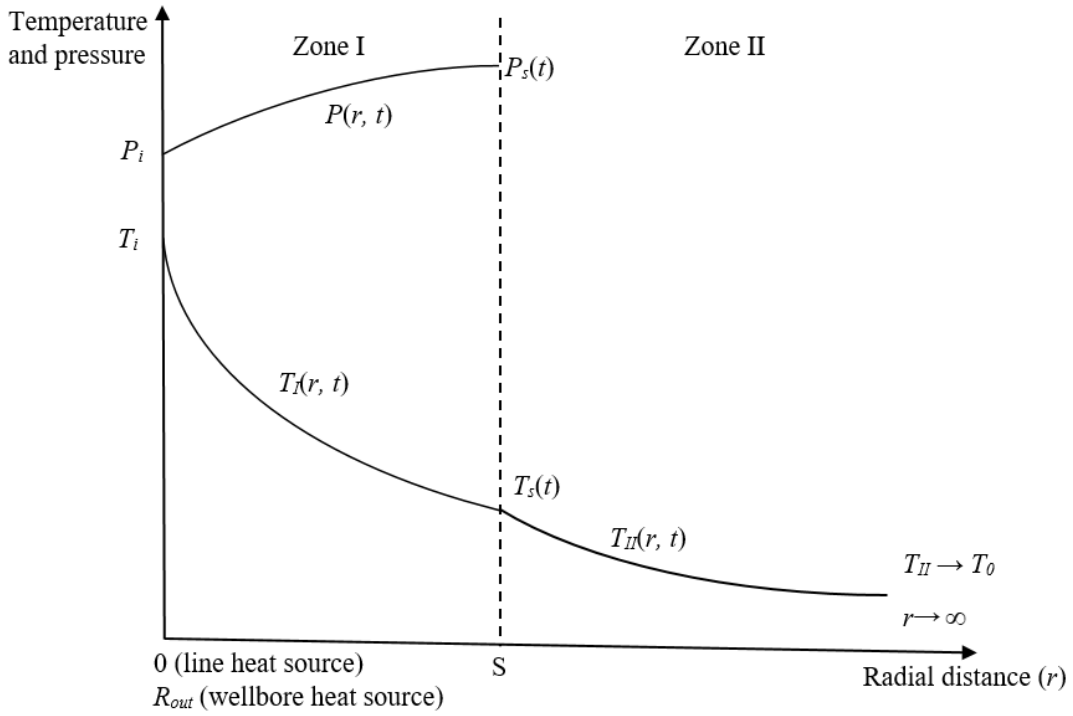

Figure 6. Schematic of pressure and temperature distribution in the reservoir upon hydrate dissociation.

The produced gas will be streaming towards the heat source according to Darcy's Law and induces a sudden change in density at the dissociation front. Other assumptions made in the models of this part are the same as those of the previous part, which are consistent with the previous analytical works (Selim and Sloan 1990; Tsimpanogiannis and Lichtner 2007; Weinbaum and Wheeler Jr 1949).

Basic equations, which are the same for both types of heat sources (line heat-source and wellbore heat-source), are presented in the following formulas.

The continuity equation of gas in Zone I is:

$$\phi\left(\frac{\partial \rho_g}{\partial t}\right)+\left(\frac{\partial \rho_g v_g}{\partial r}\right)=0,\ t>0 \tag{28}$$

where r is the radial distance (m). The gas velocity in Zone I is calculated by using Darcy's Law:

$$v_g=-\left(\frac{k}{\mu}\right)\left(\frac{\partial p}{\partial r}\right),\ t>0 \tag{29}$$

Equations 30 and 31 show the energy balance in Zones I and II, respectively:

$$\rho_I C_{pI}\frac{\partial T_I}{\partial t}+\frac{\partial \rho_g C_{pg} v_g T_I}{\partial r}=k_1\frac{\partial}{\partial r}r\frac{\partial T_I}{\partial r},\ t>0, \text{ in Zone I} \tag{30}$$

$$\frac{\partial T_{II}}{\partial t}=\frac{\alpha_{II}}{r}\frac{\partial}{\partial r}r\frac{\partial T_{II}}{\partial r},\ t>0, \text{ in Zone II} \tag{31}$$

Equation 5 employed to calculate the gas density in Zone I ($R_{out}<r<S, t>0$).

The above equations represent the fundamental concept of the process. The heat sources' temperature and pressure are constant and equal to T_i and P_i, respectively. Equations 32 and 33 also state these conditions:

$$T_I=T_i,\begin{cases}\text{Line heat}-\text{source: } r=0, t>0\\ \text{Wellbore heat}-\text{source: } r=R_{in}, t>0\end{cases} \tag{32}$$

$$P=P_i,\begin{cases}\text{Line heat}-\text{source: } r=0, t>0\\ \text{Wellbore heat}-\text{source: } r=R_{out}, t>0\end{cases} \tag{33}$$

Equation 34 states the heat transfer equation through the wellbore thickness:

$$-k_I A_w\frac{\partial T_I}{\partial r}=\frac{(T_i-T_I)}{R_w}, r=R_{out}, t>0 \tag{34}$$

$$R_w=\frac{\ln(r_2/r_1)}{2\pi k_s}+\frac{\ln(r_3/r_2)}{2\pi k_g}+\frac{\ln(r_4/r_3)}{2\pi k_s}+\frac{\ln(r_5/r_4)}{2\pi k_c} \tag{35}$$

Where r is radius (m), the *s*, *c*, and *g* subscripts respectively stand for steel (casing), cement, and gravel, and the subscripts 1-5 are schematically shown on Figure 5.

The interface pressure ($r = S, t > 0$) is calculated by the Antoine Equation (equation 8). Equations 36 and 37 respectively show the mass and energy balances at the dissociation interface. The formula for MH dissociation heat is the same as that of the previous section (equation 11) and the associated boundary conditions are represented through the equations 38-40 (Selim and Sloan 1990),:

$$F_{gH}\rho_H\left(\frac{dS}{dt}\right)+\rho_g v_g = 0,\ r = S, t > 0 \tag{36}$$

$$k_{II}\frac{\partial T_{II}}{\partial r}-k_I\frac{\partial T_I}{\partial r}=\phi\rho_H Q_{Hd}\frac{dS}{dt},\ r = S, t > 0 \tag{37}$$

$$T_I = T_{II} = T_s(t),\ r = S, t > 0 \tag{38}$$

$$T_{II} = T_0,\ r \to \infty, t > 0 \tag{39}$$

$$T_{II} = T_0, 0 < r < \infty, t = 0 \tag{40}$$

The following equations 41-43 are obtained respectively from equations 28, 30, and 36 by employing equations 29 and 5 to eliminate the gas velocity and density.

$$\phi\frac{\partial}{\partial t}\left(\frac{P}{T_I}\right)-\frac{k}{\mu}\frac{\partial}{\partial r}\left(\frac{P}{T_I}\frac{\partial P}{\partial r}\right)=0 \tag{41}$$

$$\rho_I C_{pI}\frac{\partial T_I}{\partial t}+\frac{kmC_{pg}}{\mu R}\frac{\partial}{\partial r}\left(P\frac{\partial P}{\partial r}\right)=\frac{k_1}{r}\frac{\partial}{\partial r}r\frac{\partial T_I}{\partial r},\ t > 0, \text{ in Zone I} \tag{42}$$

$$F_{gH}\phi\sigma_H\left(\frac{dS}{dt}\right)-\frac{kmP}{\mu R T_I}\frac{\partial P}{\partial r}=0,\ r = S, t > 0 \tag{43}$$

The similarity solution, which was employed in the previous part, using a dimensionless parameter (equation 44 in this part) is used for transformation, simplification, and solution of the equations mentioned above. This method satisfies the initial and boundary conditions and assumes the movement of the dissociation interface to be inversely proportional with the square root of time ($t^{1/2}$) as follows:

$$\lambda = \frac{r}{\sqrt{4\alpha_{II}t}} \tag{44}$$

On the moving dissociation interface, equation 44 becomes:

$$\beta = \frac{S}{\sqrt{4\alpha_{II} t}},\ r = S, t > 0 \tag{45}$$

And, on the outer surface of the wellbore:

$$\lambda_{os} = \frac{R_{out}}{\sqrt{4\alpha_{II} t}},\ r = R_{out}, t > 0 \tag{46}$$

The abovementioned equations are transformed by employing equations 44-46 and presented in Appendix B.

By considering the procedure recommended by previous works (Ã–zisik et al. 1993; Carslaw and Jaeger 1959), the following solutions for the temperature distributions in the two heat source cases are assumed implementing the exponential integral (Ei) function:

Line heat-source: $$\begin{cases} T_I(\lambda) = T_i - A_1 Ei(-(a\lambda + b)^2) + A_1 Ei(-b^2) \\ T_{II}(\lambda) = T_0 + B_1 Ei(-\lambda^2) \end{cases} \tag{47}$$

Wellbore heat-source: $$\begin{cases} T_I(\lambda) = -A_2 Ei(-(a\lambda + b)^2) + A_2 Ei(-b^2) + C \\ T_{II}(\lambda) = T_0 + B_2 Ei(-\lambda^2) \end{cases} \tag{48}$$

A_1, B_1, C, A_2, and B_2 constants are defined in Appendix B.

The pressure distribution in Zone I for both heat sources can be calculated from the equation S35 as follows:

$$P(\lambda) = \left(P_0^2 + \frac{4F_{gH}\phi\rho_H \alpha_{II} \mu R \beta}{km} \int T_I d\lambda \right)^{1/2} \tag{49}$$

Then, equations 50 and 51 show the pressure distributions for both heat sources by replacing and integrating T_I from equations 47 and 48:

Line heat-source: $$P = \left(P_0^2 + L_2(\beta) M(\beta) \lambda + A_1 L_2(\beta)(N(0) - N(\lambda)) \right)^{1/2} \tag{50}$$

Wellbore heat-source: $$P = \left(P_0^2 + L_2(\beta)(K_1(\beta)\lambda - A_2 N(\lambda) - (K_1(\beta)\lambda_{os} - A_2 N(\lambda_{os}))) \right)^{1/2} \tag{51}$$

where $L_2(\beta)$, $M(\beta)$, $N(\lambda)$, and $K_1(\beta)$ are defined in Appendix B. The obtained solutions for temperature and pressure distributions satisfy the basic equations and boundary conditions (equations 28-43) by direct substitution.

The following formula calculates the heat flux from the wellbore (J/(s.m^2)) as a function of time:

$$u_r = -k_I \frac{\partial T_I}{\partial r},\ r = R_{out} \tag{52}$$

Equation 52 can be transformed to an equal equation according to equation 44 (provided in Appendix B).

Integrating equation 52 gives the total heat input into the reservoir from the heat source (J/m^2) up to time *t* as follows:

$$Q_{rt} = -k_I \int_0^t \frac{\partial T_I}{\partial r} dt,\ r = R_{out} \tag{53}$$

The total volume of produced gas at standard temperature and pressure (STP) of dry gas can be calculated as follows:

$$V_{rp} = \frac{n_{rt} R T_{STP}}{P_{STP}} \tag{54}$$

where V_{rp} and n_{rt} respectively are the total volume (m^3/m^2) and total moles (mole/m^2) of produced gas per average moving-interface surface area up to time *t* at T_{STP} and P_{STP} as temperature and pressure of dry gas at STP conditions, respectively. Further details are provided in Appendix B.

Following formula evaluates the dissociation energy efficiency (Song et al. 2015):

$$\eta_r = \frac{V_{rp} Q_g}{Q_{rt}} \tag{55}$$

where η_r is the energy efficiency ratio.

2.3 MH dissociation in Radial coordinates considering a coaxial borehole heat exchanger

A schematic of the dissociation process inside the reservoir is presented in Figure 7a. Zone II is composed of undissociated hydrate at a temperature of T_0 at infinity ($r \to \infty$), which increases to converge to the dissociation temperature ($T_s(t)$) close to the moving dissociation boundary ($r=S(t)$), denoted by the dashed circle. Zone I expresses the dissociated region, with

its different temperatures and pressures at various locations (r) and times (t). The grey ring in the middle of Figure 7a shows the supporting structure of the wellbore. A top view of the wellbore is shown in Figure 7b. The wellbore considered in this study has coaxial configuration with pipe-in-pipe geometry (Braud et al. 1983; Mei and Fischer 1983). Hot water is supplied to the wellbore either through the inner tube or the annulus between the inner and outer tubes; it is then extracted from the other path (Figure 7b). Heat transfer to the reservoir occurs through the borehole's external wall. The borehole's external layers, shown in Figure 1c, appear in cross section area of the borehole wall in Figure 7b. These layers (from inner to outer) are the 1) inner tube wall; 2) inside casing; 3) gravel; 4) outside casing; and 5) cement, and the associated radii are shown in Figure 7c. The following basic steps are considered as the MH dissociation process in this modelling: i) before dissociation begins, MH is assumed to be in equilibrium condition at a temperature T_0 in the reservoir pores; ii) at time $t = 0$, hot water is injected into wellbore with a constant flow rate and temperature, inducing heat transfer to the reservoir; iii) when the temperature at the external wall of the borehole reaches the dissociation temperature of MH, dissociation begins, followed by a sharp moving boundary surface separating the dissociated zone (the water and gas produced in Zone I) from the undissociated zone (the undissociated MH in Zone II).

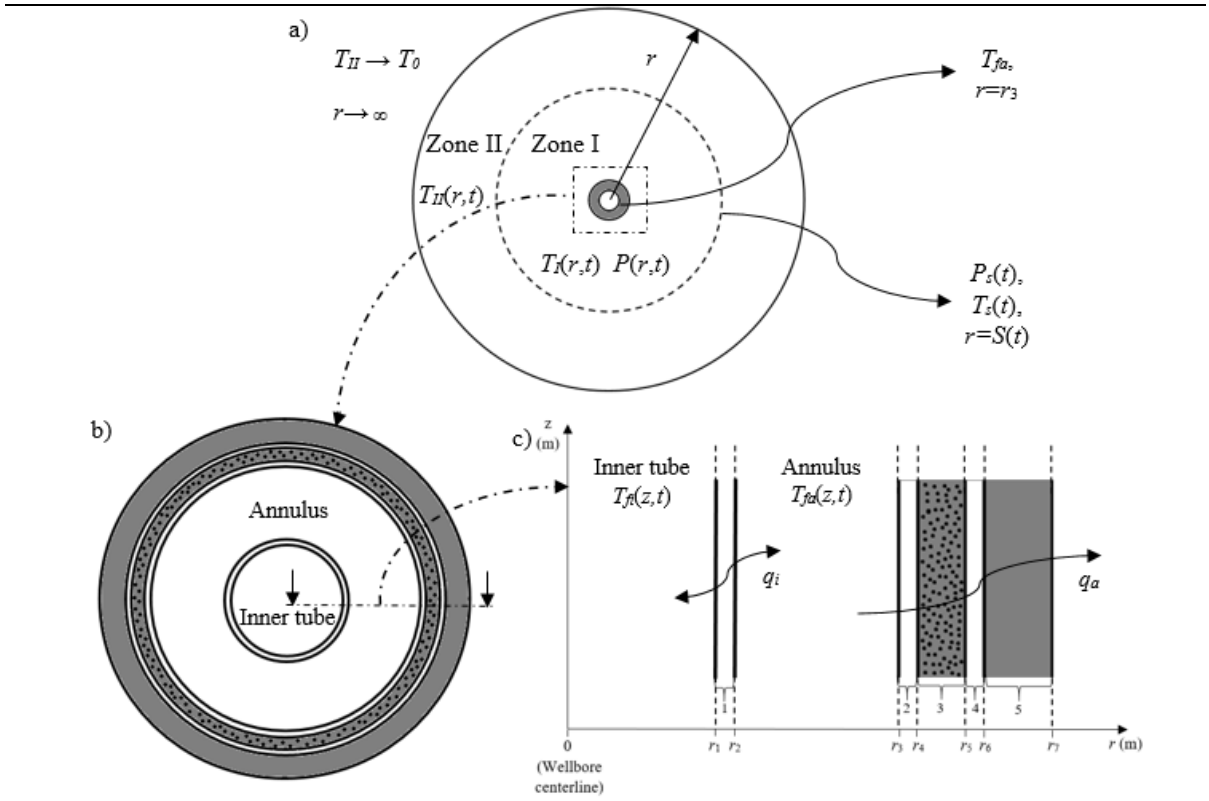

Figure 7. a) Schematic of the infinite radial model of hydrate dissociation considered in this study. The dissociation interface is identified by the dashed circle, and the grey region shows the well thickness. b) Magnified image of the borehole top view. c) Borehole structure with borehole center line denoted by a dashed line, and the various layers: 1) Inner tube wall; 2) Inside casing; 3) Gravel; 4) Outside casing; and 5) Cement.

As was mentioned previously, two operation conditions are considered for the heat source: i) hot water injection into the inner tube and extraction from the annulus; and ii) hot water injection into the annulus and extraction from the inner tube. The flow rate and the temperature of the injected water are constant in models. However, the temperature distribution of the fluid along the inner tube (T_{fi}) and the annulus (T_{fa}) is not constant, and changes over time due to the heat transfer to the outside via conduction and the convection heat transfer of the fluid inside the wellbore.

The heat transfer rate inside the wellbore (e.g. between the annulus and inner tube) and to the reservoir are represented respectively by q_i and q_a (Figure 7c). The former (q_i) consists of three heat transfer components: i) convection heat transfer in the inner tube between the water flow and the inner surface of the tube; ii) conduction heat transfer through the inner tube thickness to the annulus; and iii) convection heat transfer between the outer surface of the inner tube and the water flow in the annulus. The latter (q_a) consists of: i) convection heat transfer between the water flow and the outer surface of the annulus; and ii) the conduction heat transfer through the external wall of the wellbore (cement, casing, and gravel layers). For each of the heat transfer components of q_i and q_a, a thermal resistance is defined in the following based on the heat transfer calculation of the wellbores presented by Hellstrom (Hellstrom 1992).

Convective heat transfer resistance (m.K/W) between the inner tube surface ($r=r_1$) and the water flow in the tube is defined as follows:

$$R_{cii} = \frac{1}{\pi k_f Nu_{ii}} \tag{56}$$

where R_{cii} is the convective heat transfer resistance (m.K/W), k_f is the fluid thermal conductivity (W/m.K), and Nu_{ii} is the Nusselt's number of the fluid flow in the inner tube. Different formulas have been suggested for Nusselt's number in previous literature with varying degrees of accuracy (Dittus and Boelter 1930; Gnielinski 1975; Hausen 1959; Kraussold 1934; Notter and Sleicher 1972; Petukhov 1970; Rohsenow et al. 1985; Sieder and Tate 1936). Among them, Gnielinski correlation (Gnielinski 1975) is reported to be suitable and accurate for coaxial heat exchangers considering fluid flow in the annulus (Gnielinski 2009; Ntuli et al. 2010; Rohsenow et al. 1985; Wärmeatlas 1988). Nusselt's number of fluid flow in the inner tube is defined as follows based on the Gnielinski formula (Gnielinski 1975):

$$Nu_{ii} = \frac{(f/2)(\mathrm{Re}_i - 1000)\,\mathrm{Pr}}{1 + 12.7(f/2)^{1/2}(\mathrm{Pr}^{2/3} - 1)} \tag{57}$$

where Re_i is the Reynolds number in the inner tube, Pr is the Prandtl number, and f is the friction factor for smooth pipes. Re_i, Pr, and f are calculated respectively as follows:

$$\mathrm{Re}_i = \frac{v_f D}{\nu_f} = \frac{2 r_1 v_f \rho_f}{\mu_f} = \frac{2 \rho_f V_f}{\pi \mu_f r_1} \tag{58}$$

$$\mathrm{Pr} = \frac{\mu_f C_f}{\rho_f k_f} \tag{59}$$

$$f = (1.58 \ln(\mathrm{Re}_i) - 3.28)^{-2} \tag{60}$$

where D is the pipe diameter (m), v_f is the water flow velocity (m/s), ν_f is the kinematic viscosity (m^2/s), ρ_f is the water density (kg/m^3), V_f is the water flow rate (m^3/s), r_1 is the radial distance (m) as shown in Figure 7c, C_f is the fluid volumetric heat capacity ($J/(m^3.K)$), and μ_f is the water dynamic viscosity (Pa.s).

The conduction thermal resistance (m.K/W) of the tube is calculated as follows:

$$R_p = \frac{\ln(r_2 / r_1)}{2\pi k_p} \tag{61}$$

where r_2 and r_1 are inner tube radii as shown in Figure 7c, and k_p is the inner tube's thermal conductivity (W/(m.k)).

The convection thermal resistance (mK/W) of the heat transfer from the outer surface of the inner tube ($r=r_2$) to the fluid flow in the annulus can be represented as follows (Hellstrom 1992):

$$R_{coi} = \frac{1}{\pi k_f Nu_{oi}} \left(\frac{1}{r^*} - 1 \right) \tag{62}$$

where Nu_{oi} is the Nusselt's number of the fluid flow close to the outer surface of the inner tube, and r^* is the ratio between the inner and outer radii of the annulus (r_2 / r_3). Petuhkov and Roizen (Petukhov and Roizen 1967) derived an expression for the Nusselt's number in the annulus close to the inner tube based on experimental data:

$$Nu_{oi} = \zeta Nu_{pipe} 0.86 (r^*)^{-0.16} \tag{63}$$

where ζ is a constant, equal to 1 in this case, and Nu_{pipe} is the Nusselt's number of the water flow in the annulus close to the inner pipe, calculated based on equation 57, using the Prandtl number and friction factor formulas from equations 59 and 60, and a Reynolds number as follows:

$$\mathrm{Re}_a = \frac{v_f d_h}{\nu_f} = \frac{2(r_3 - r_2) v_f \rho_f}{\mu_f} = \frac{2(r_3 - r_2) \rho_f V_f}{\pi (r_3^2 - r_2^2) \mu_f} \tag{64}$$

where r_3 and r_2 are the radii (m) of the annulus, shown in Figure 7c, and d_h is the hydraulic diameter (m) of the annulus, which can be calculated as follows:

$$d_h = 2(r_3 - r_2) \tag{65}$$

The convection thermal resistance (m.K/W) of the region between water flow and the outer surface of the annulus (r=r_3) can be calculated based on the following formula (Hellstrom 1992):

$$R_{cia} = \frac{1}{\pi k_f Nu_{oa}} \left(1 - r^* \right) \tag{66}$$

where Nu_{oa} is the Nusselt's number of the water flow close to the outer surface of the annulus, which is defined as follows based on the work performed by Petuhkov and Roizen (Petukhov and Roizen 1967):

$$Nu_{oa} = Nu_{pipe}(1-0.14(r^*)^{0.6}) \tag{67}$$

And finally, in order to calculate the conduction thermal resistance of the external wall of the wellbore, the wall can be considered as a homogenous layer by summing the thermal resistances of the cement, casing, and gravel layers together as stated in equation 68:

$$R_w = \frac{\ln(r_4/r_3)}{2\pi k_p} + \frac{\ln(r_5/r_4)}{2\pi k_g} + \frac{\ln(r_6/r_5)}{2\pi k_s} + \frac{\ln(r_7/r_6)}{2\pi k_c} \tag{68}$$

where k_x stands for thermal conductivity (W/(m.K)) with the *s*, *c*, *p*, and *g* subscripts respectively referring to the steel (casing), cement, inner pipe, and gravel. Figure 7 also shows r_3-r_7.

Therefore, the total thermal resistances ((m.K)/W) associated with q_i and q_a are respectively as follows:

$$R_1 = R_{cii} + R_p + R_{coi} \tag{69}$$

$$R_2 = R_{cia} + R_w \tag{70}$$

At steady-state condition, the convection heat transfer in the water flow should be equal to the transverse heat transfer between the inner tube and annulus (q_i) and between the annulus and wellbore (q_a). This expression is presented in equations 71 and 72:

$$\pm C_f V_f \frac{\partial T_{fi}(z,t)}{\partial z} = \underbrace{\frac{T_{fi}(z,t) - T_{fa}(z,t)}{R_1}}_{q_i(z,t)} \tag{71}$$

$$\pm C_f V_f \frac{\partial T_{fa}(z,t)}{\partial z} = \underbrace{\frac{T_{fa}(z,t)-T_I(r_7,t)}{R_2} + \frac{T_{fa}(z,t)-T_{fi}(z,t)}{R_1}}_{q_a(z,t)} \quad (72)$$

where T_{fi} is the water flow temperature (K) in the inner tube, and T_{fa} is the water flow temperature in the annulus (K), and *z* represents the axial distance along the wellbore, which is in the range of 0 (at the base of the wellbore) to h (top boarder of the hydrate zone). Some notations in equations 71 and 72 should be taken into account: i) the $\pm$ sign refers to the direction of the water flow, with + standing for the water flow in the direction of the z-axis; and ii) in q_a calculation, an average value of the temperature along the outer surface of the external wall of the wellbore ($T_I(r_7)$) is considered instead of a varying temperature with regards to the z-axis. The temperature distribution resulted from the two operation models of the heat source (T_{fi} and T_{fa}) can be obtained by solving equations 71 and 72 and considering two boundary conditions: i) the inlet temperature (T_i) is constant; and ii) no heat flux occurs at the base of the wellbore. More details are provided in Appendix C. Then, the heat transfer rate to the reservoir can be obtained, after which, the subsequent hydrate dissociation will be calculated as described next. The heat transfer from the heat source to the reservoir is consumed in two ways: i) by increasing the temperature of the sediments and the water-gas produced in the dissociated zone; and ii) in hydrate dissociation at the moving boundary and increasing the temperature of the matrix materials in Zone II close to the moving boundary. The input heat should transfer through the dissociated region, during which, a large part of the input heat will be consumed as in i) reducing the rate of hydrate dissociation and the speed of the moving interface as the process continues.

The proposed trends of temperature and pressure distribution in the reservoir during dissociation are shown in Figure 2. The temperature and pressure ranges for a specific time in Zone I are respectively $T_s < T_I < T_I(r_7)$ and $P_i < P < P_s$, and in Zone II, the temperature range will be $T_0 < T_{II} < T_s$ with a constant pressure equal to the equilibrium pressure of MH. The temperature at the outer surface of the wellbore ($r=r_7$) changes with time due to the heat

transfer from the wellbore and temperature changes of the inside fluid, but it is always lower than the temperature on the other side of the wellbore (T_{fa}). The temperature and pressure at the moving dissociation boundary are not also constant.

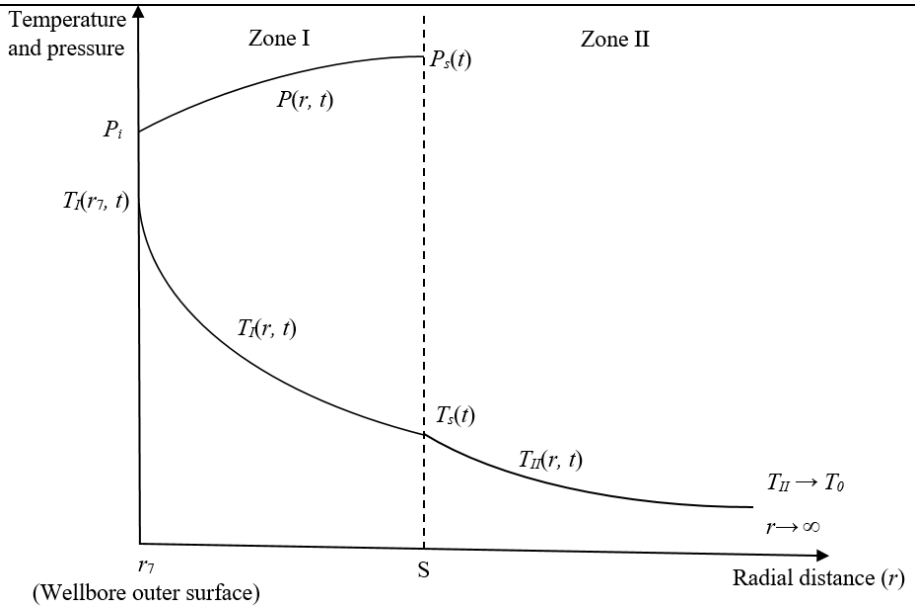

Figure 8. Schematic of pressure and temperature distribution in the reservoir during MH dissociation.

The produced gas will stream towards the heat source according to Darcy's Law, inducing a sudden change in density at the dissociation front due to the gas production. There are a lot of similarities between the solution method stated in this part for MH dissociation and those of the previous part. Assumptions made in the dissociation models of the current part are the same as those of the previous part.

The continuity equation of gas in Zone I is stated in equation 28. The gas velocity (v_g) in Zone I is calculated using equation 29. Equations 30 and 31 show the energy balance in Zones I and II, respectively. The gas density in Zone I, based on the ideal gas law, can be calculated by equation 5:

The initial and boundary conditions are: i) temperature and pressure at the inner wall of the wellbore (r_3) are known at each time step due to the calculations mentioned earlier for temperature distribution inside the wellbore; and ii) no pressure drop is assumed in the wellbore, and the pressure at the outer surface of the well (r_7) is P_i.

The heat transfer equation in the well, for the case considering the well's heat source, is stated by Equation 6:

$$-k_I A_w \frac{\partial T_I}{\partial r} = \frac{(T_{fa} - T_I)}{R_2}, r = r_7, t > 0 \quad (73)$$

where A_w is the wellbore surface area (m^2), R_w is thermal resistivity of the wellbore (W/K), k_I is the thermal conductivity of Zone I (W/(m.K)), r is the radius (m). It should be noted that the wellbore structure proposed in the present part is the same as that of the previous part.

Temperature and pressure at the moving dissociation interface are calculated by the Antoine Equation (equation 8).

The mass and energy balances at the dissociation interface as well as the heat of MH dissociation are respectively represented in equations 36, 37, and 11 (Selim and Sloan 1990) with the associated initial and boundary conditions represented through equations 38-40.

The similarity solution is also employed to solve the abovementioned equations in this part, using the same dimensionless parameter relating the movement of the dissociation interface to the square root of time ($t^{1/2}$), as represented by a non-dimensional parameter shown in equation 44. This parameter on the moving dissociation interface ($r = S$) and outer surface of the wellbore ($r = r_7$) is represented through the equations 45 and 46, respectively.Therefore, by using equations 44-46, the previous equations are simplified and transformed, as presented in Appendix C in detail.

An exponential integral (Ei) function is employed to find the solution to the temperature distribution in the reservoir during dissociation as described in equations 73 and 74. This solution has also been recommended in previous works (Ã–zisik et al. 1993; Carslaw and Jaeger 1959).

$$T_I = -A_3 Ei\left(-(a\lambda + b)^2\right) + A_3 Ei\left(-b^2\right) + B_3 \quad (73)$$

$$T_{II} = T_0 + C_1 Ei\left(-\lambda^2\right) \quad (74)$$

The A_3, B_3, and C_1 constants are defined in Appendix C.

Then, the pressure distribution in Zone I can be calculated from equation S35 as follows:

$$P(\lambda)=\left(P_0^2+\frac{4F_{gH}\phi\rho_H\alpha_{II}\mu R\beta}{km}\int T_I d\lambda\right)^{1/2} \tag{75}$$

By replacing T_I according to equation 37, the pressure distributions in zone I will be calculated as shown in equation 40:

$$P=\left(P_0^2+L_3(\beta)(K_2(\beta)\lambda-A_3N(\lambda)-(K_2(\beta)\lambda_{os}-A_3N(\lambda_{os})))\right)^{1/2} \tag{76}$$

where $L_3(\beta)$, $N(\lambda)$, and $K_2(\beta)$ are defined in Appendix C. It should be noted that the obtained expressions for temperature and pressure distributions can satisfy the basic equations and boundary conditions, mentioned earlier, by direct substitution.

Heat flux (J/sm^2) from the wellbore to the reservoir as a function of time can be obtained from the following formula:

$$u_r=-k_I\frac{\partial T_I}{\partial r},\ r=r_7 \tag{77}$$

Equation 77 can be transformed into an equal equation according to equation 30 (Appendix C).

By integrating Equation 77, the total heat input into the reservoir from the wellbore (J/m^2) up to time *t* can be calculated as in the following equation:

$$Q_{rt}=-k_I\int_0^t\frac{\partial T_I}{\partial r}dt\ ,\ r=r_7 \tag{78}$$

The total volume of gas produced up to time *t* can be calculated as follows at the standard temperature and pressure (STP) of dry gas:

$$V_{rp}=\frac{n_{rt}RT_{STP}}{P_{STP}} \tag{79}$$

where V_{rp} and n_{rt} are respectively the total volume (m^3/m^2) and total moles (mole/m^2) of produced gas per surface area of the moving interface up to time *t* with T_{STP} and P_{STP} respectively as the temperature and pressure of dry gas at STP conditions. Further details of the calculation of the total volume of produced gas are provided in Appendix C.

The energy efficiency ratio of the process is defined as follows (Song et al. 2015):

$$\eta_r = \frac{V_{rp} Q_g}{Q_{rt} (2\pi r_7 h)} \tag{80}$$

where η_f is the energy efficiency ratio, and Q_g is the heating value of the gas at STP conditions (J/m^3).

MATLAB programming software is used for all calculations in this work.

Chapter 3
Results and discussion

Some parts of the thesis are published in two journals: i) the Journal of Petroleum Science and Engineering (Roostaie and Leonenko 2019b) with DOI: 10.1016/j.petrol.2019.106505 and License: CC-BY-NC-ND; and ii) the Energy Journal (Roostaie and Leonenko 2019a) with DOI: 10.1016/j.energy.2019.116815 and License: CC-BY-NC-ND. This thesis has resulted in another paper (Roostaie and Leonenko 2020) (arXiv preprint: arXiv:2001.04900) and submitted to the Energy Conversion and Management Journal.

3.1 One-dimensional model with a flat heat source

Equation 18 indicates that the location and movement of the dissociation interface are dependent on β. It should be noted that β represents both the dimensionless interface position and dimensionless interface velocity ($v_s / (4\alpha_{II} t)^{1/2}$). Thus, the higher the value of β, the faster the movement of the dissociation interface. As shown in the equation S23, the value of β is dependent on P_s and T_s values, which are calculated using the pressure and temperature at the heat source wall (outer boundary) according to the equations in the previous section. The temperature at the outer boundary of the heat source is time dependent, inducing P_s and T_s at the dissociation front to change over time. Figure 9 shows the value of β considering specific physical and boundary conditions presented in Table 2, which are obtained and set from the previous studies (Cheng et al. 2011; Dalla Santa et al. 2017; Remund 1999; Selim and Sloan 1990). β increases from a slightly lower value at the beginning but converges to a value as the temperature at the wall surface converges to temperature T_i of the inside of the well, which is kept constant.

Table 2. Parameters used in the modeling.	
Total wellbore thickness, L, m	0.054
Cement thickness, L_c, m	0.025
Gravel thickness, L_g, m	0.015
Casing thickness, L_s, m	0.014
Contact area of wellbore with reservoir in production region, m^2	1
Thermal conductivity of cement, k_c, W/(m.K)	0.933
Thermal conductivity of gravel, k_g, W/(m.K)	0.4
Thermal conductivity of casing (steel), k_s, W/(m.K)	43.3
Porosity, ϕ	0.3
Permeability, k, μm^2	1
Thermal diffusivity of Zone I, α_I, $\mu m^2/s$	2.89×10^6
Thermal conductivity of Zone I, k_I, W/(m.K)	5.57
Thermal diffusivity of Zone II, α_{II}, $\mu m^2/s$	6.97×10^5
Thermal conductivity of Zone II, k_{II}, W/(m.K)	2.73
Hydrate density, ρ_H, kg/m^3	913
Heat of dissociation of hydrate, Q_{Hd}, J/kg	$446.12\times10^3 - 132.638T_s$
Gas heat capacity, C_{pg}, J/(kg.K)	8766
Gas viscosity, μ, Pa.s	10^{-4}
Heating value of the gas at STP conidtions, Q_g, MJ/m^3	37.6
Molecular mass of methane, m, g/mol	16.04
Mass ratio of the methane gas trapped inside the hydrate to the mass of hydrate, F_{gH}	0.1265
Universal gas constant, R, J/(mol.K)	8.314

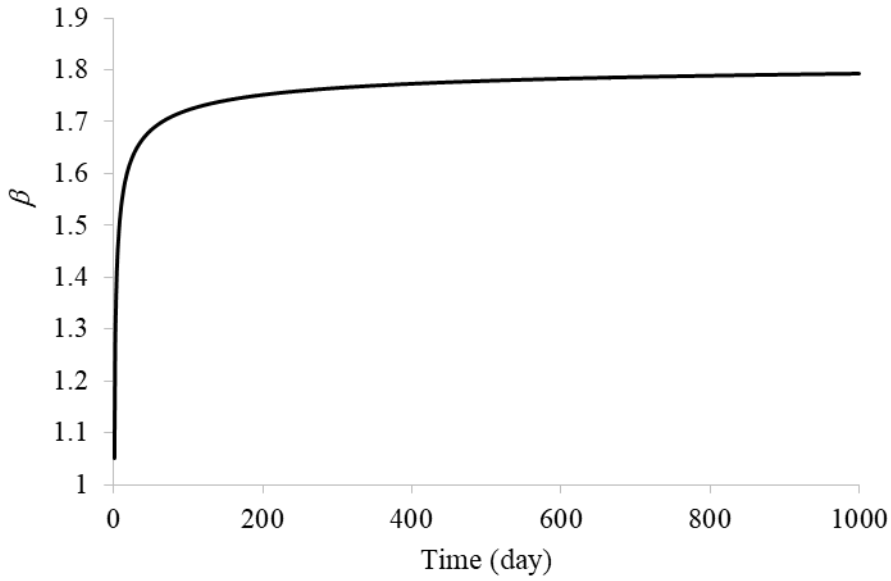

Figure 9. Dimensionless position of interface during 1000 days dissociation process at T_i=563.5 K, P_i=7.6 MPa, and T_0=275K.

The effect of boundary conditions on the interface movement is presented in Figure 10, which shows the value of β with regards to different well pressure and temperature after 100 days of dissociation. The results shown in Figure 10 have the same trend as the results reported in the previous work by Selim et al. (Selim and Sloan 1990), but with a slightly lower values of β (about 0.1 difference). This difference is due to the conduction heat transfer in the wellbore thickness, which causes the amount of transferred heat to the dissociation surface becomes lower compared to the previous work (Selim and Sloan 1990), in which a flat heat source with constant temperature without wellbore thickness is considered. In all cases, decreasing the heat source pressure while increasing its temperature induces higher values of β. Figure 11 represents the relation between the interface velocity and MH temperature, T0. The higher the hydrate temperature, the higher the interface movement. These results are consistent with data obtained in a Numerical work by Liang et al. (Liang et al. 2010), who also found that decreasing the pressure and increasing the surrounding temperature would increase the rate of hydrate dissociation upon

depressurization. They also validated their results against experiments performed by Masuda (MASUDA 1999).

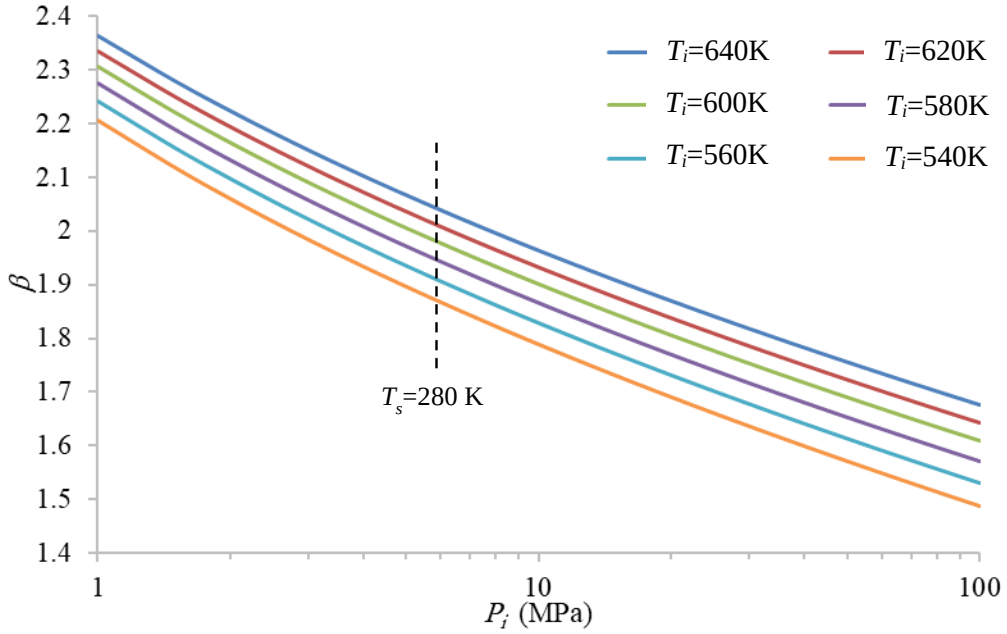

Figure 10. Dimensionless position of interface at T_0=280 K and various T_i and P_i values.

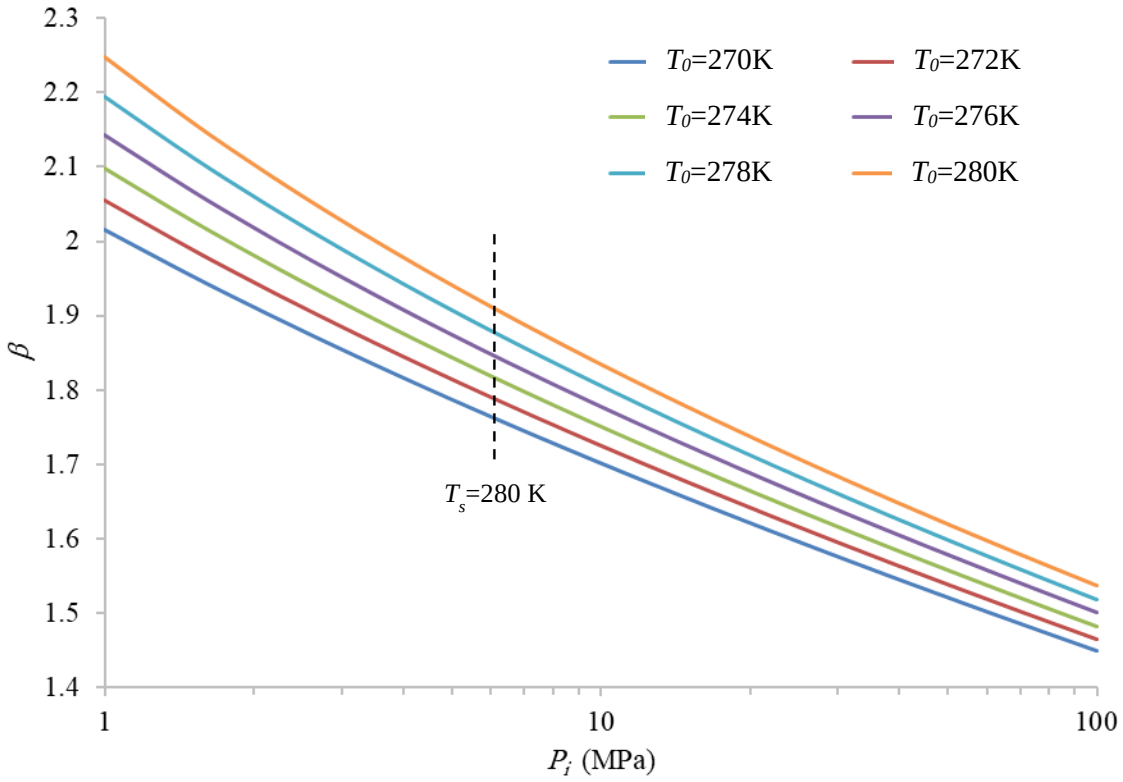

Figure 11. Dimensionless position of interface at T_i=563.5 K and various T_0 and P_i values.

Furthermore, in Figures 10 and 11, the associated temperature and pressure of the locus for which the dissociation temperature is equal to the temperature of MH (280 K) is shown. The dissociation temperature is mainly dependent on heat source pressure, while the effect of the temperature of the heat source and MH temperatures on T_s is almost negligible; higher P_i increases T_s, while lower P_i decreases T_s. This is also in agreement with the previous work by Selim et al. (Selim and Sloan 1990), as they showed the direct dependency of T_s on P_i and mentioned that for lower pressures of 6 MPa, T_s may reduce to the freezing temperature of water which causes the interruption of the dissociation process due to ice generation. It should be mentioned that when T_s is equal to T_0, all the transmitted heat to the interface is consumed for the dissociation and no heat is transferred to or from the hydrate zone, and the temperature of the hydrate zone remains constant. On the other hand, as T_s falls below T_0,

some part of the required heat for dissociation is absorbed from the hydrate zone, resulting in the temperature reduction of the hydrate zone.

Temperature and pressure distributions are calculated and presented in Figures 12 and 13 for the following two boundary conditions (BCs): BC 1) $T_i = 450\,\mathrm{K}$, $P_i = 10$ MPa, and $T_0 = 280\,\mathrm{K}$, and BC 2) $T_i = 563.5\,\mathrm{K}$, $P_i = 7.6$ MPa, and $T_0 = 275\,\mathrm{K}$ considering three different time frames. The temperature distribution in Zones I and II are separated by a horizontal dashed line that shows the interface temperature. However, due to the small temperature increment at the well surface in longer time frames (as shown in the Figure 12), the interface temperature changes slightly. The temperature change at the well surface also causes the interface pressure to change in longer time frames. It should be noted that as the dissociation progresses and the temperature at the well surface converges to that inside the well, the temperature and pressure at the interface respectively tend to decrease and increase gradually and converge to the associated values reported Selim and Sloan's work (Selim and Sloan 1990), in which the associated values for the interface temperature and pressure for the two proposed boundary conditions were reported to be: BC 1) T_s = 285 K, P_s = 290 Pa; BC 2) T_s = 282.5 K, P_s = 560 Pa. Tsimpanogiannis and Lichtner (Tsimpanogiannis and Lichtner 2007) in their semi-analytical model showed that increasing the temperature of well would increase the pressure at the interface, which is also shown in our results of boundary conditions of BC 1 and BC 2.

The results of temperature distribution also illustrate that the distance between the dissociation surface and the heat source is higher in the previous study without considering the wellbore thickness (Selim and Sloan 1990) compared to the present model due to the negative effect of heat conduction in the well, but this difference decreases in longer time frames as the dissociated zone thickens and the effect of heat source thickness disappears gradually. The results presented in Figure 12 for temperature distribution are also in good agreement with those reported by Li et al. (Li et al. 2011b), who experimentally investigated MH dissociation upon thermal stimulation. They also reported that the decomposition

progressed by a moving boundary, which separates dissociate zone form the undissoicated zone.

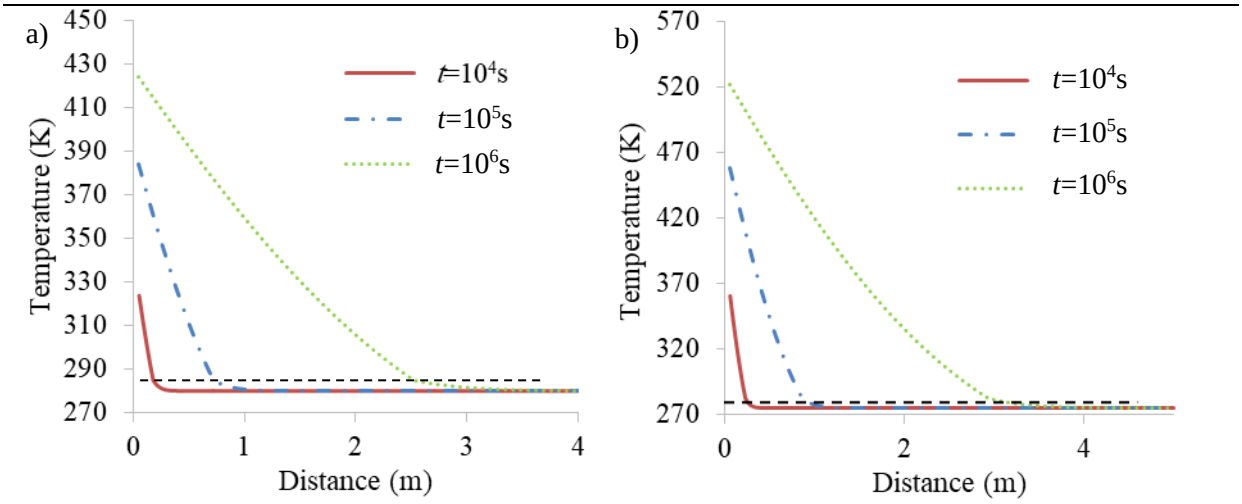

Figure 12. Temperature distribution for case 1 at different time frames for two initial and boundary conditions of a) BC 1 b) BC 2.

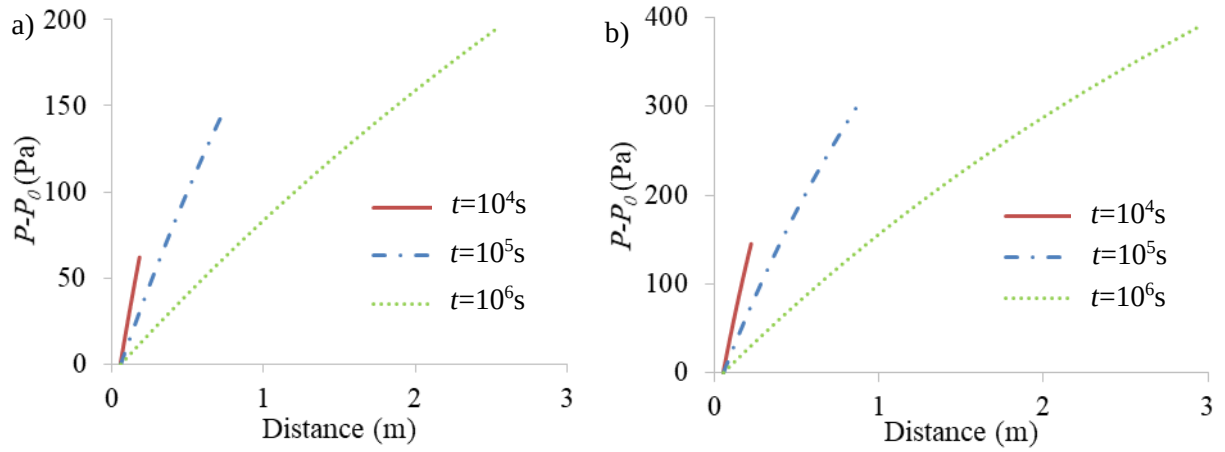

Figure 13. Pressure distribution for case 1 in the dissociated zone at different time frames for two initial and boundary conditions of a) BC 1 b) BC 2.

The volume of produced gas in STP conditions, amount of input heat, and energy efficiency upon hydrate dissociation considering the two initial and boundary conditions during 100

days of gas dissociation are shown in Figure 14. The volume of produced gas and the amount of input heat are higher considering BC 2 compared to BC 1. However, the energy efficiency is higher considering BC 2 compared to BC 1 due to the higher difference between the amounts of input heat and relatively smaller difference between the associated produced gas as shown in Figure 14. The results of energy efficiency indicate that increasing the heat source temperature and decreasing its pressure would increase the rate of dissociation, but will not increase the total efficiency of the process. It is somewhat surprising that the energy efficiency increases to a peak point in the beginning then it decreases as dissociation progresses. This could be due to the constant surface area of the dissociation interface, which is equal to the surface area of the heat source, during the dissociation that restricts the amount of gas production during dissociation. On the other hand, the amount of input heat increases such that it cannot reach the dissociation front due to the sediment matrix of Zone I and dissociation products. Therefore, the speed of input heat increment exceeds the speed of the produced gas increment until the temperature at the heat source surface gradually converges to that inside the heat source, and the energy efficiency also converges to a constant value.

The same trend for energy efficiency (i.e., significant increase at the beginning then decreasing smoothly) was also reported by Li et al. (Li et al. 2014; Li et al. 2011a) and Wang et al. (Wang et al. 2013), who investigated the MH dissociation behavior upon thermal stimulation using cubic hydrate simulators. They claimed that the sudden increase of the energy efficiency at the beginning is due to the rapid hydrate dissociation close to the wellbore at the beginning of the process. In another experimental work performed by Wang et al. (Wang et al. 2014b) on the gas production form MH using thermal stimulation by hot water, the same trend for the energy efficiency and gas production was reported. It was claimed that the pre-depressurization before heat stimulation caused the sudden increase of the energy efficiency at the beginning, then it decreased and converged to lower value. They reported an energy efficiency of around 4 after 100 minutes of dissociation, which shows a good agreement with our results. In the work of Selim et al. (Selim and Sloan 1990) an energy efficiency between 6.4-11.2 was reported, which is close to the results presented in the current paper and of high value because of the similar conditions considered in the two

works. The energy efficiency reported in this work is consistent with that of Tang et al. (Tang et al. 2005), who experimentally investigated the gas production from MH reservoirs upon thermal stimulation. They reported an energy ratio, which was calculated in the same way as the energy efficiency in the present work, of about 5 upon conditions close to the BC 2. They also revealed that increasing the initial temperature and decreasing the initial pressure improved the energy ratio. Bayles et al. (Bayles et al. 1986) studied analytically MH dissociation upon cyclic steam injection. They reported the same trend for the energy efficiency for one year dissociation, which was converged between 4 to 9.6. Again, our results are in good agreement with theirs, and the slight difference could be due to the direct steam injection into the reservoir and the cyclic pattern of the process.

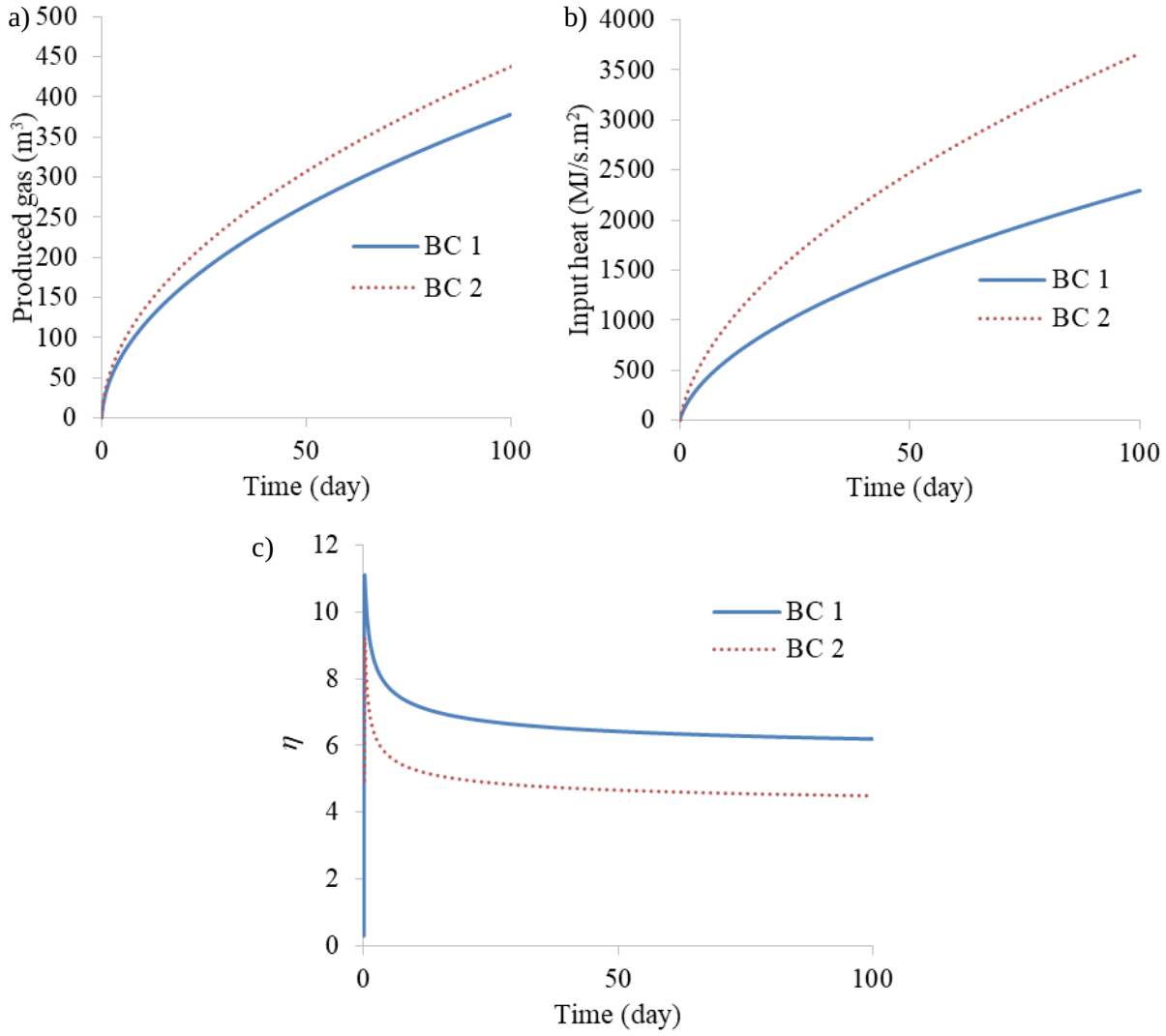

Figure 14. a) volume of produced gas, b) amount of input heat, and c) energy efficiency during hydrate dissociation for two BCs.

A parametric study is performed in order to investigate the effect of various parameters, stated in Table 3, on the dissociation process. The obtained results from the parametric study, shown in Figure 15, indicate the following points: a) the higher the thermal diffusivity and conductivity of Zone I, the higher the dissociation movement; b) the lower the thermal diffusivity and conductivity of Zone II, the higher the dissociation movement; and c) the permeability and gas viscosity almost have no effect on the dissociation process as the interface velocity does not change by various values of each.

The same results were reported by Selim and Slaon (Selim and Sloan 1990). Zhao et al. (Zhao et al. 2015) investigated the numerical model of gas production form MH using thermal stimulation and showed that increasing the thermal conductivity promoted the dissociation process, on the other hand, different relative water-gas permeabilities have almost no effect on the gas production. They also numerically showed that increasing sediments' thermal conductivity would increase the rate of gas generation at the beginning of hydrate dissociation upon depressurization (Zhao et al. 2014). It should be mentioned that both of their works were validated by the experimental work of Masuda (MASUDA 1999). Tsimpanogiannis and Lichtner (Tsimpanogiannis and Lichtner 2007) investigated a parametric study on the effect of different parameters on the MH dissociation upon thermal stimulation. They revealed that increasing the thermal conductivity of the porous media induced more MH dissociation.

Table 3. Range of parameters employed in the parametric study.

Porosity, ϕ	0.1 to 0.5
Permeability, k, μm^2	0.1 to 5
Thermal diffusivity of Zone I, α_I , $\mu m^2/s$	1×10^6 to 5×10^6
Thermal conductivity of Zone I, k_I , W/(m.K)	3 to 7
Thermal diffusivity of Zone II, α_{II} , $\mu m^2/s$	4×10^5 to 8×10^5
Thermal conductivity of Zone II, k_{II} , W/(m.K)	1 to 5
Gas viscosity, μ , Pa.s	10^{-4} to 10^{-6}

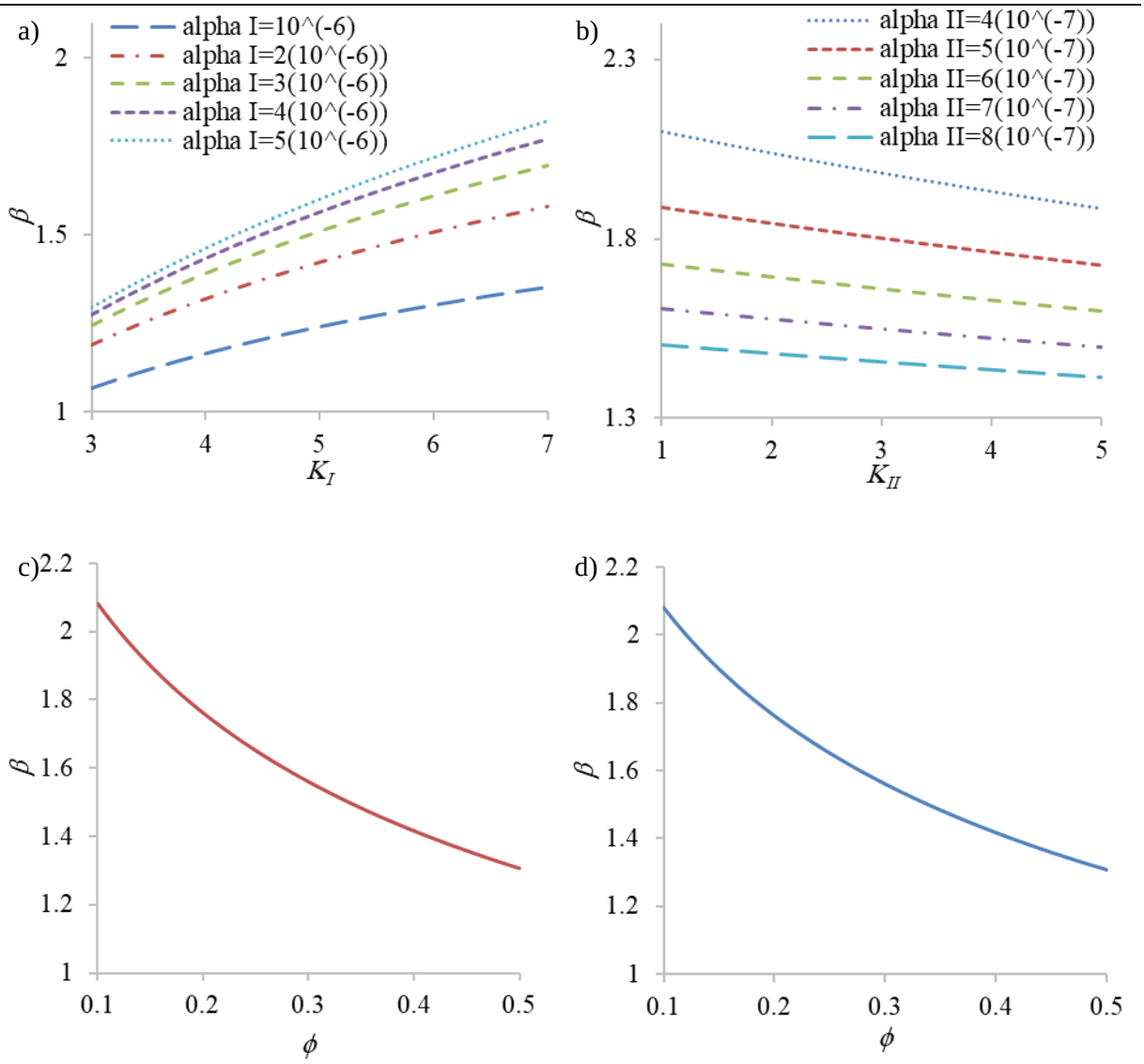

Figure 15. The effect of various values of the parameters stated in Table 2 on the interface movement after 100 days dissociation. a) thermal diffusivity and thermal conductivity of Zone I, b) thermal diffusivity and thermal conductivity of Zone II, c) various values of porosity with different permeabilities, and d) various values of porosity with different gas viscosities.

3.2 Radial model with line and wellbore heat sources

As equation 20 indicates, β represents the dissociation interface dimensionless position and velocity ($v_s / (4\alpha_{II} t)^{1/2}$). The value of β only depends on P_s and T_s (equation S28), which depend on the heat source pressure and temperature (outer surface of the heat source in the wellbore-heat-source case) according to their associated equations in the modeling section. The temperature at the wellbore outer surface is time-dependent, inducing variable P_s and T_s over time; however, the line heat-source temperature in the other case remains constant, inducing constant P_s and T_s. The proposed properties and parameters (Table 4) are based on the previous studies (Cheng et al. 2011; Dalla Santa et al. 2017; Remund 1999; Selim and Sloan 1990). Figure 16 shows that β increases at the beginning in the wellbore-heat-source case because the temperature at the wellbore outer surface increases over time, but tends to converge to the associated value of β in the line-heat-source case as the temperature at the wellbore outer surface converges to the temperature inside of the well (T_i).

Table 4. Parameters used in the modeling.	
Wellbore's inner surface radius, R_{in} (r_1), m	0.07
r_2, m	0.077
r_3, m	0.092
r_4, m	0.099
Wellbore's outer surface radius, R_{out} (r_5), m	0.124
Cement thermal conductivity , k_c, W/(m.K)	0.933
Gravel thermal conductivity, k_g, W/(m.K)	0.4
Casing (steel) thermal conductivity, k_s, W/(m.K)	43.3
Porosity, ϕ	0.3
Permeability, k, μm^2	1
Zone I thermal diffusivity, α_I , $\mu m^2/s$	2.89×10^6
Zone I thermal conductivity, k_I , W/(m.K)	5.57
Zone II thermal diffusivity, α_{II} , $\mu m^2/s$	6.97×10^5
Zone II Thermal conductivity, k_{II} , W/(m.K)	2.73
Hydrate density, ρ_H , kg/m^3	913
Hydrate dissociation heat , Q_{Hd} , J/kg	$446.12\times10^3 - 132.638T_s$
Gas heat capacity, C_{pg} , J/(kg.K)	8766
Gas viscosity, μ , Pa.s	10^{-4}
Gas heating value at STP conditions, Q_g , MJ/m^3	37.6
Methane molecular mass, m, g/mol	16.04
Methane gas mass ratio trapped inside the hydrate, F_{gH}	0.1265
Universal gas constant, R, J/(mol.K)	8.314

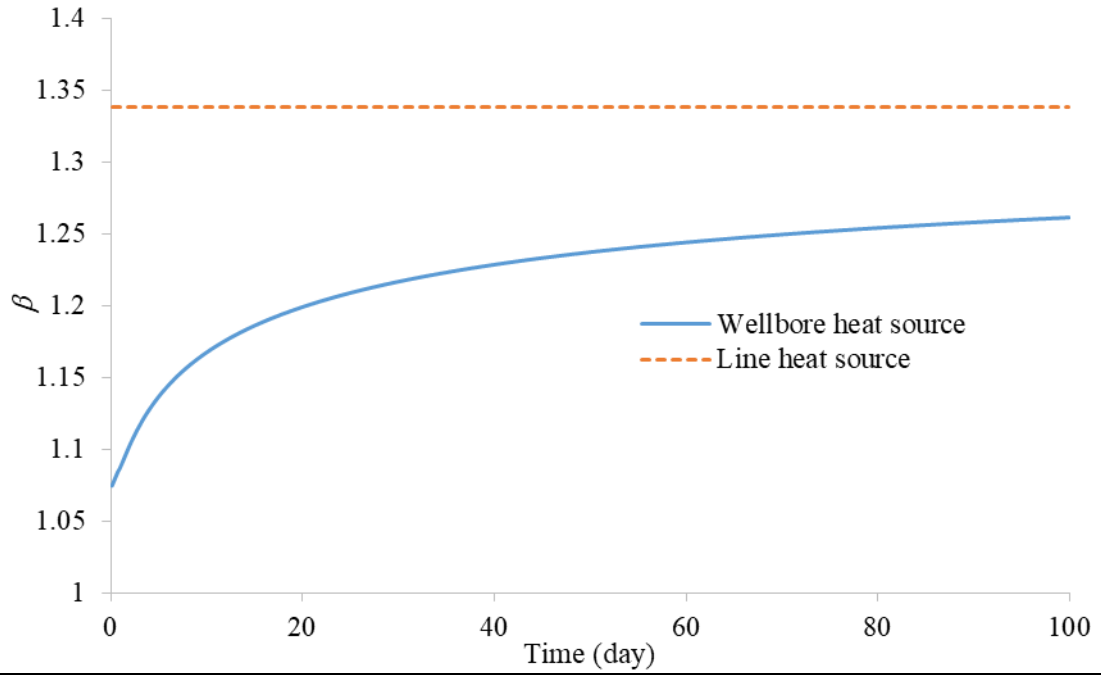

Figure 16. Dimensionless interface position assuming T_0=275 K $T_i = 563.5$ K, and $P_i = 7.6$ MPa.

Figure 17 represents the boundary conditions effect on the interface movement 100 days after the process begun using both heat sources. Increasing the pressure and decreasing the heat source temperature decrease β. The initial temperature of MH also has a direct impact on β. Previous study by Selim and Sloan have reported the same relation between β and P_i, T_i, and T_0 (Selim and Sloan 1990). Another numerical work on MH dissociation upon depressurization, which was validated against Masuda's results (MASUDA 1999), showed that decreasing wellbore pressure and increasing reservoir temperature increase the dissociation rate (Liang et al. 2010).

a)

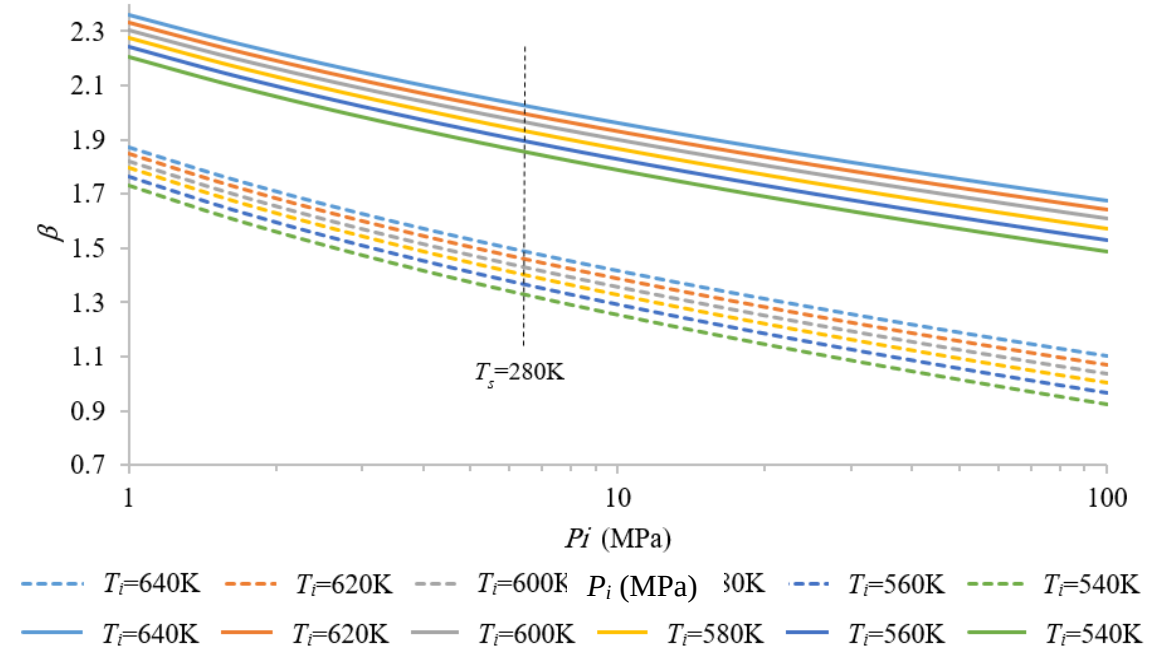

b)

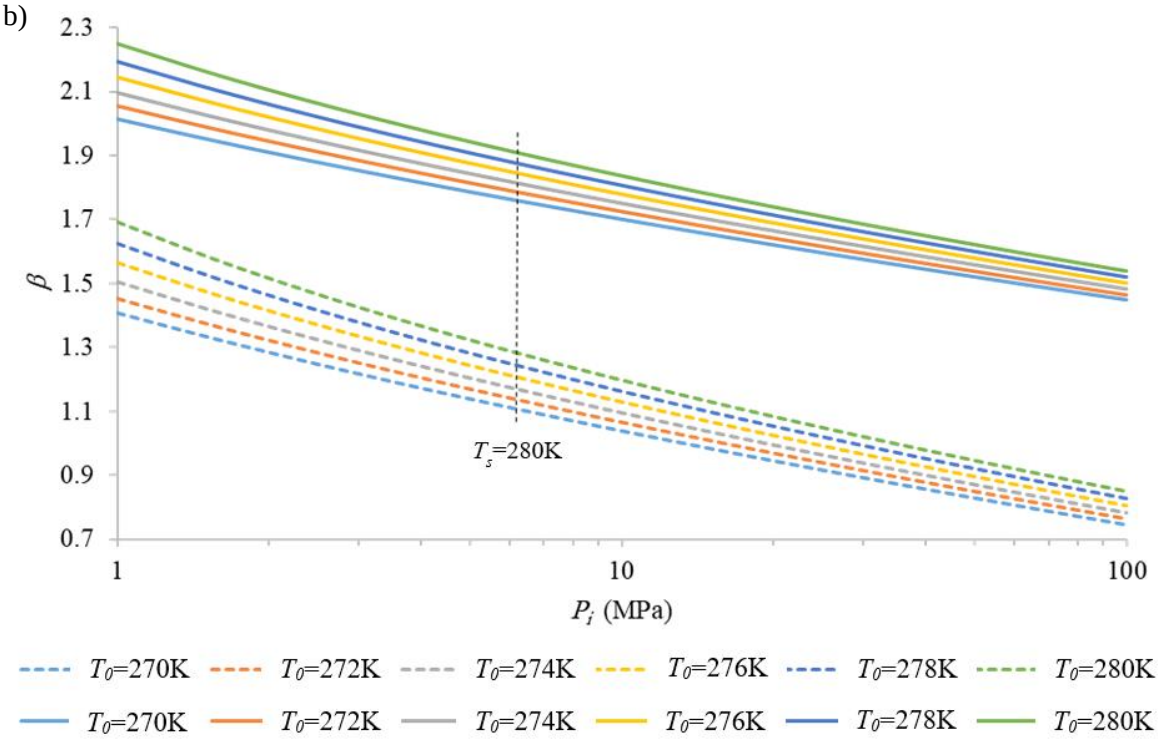

Figure 17. Dimensionless interface position assuming: a) T_0=280 K and various T_i and P_i values, and b) T_i=563.5 K and various T_0 and P_i values. Dashed lines and solid lines respectively represent the wellbore-heat-source and the line-heat-source cases.

The vertical dashed lines in Figure 17 show the associated temperature and pressure at the locus on which the dissociation temperature equals 280 K. On the loci left (lower P_i) and right (higher P_i) of this locus, the dissociation temperature decreases and increases, respectively. This temperature is mainly dependent on heat source pressure, and almost independent of the heat source and MH temperatures. Previous work (Selim and Sloan 1990) also reported that under lower heat source pressures of 6 MPa, T_s may reduce to the freezing temperature of water, and ice generation can induce the stoppage of the dissociation. For situations in which T_s is higher than the MH temperature, some part of heat input from the heat source will be consumed to increase the temperature of MH close to the dissociation front to T_s. If T_s approaches T_0 all heat from the heat source is consumed for dissociation. Conversely, if T_s falls below T_0, some part of the heat required for dissociation will be provided from the hydrate zone, reducing the temperature of this zone near the dissociation interface.

Temperature and pressure distributions for the two heat sources are calculated and presented in Figures S1 and S2 considering three different time frames and the following initial and boundary conditions (BCs): BC 1) $T_i = 450\,\text{K}$, $P_i = 10$ MPa, and $T_0 = 280\,\text{K}$, and BC 2) $T_i = 563.5\,\text{K}$, $P_i = 7.6$ MPa, and $T_0 = 275\,\text{K}$. The horizontal dashed lines in the temperature distribution diagrams (Figure S1) represent the temperature at the dissociation interface separating Zone I from Zone II. The trends for temperature and pressure distributions reported Selim and Sloan (Selim and Sloan 1990) is similar to those of the case with line heat source. Tsimpanogiannis and Lichtner (Tsimpanogiannis and Lichtner 2007), who built up a semi-analytical 1D model based on the work of Selim and Sloan (Selim and Sloan 1990) without the wellbore structure, showed that the higher temperatures of the heat source increased the interface pressure. The results of temperature distribution are also consistent with an experimental work performed by Li et al. (Li et al. 2011b) on MH dissociation upon thermal stimulation. They reported that the dissociation progressed by a moving boundary interface. Figure 18 shows the volume of gas produced (m^3) under STP conditions in both

cases in response to different heat sources, as well as the amount of input heat (MJ/m^2), and energy efficiency for the model with wellbore heating considering two BCs over 100 days.

Various researches have experimentally investigated MH dissociation by hot water circulation in a reservoir. for instance, using this approach, Song et al. (Song et al. 2015) experimentally achieved a similar trend for the energy efficiency of gas production from MH . Their reported energy efficiency of 18 and 40, is in good agreement with the present results. Wang et al. (Wang et al. 2014b) also found the same energy efficiency and gas production trends, and Li et al. (Li et al. 2014; Li et al. 2011a) for a 5.8 L cubic reactor, observed that the energy efficiency of the process is approximately 20.6. Wang et al. (Wang et al. 2013) reported an energy efficiency between 6 and 20. Tang et al. (Tang et al. 2005) reported that increasing the hot water temprature and decreasing the pressure of the wellbore improve the energy ratio (the same as the energy efficiency) of MH dissociation.

Taking a different approach, Bayles et al. (Bayles et al. 1986) analytically studied MH dissociation upon cyclic steam circulation into the reservoir, and reported the same energy efficiency trend, convergence between 4 to 9.6, and gas production over one year's dissociation. The slight difference between their results and those reported hear probably results from the direct steam circulation into the reservoir and the cyclic pattern of their process.

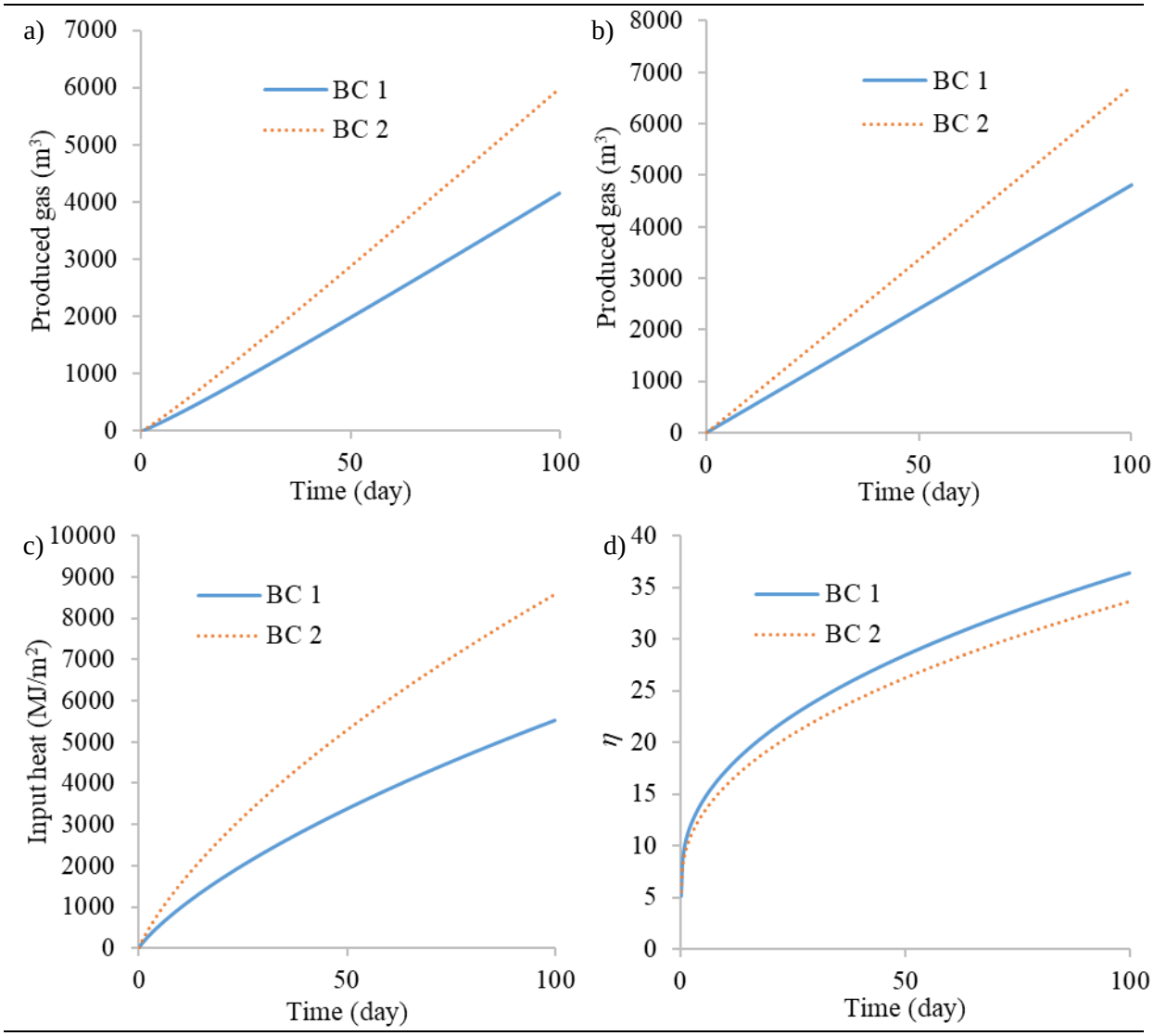

Figure 18. a) volume of gas produced in the wellbore-heat-source model, b) volume of gas produced in the line-heat-source model, c) amount of input heat in the wellbore-heat-source model, and d) energy efficiency during hydrate dissociation in the wellbore-heat-source model for two BCs.

A parametric study is employed to investigate the effect of various parameters (Table 2) on the dissociation process. Figures 19 and 20 respectively show the dissociation rate and gas-production resulting from the study. Figures S3 and S4 (Appendix A) respectively display the heat input from the wellbore to the reservoir and the energy efficiency in the wellbore-heat-source case. Increasing the thermal conductivity of Zone I significantly increases the amount

of heat input from the reservoir (Figure S1a). Higher thermal diffusivity (lower heat capacity while the density is constant) makes the media to store less heat, which in turn, increases the heat transferred to the dissociation front. Eventually, higher thermal diffusivity and higher thermal conductivity increase the dissociation rate (Figure 19a) and gas production (Figure 20a). Lower thermal diffusivity in Zone II increases the storage of the heat transferred to this zone from the dissociation interface. Ultimately, this stored heat is released and consumed by dissociation, increasing the dissociation rate (Figure 19b). Higher thermal conductivity in Zone II reduces the dissociation rate and gas production because heat is being transferred to this zone from the moving interface more quickly than when it is consumed by dissociation. Higher thermal diffusivity in Zone II increases gas production (Figure 20b) because the heat storage reduction in this zone induces more heat consumption by dissociation and more gas production. Lower thermal diffusivity and higher thermal conductivity in Zone II increases the input heat (Figure S3b) for the same reason stated for input heat increment induced by the same changes in Zone I (Figure S3a). However, the input heat increment for Zone II is much lower than that of Zone I due to Zone I's direct contact with the wellbore. The energy efficiency in the case with wellbore heating has a direct relation to the thermal diffusivity of Zones I and II (Figures S4a and S4b). On the other hand, energy efficiency decreases with increasing thermal conductivity in Zones I and II. Higher porosity reduces the conduction heat transfer and the heat input from the wellbore (Figure S3c), ultimately reducing the dissociation rate (Figures 19c and 19d). Furthermore, higher porosity increases the amount of MH trapped in the pores, eventually increasing the amount of gas produced (Figures 20c and 20d). Clearly, reservoir porosity has a direct relation on the energy efficiency of dissociation. Various permeabilities of media and gas viscosities have no impact on the dissociation process.

Selim and Sloan (Selim and Sloan 1990) reported similar results for dissociation rate (Figure 19) during similar parametric studies. Zhao et al. (Zhao et al. 2015) mathematically showed that increasing thermal conductivity had a direct positive effect on the dissociation process using hot water circulation in the reservoir; although water and gas relative permeabilities have almost no impact on the process. In another numerical work, they showed that

increasing sediments' thermal conductivity increased the gas generation rate at the beginning of dissociation upon depressurization (Zhao et al. 2014). Both these works were verified against Masuda's experimental work (MASUDA 1999). Tsimpanogiannis and Lichtner (Tsimpanogiannis and Lichtner 2007) showed that increasing the porous media's thermal conductivity increased MH dissociation. Moridis et al. (Moridis et al. 2004) conducted numerical analyses of various gas production scenarios from MH zones at the Mallik site and showed that a higher initial formation temperature, well temperature, and formation thermal conductivity increased gas production; although it is not affected by the formation's permeability and the specific heat of the rock and MH. It should be noted that the difference between the results of experimental works and the present work, which is not significant, is due to some of different working conditions, such as direct hot water circulation into the reservoir, time period of experiments, and model parameters (i.e. hydrate saturation).

Table 5. Range of parameters employed in the parametric study.

Porosity, ϕ	0.1 to 0.5
Permeability, k, μm^2	0.1 to 5
Zone I thermal diffusivity, α_I, $\mu m^2/s$	1×10^6 to 5×10^6
Zone I thermal conductivity, k_I, W/(m.K)	3 to 7
Zone II thermal diffusivity, α_{II}, $\mu m^2/s$	4×10^5 to 8×10^5
Zone II thermal conductivity, k_{II}, W/(m.K)	1 to 5
Gas viscosity, μ, Pa.s	10^{-4} to 10^{-6}

a)

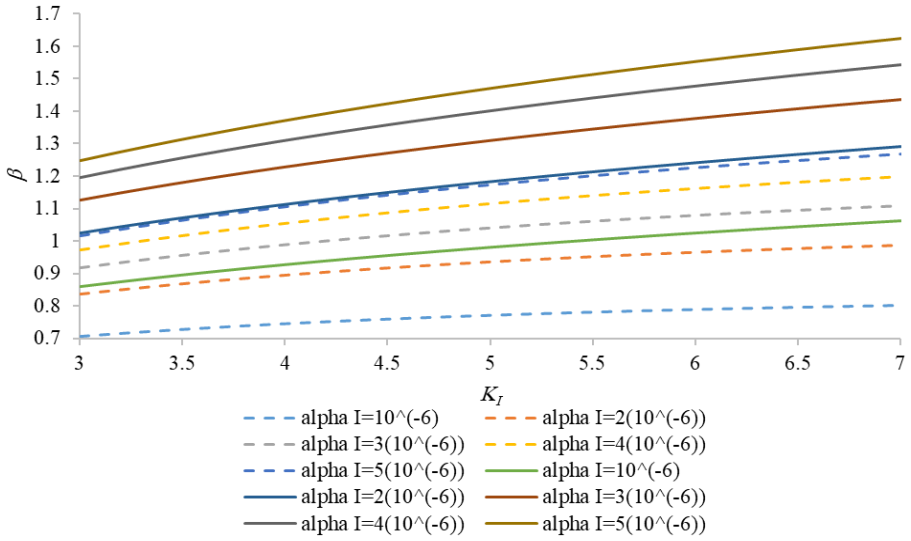
β
K_I
alpha I=10^(-6)
alpha I=2(10^(-6))
alpha I=3(10^(-6))
alpha I=4(10^(-6))
alpha I=5(10^(-6))
alpha I=10^(-6)
alpha I=2(10^(-6))
alpha I=3(10^(-6))
alpha I=4(10^(-6))
alpha I=5(10^(-6))

b)

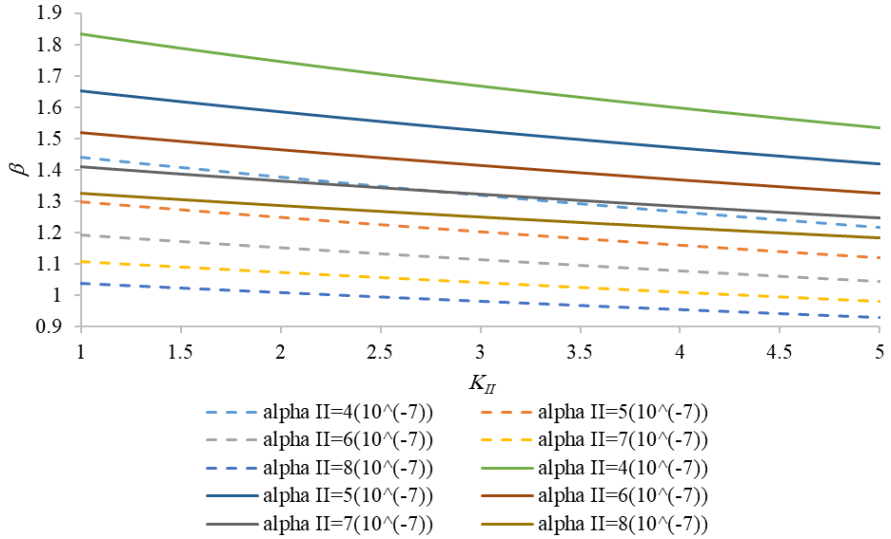
β
K_{II}
alpha II=4(10^(-7))
alpha II=5(10^(-7))
alpha II=6(10^(-7))
alpha II=7(10^(-7))
alpha II=8(10^(-7))
alpha II=4(10^(-7))
alpha II=5(10^(-7))
alpha II=6(10^(-7))
alpha II=7(10^(-7))
alpha II=8(10^(-7))

c)

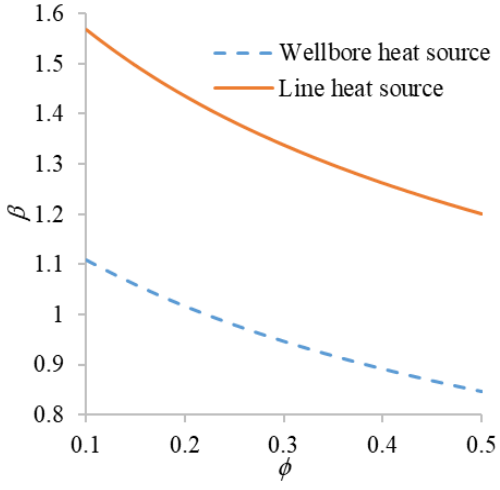
Wellbore heat source
Line heat source
β
ϕ

d)

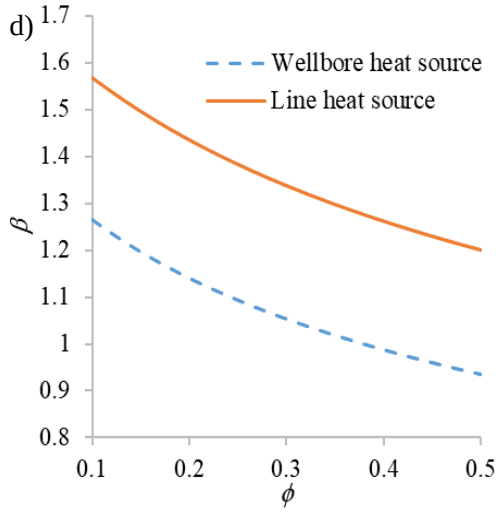
Wellbore heat source
Line heat source
β
ϕ

Figure 19. Effect of various parameters on the interface movement after 100 days dissociation considering both types of heat sources: a) thermal diffusivity and thermal conductivity of Zone I, b) thermal diffusivity and thermal conductivity of Zone II, c) porosity with various permeabilities, and d) porosity with various gas viscosities.

Dashed lines and solid lines respectively represent the wellbore-heat-source and the line-heat-source models.

a)

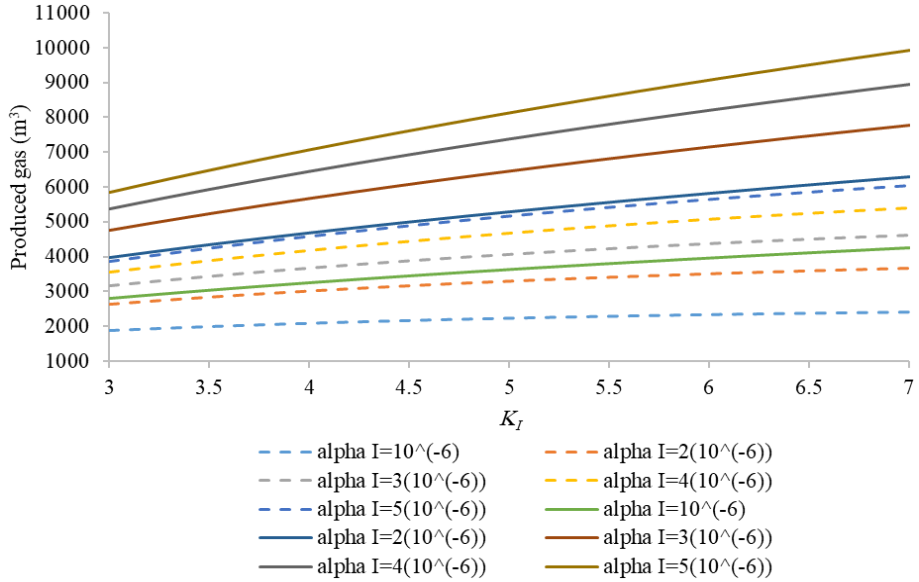

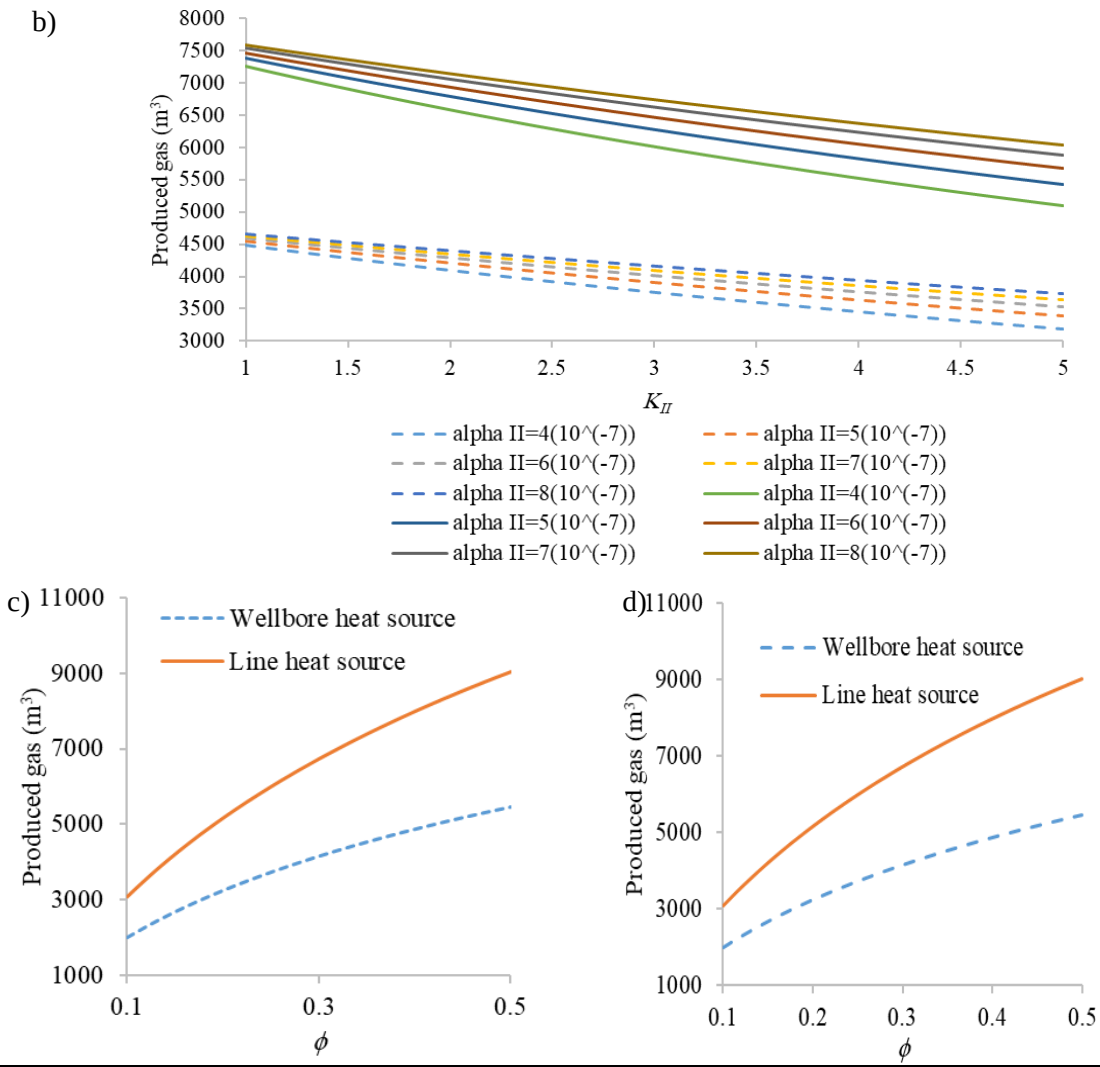

Figure 20. Produced gas after 100 days dissociation considering both heat sources and various parameters: a) thermal diffusivity and thermal conductivity of Zone I, b) thermal diffusivity and thermal conductivity of Zone II, c) porosity with various permeabilities, and d) porosity with various gas viscosities.

Dashed lines and solid lines respectively represent the wellbore-heat-source and the line-heat-source models.

The present results in this part are a follow-up of the previous part (3.1)on MH dissociation upon thermal stimulation, in which the wellbore structure effect on MH dissociation upon

wellbore heating was assessed using a 1D analytical model in Cartesian coordinates. This 1D model is extended to radial models by employing analytical approaches coupling the heat and mass transfer with MH dissociation in radial coordinates. Furthermore, two types of heat source are assumed: i) wellbore heat-source with a specific radius and external layers; and ii) line heat-source. Variable temperature at the wellbore surface due to the heat transfer in the external layers causes lower dissociation rate, which is also inconstant, and produced gas compared to those of the line-heat-source case. Although, the results reveal good agreement with the previous similar experimental and mathematical studies; none of the previous investigations analytically investigated the MH dissociation in radial coordinates upon wellbore heating by involving the effect of wellbore structure.

The magnitude of β (Figure 17) is lower than those reported by Selim and Sloan (Selim and Sloan 1990) (approximately 32% lower than the line-heat-source case) and those of the previous part (3.1) (approximately 25% lower than the wellbore-heat-source case) due to the radial coordinate employed in this study. These results further prove that the dissociation rate is not constant and depends on the temperature at the wellbore surface, which changes by the conduction heat transfer in the wellbore structure.

The effect of temperature increment of the wellbore's outer surface on the interface temperature becomes negligible as the dissociation progresses because over time, this temperature increment decreases (Figure S1) and Zone I becomes bigger, absorbing larger part of the heat transferred from the wellbore. The distance between the dissociation interface and the heat source is longer in the line-heat-source model (Figures S1c and S1d) compared to that of the wellbore-heat-source model (Figures S1a and S1b). This is due to the direct heat transfer from the line heat-source to the reservoir that causes higher dissociation rate, while there is heat conduction in the wellbore thickness in the other model. This difference decreases over time as Zone I absorbs larger amount of input heat, which reduces the negative effect of heat source thickness on the dissociation rate. Interface pressure (Figures S2a and S2b) is not constant and increases due to the temperate increment at the wellbore surface, but, tends to converge to the associated values of the line-heat-source case (Figures

S2c and S2d) as the temperature at the well surface gets closer to that of inside the well. Relatively smaller interface locations are reported by Selim and Sloan (Selim and Sloan 1990) and in the previous model (3.1) compared to those presented in Figures S1 and S2 due to the radial coordinates employed in the present model, inducing the interface area increment through the dissociation and absorption of higher amount of input heat by Zone I.

The gas produced is higher for the line-heat-source case compared to that of the wellbore-heat-source case due to the interface location mentioned earlier (Figures 18a and 18b). The gas produced and the input heat are higher by applying BC 2 compared to that of BC 1 (Figures 18a-18c). However, the energy efficiency is higher in the BC 1 case compared to that of BC 2 (Figure 18d) because the difference between the amount of input heat for the two BCs is higher than the difference between the associated amounts of produced gas. Thus, increasing the heat source temperature and decreasing its pressure increase the dissociation rate, but will not increase the efficiency of the process because Zone I becomes bigger and absorbs a larger part of the input heat, decreasing the slope of produced gas and energy efficiency. Selim and Sloan (Selim and Sloan 1990) reported higher produced gas and energy efficiency by applying BC2 compared to those of BC1. They also showed a constant energy efficiency between 6.4-11.2. The heat transfer in the wellbore structure and the radial geometry of the present study caused these differences from the present results. The previous part (3.1) showed the similar trends for input heat and produced gas by applying the same initial and boundary conditions. Furthermore, higher energy efficiency for BC1 is reported than that of BC2, but the associated trend of energy efficiency had a maximum peak in the beginning of the dissociation, then it decreased over time. As mentioned, this behavior is due to the employed model geometry.

Lastly, the previous studies (mentioned before) mainly investigated effects of reservoir's characteristics on the produced gas and dissociation rate without assessment of the associated effects on the input heat from the wellbore (Figure S3) and the energy efficiency (Figure S4), which would also clarify the results shown in Figures 19 and 20. The present results reveal that higher thermal conductivities of Zones I and II decrease the energy efficiency; although

the produced gas is increased in higher Zones I's thermal conductivities. This is due to: i) the input heat increment induced by higher thermal conductivities (more pronounced for Zone I) (Figure S3a); and ii) the lower gas production caused by increasing Zone II's thermal conductivity. Increasing thermal diffusivities causes higher gas production and lower input heat resulting in higher energy efficiencies. Furthermore, the effect of thermal diffusivity of Zones I and II on the energy efficiency is more pronounced respectively in lower and higher thermal conductivities of Zones I and II. Higher thermal conductivities always increase the input heat, but higher porosity decreases it, inducing significant raise in the energy efficiency.

3.3 Radial model with the coaxial wellbore heat source

Pressure and temperature at the dissociation interface (P_s and T_s) are coupled to the pressure and temperature at the wellbore (outer surface of the wellbore) due to their associated equations, mentioned earlier in the modeling section. Thus, The dimensionless position and dimensionless velocity ($v_s / (4\alpha_{II} t)^{1/2}$) of the dissociation interface, both represented by β (equation 45), which are connected to P_s and T_s (equation S72), are related to the pressure and temperature at the wellbore. The temperature at the outer surface of the wellbore is dependent on the temperature of the annulus section and time. The temperature inside the wellbore changes due to time and the temperature at the wellbore, which changes over time as the dissociation progresses. Table 6 shows the proposed properties and parameters for the base model according to previous studies (Acuña and Palm 2010; Beier et al. 2013; Cheng et al. 2011; Dalla Santa et al. 2017; Holmberg et al. 2016; Majorowicz and Osadetz 2001; Remund 1999; Selim and Sloan 1990).

As shown in Figure 21a, β decreases at the beginning of the process because the thickness of Zone I increases over time, and the associated matrix in this zone absorbs a higher amount of transferred heat. Thus, dissociation is responsible for most of the energy consumption in the early stages of the process. But the energy consumption converges to a fixed value because the temperature at the wellbore surface is also converging slightly to that of inside of

the well (T_{fa}). Figure 21b shows the location of the interface (S) during the process. The slope in the diagram is the highest at the beginning, but it decreases over time, which supports the observations from previous studies (Moridis et al. 2004; Song et al. 2015; Wang et al. 2014b). This behavior is in line with β, which decreases significantly at the beginning but slightly converges to a constant value, and can be justified for the same reasons. Wang et al. (Wang et al. 2013) and Li et al. (Li et al. 2014; Li et al. 2011a), who experimentally investigated the hydrate dissociation upon thermal stimulation, also proved that at the beginning of the dissociation process, the rate of dissociation close to the wellbore is the highest. Variable dissociation rates (β) are reported in the previous parts (3.1 and 3.2) due to the variable temperature at the wellbore. When hot water is injected through the annulus, temperature distribution through this section, from which the heat transfer to the reservoir takes place, is higher, as shown in Figures 21c and 21d, inducing slightly higher values for β and S compared to those of the other operating scheme. The temperature difference becomes significant through the extraction part especially at the beginning of the process (Figures 21c and 21d). However, the associated differences decrease as the process continues to 100 days. This behavior was also reported by Beier et al. (Beier et al. 2013) who analytically and experimentally investigated the temperature distribution in the coaxial heat exchangers as ground source heat pumps.

Table 6. Parameters used for the base model.	
r_1, m	0.043
r_2, m	0.05
r_3, m	0.07
r_4, m	0.077
r_5, m	0.092
r_6, m	0.099
r_7, m	0124
Methane hydrate thickness, m	80
Thermal conductivity of inner tube (polyethylene tube), k_p, W/(m.K)	0.4
Thermal conductivity of cement, k_c, W/(m.K)	0.933
Thermal conductivity of gravel, k_g, W/(m.K)	0.4
Thermal conductivity of casing (steel), k_s, W/(m.K)	43.3
Thermal conductivity of water, k_f, W/(m.K)	0.667
Density of water, ρ_f , kg/m^3	971.79
Dynamic viscosity of water, μ_f , Pa.s	3.54×10^{-4}
Specific heat capacity of water, C_f, kJ/(kg.K)	3.89
Porosity, ϕ	0.3
Water flow rate, V_f , L/s	0.56
Permeability, k, μm^2	1
Thermal diffusivity of Zone I, α_I , μm^2/s	2.89×10^6
Thermal conductivity of Zone I, k_I , W/(m.K)	5.57
Thermal diffusivity of Zone II, α_{II} , μm^2/s	6.97×10^5
Thermal conductivity of Zone II, k_{II} , W/(m.K)	2.73
Hydrate density, ρ_H , kg/m^3	913
Heat of dissociation of hydrate, Q_{Hd} , J/kg	$446.12\times10^3 - 132.638T_s$
Gas heat capacity, C_{pg} , J/(kg.K)	8766
Dynamic viscosity of gas, μ , Pa.s	10^{-4}
Heating value of the gas at STP conditions, Q_g , MJ/m^3	37.6
Molecular mass of methane, m, g/mol	16.04
Mass ratio of the methane gas trapped inside the hydrate to the mass of hydrate, F_{gH}	0.1265
Universal gas constant, R, J/(mol.K)	8.314

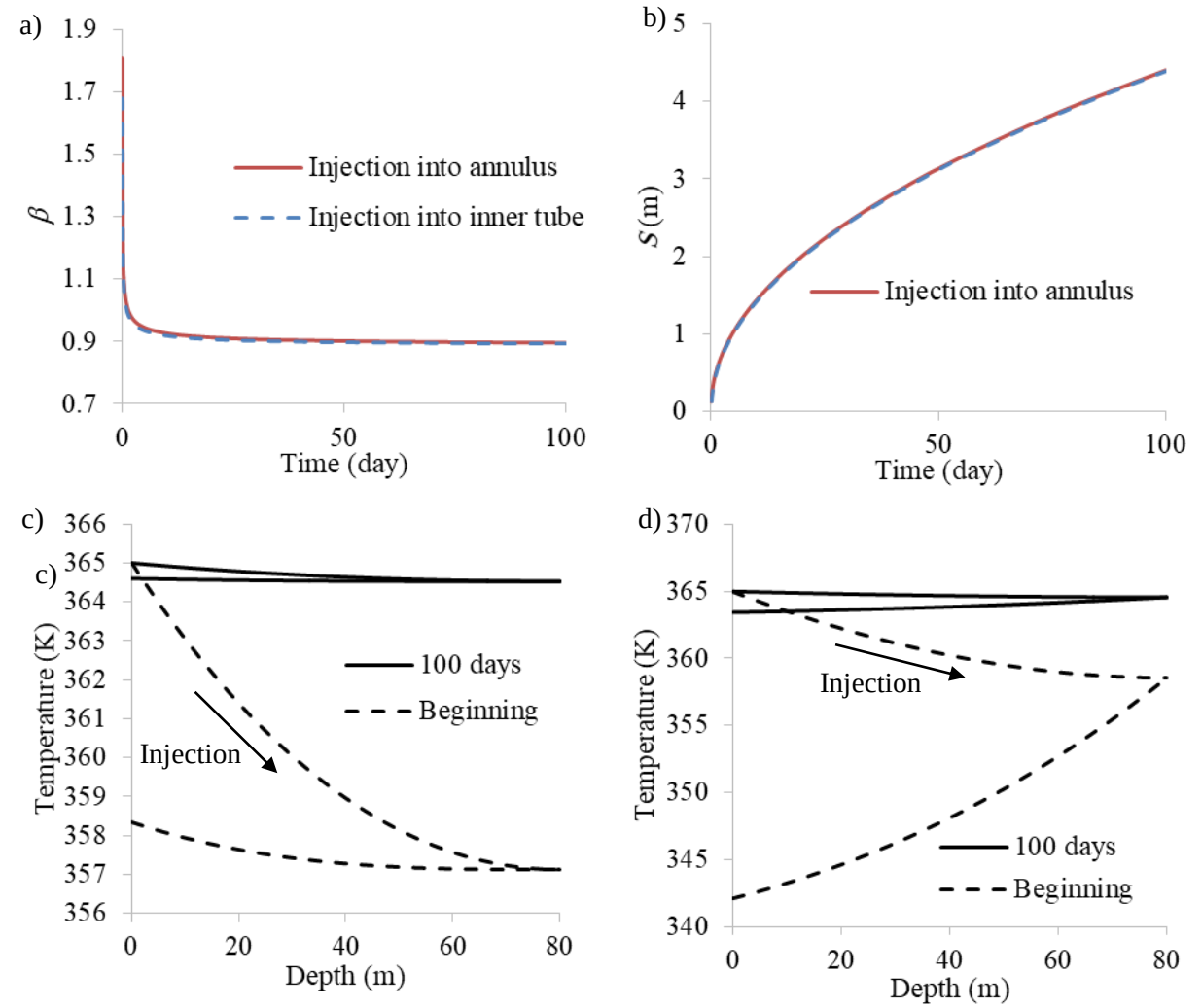

Figure 21. Variation of a) β and b) interface location versus time for the two operation schemes. Temperature distribution in the wellbore versus depth when hot water is injected into c) inner tube and d) annulus. The conditions are: T_0=280 K and T_i=365 K, P_i=7.6 MPa, and a water flow rate of 0.56 L/s.

Figure 22a shows that decreasing the pressure at the wellbore and increasing the temperature of injected water decrease the value of β after 100 days operation. Further information of the effect of the injected water temperature on dissociation is provided in the following results. The initial temperature of MH also has a direct effect on β as shown in Figure 22b. These results are consistent with those of the previous work by Selim and Sloan (Selim and

Sloan 1990) with the same trend, but β is lower (approximately 48%) in the present model. Previous models (3.1 and 3.2) also reported the same behavior for β against various initial pressures and temperatures, but with higher values (approximately 26% and 66%). These differences could be due to the following reasons: i) in the work performed by Selim and Sloan (Selim and Sloan 1990), a 1D flat heat source without wellbore thickness was considered; and ii) in the previous work (Selim and Sloan 1990) and previous sections (3.1 and 3.2) temperature of the heat source was assumed to be very high and constant.

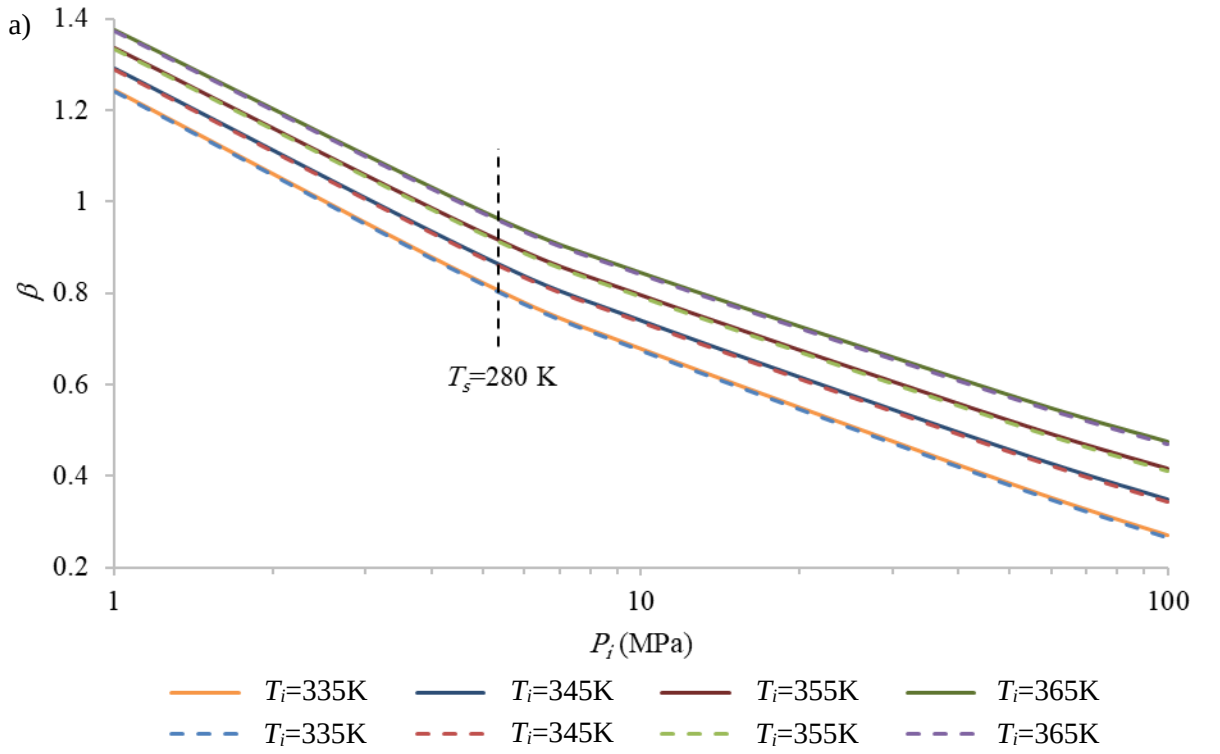
a)
1.4
1.2
1
0.8
0.6
0.4
0.2
β
T_s=280 K
1
10
100
P_i (MPa)
T_i=335K
T_i=345K
T_i=355K
T_i=365K
T_i=335K
T_i=345K
T_i=355K
T_i=365K

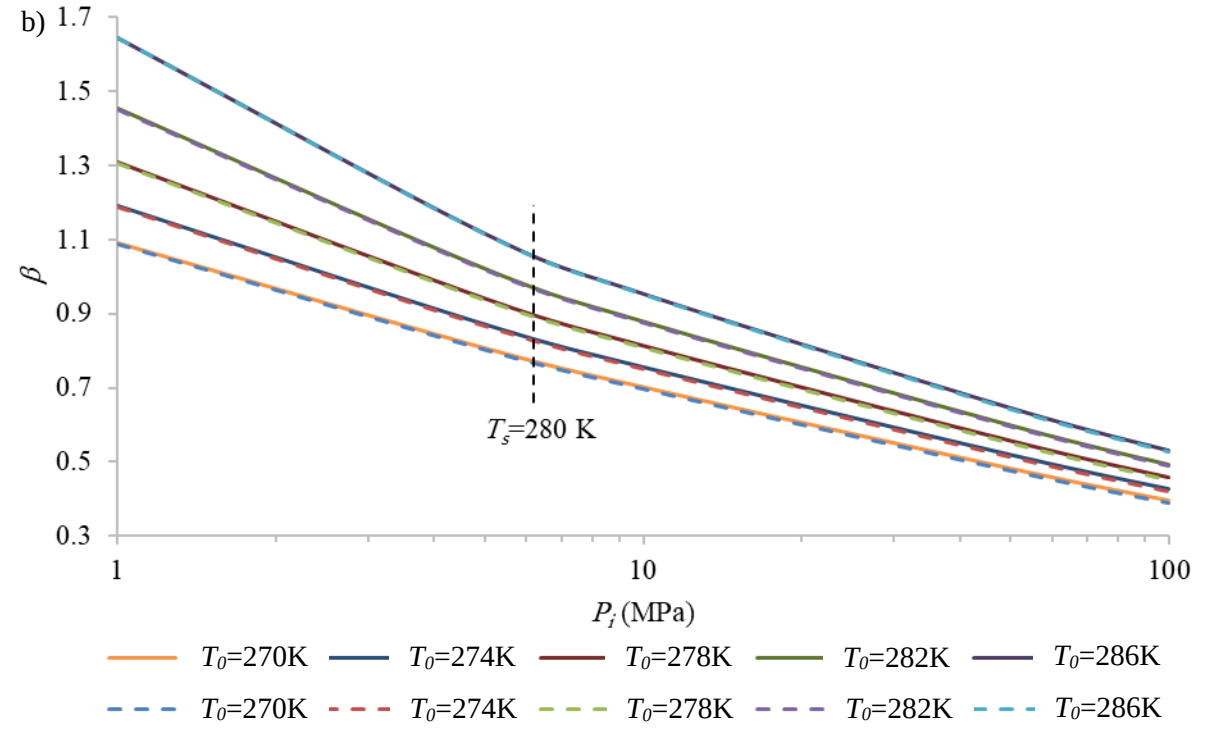
b)
1.7
1.5
1.3
1.1
0.9
0.7
0.5
0.3
β
T_s=280 K
1
10
100
P_i (MPa)
T_0=270K
T_0=274K
T_0=278K
T_0=282K
T_0=286K
T_0=270K
T_0=274K
T_0=278K
T_0=282K
T_0=286K

Figure 22. Dimensionless interface position at: a) T0=280 K and various Ti and Pi values, and b) Ti=365 K and various T0 and Pi values. Dashed lines and solid lines respectively represent the cases with hot water injection into the inner tube and the annulus.

Furthermore, the locus at which the dissociation temperature is equal to 280 K (MH equilibrium temperature) is also shown on Figure 22. At the points on the left and right sides of this locus, the dissociation temperature decreases and increases, respectively. The dissociation temperature could be considered to be mainly dependent on heat source pressure, while it is almost independent from the temperature of the heat source and MH. This result is in agreement with the previous work (Selim and Sloan 1990) and previous models (3.1 and 3.2), where it was also reported that for lower heat source pressures of 6 MPa, T_s may reduce to the freezing temperature of water, and ice generation can halt dissociation. For the situations, in which T_s is higher than the MH temperature, some part of input heat from the heat source will be consumed to increase the temperature of MH zone close to the dissociation front to T_s. If T_s approaches T_0 all heat from the heat source is consumed for dissociation and no heat will be transferred to or from the MH zone near the dissociation interface as the temperature of the hydrate zone remains constant. On the other hand, if T_s falls below T_0, some part of the required heat for dissociation will be provided from the hydrate zone, resulting in the temperature reduction of the hydrate zone near the dissociation interface.

Temperature and pressure distributions calculated for the two operation schemes are respectively depicted in Figures 23 and 24 for different time frames, with the following two boundary conditions (BCs): BC 1) $T_i = 340\,\text{K}$, $P_i = 10\,\text{MPa}$, and $T_0 = 280\,\text{K}$, and BC 2) $T_i = 365\,\text{K}$, $P_i = 7.6\,\text{MPa}$, and $T_0 = 275\,\text{K}$. It should be noted that the temperature of the injected water is below the saturation temperature of water. Black dashed lines in Figure 23 represent the temperature at the dissociation interface. Although, as mentioned earlier, T_s depends on the temperature at the wellbore and does not change significantly (Figure 23) because the temperature increase at the wellbore becomes smaller in longer time frames for

the reasons stated earlier for the trend of β during the process. Figures 23 and 24 along with Figure 22 show that the interface moves further if the inlet temperature is increased and the pressure at the wellbore is decreased, again reflecting reports by Selim and Sloan (Selim and Sloan 1990). The interface pressure (Figure 24) is not constant and increases due to temperate changes at the wellbore surface. The pressure increment does not follow a constant slope and decreases as the temperature at the wellbore surface gets closer to that inside the well. Thus, it does not change significantly, resulting in convergence of the interface pressure. These results are in line with those reported in the previous sections (3.1 and 3.2), mainly because the temperature at the wellbore was not constant in those models due to the heat conduction through the wellbore structure. In accordance with the present results, a study by Tsimpanogiannis and Lichtner (Tsimpanogiannis and Lichtner 2007), who built a semi-analytical model for hydrate dissociation, demonstrated that increasing the temperature of the wellbore raised the pressure at the interface. The temperature distribution differences between the two operation schemes is negligible, with only slightly higher temperature at the wellbore upon injection into the annulus, causing higher dissociation pressures and farther interface location from the wellbore.

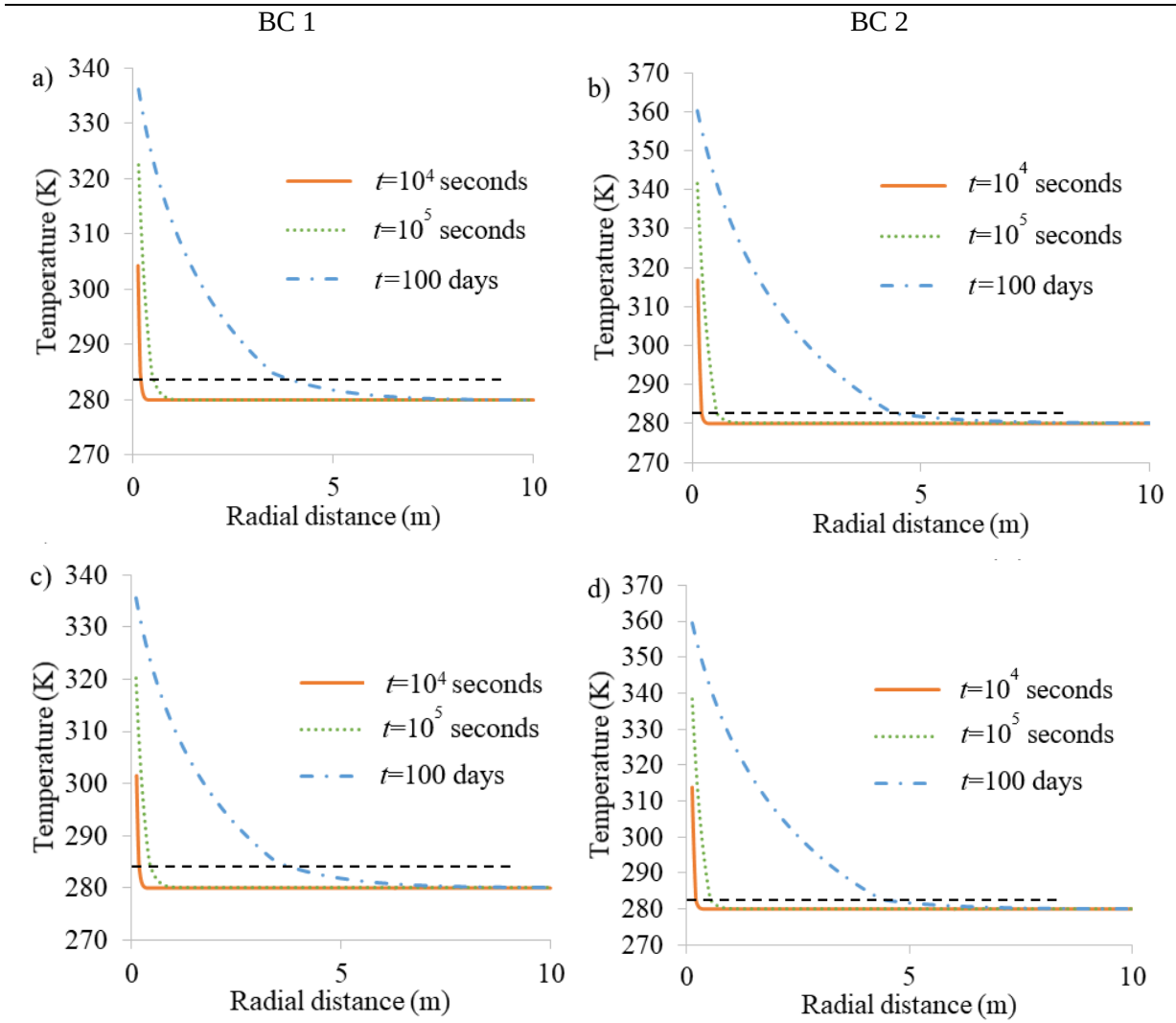

Figure 23. Temperature distribution at different time frames for two initial and boundary conditions (i.e., BC 1: a and c, BC 2: b and d). a) and b) are for hot water injection into annulus, and c) and d) are for hot water injection into the inner tube. The black dashed line specifies the temperature at the dissociation interface.

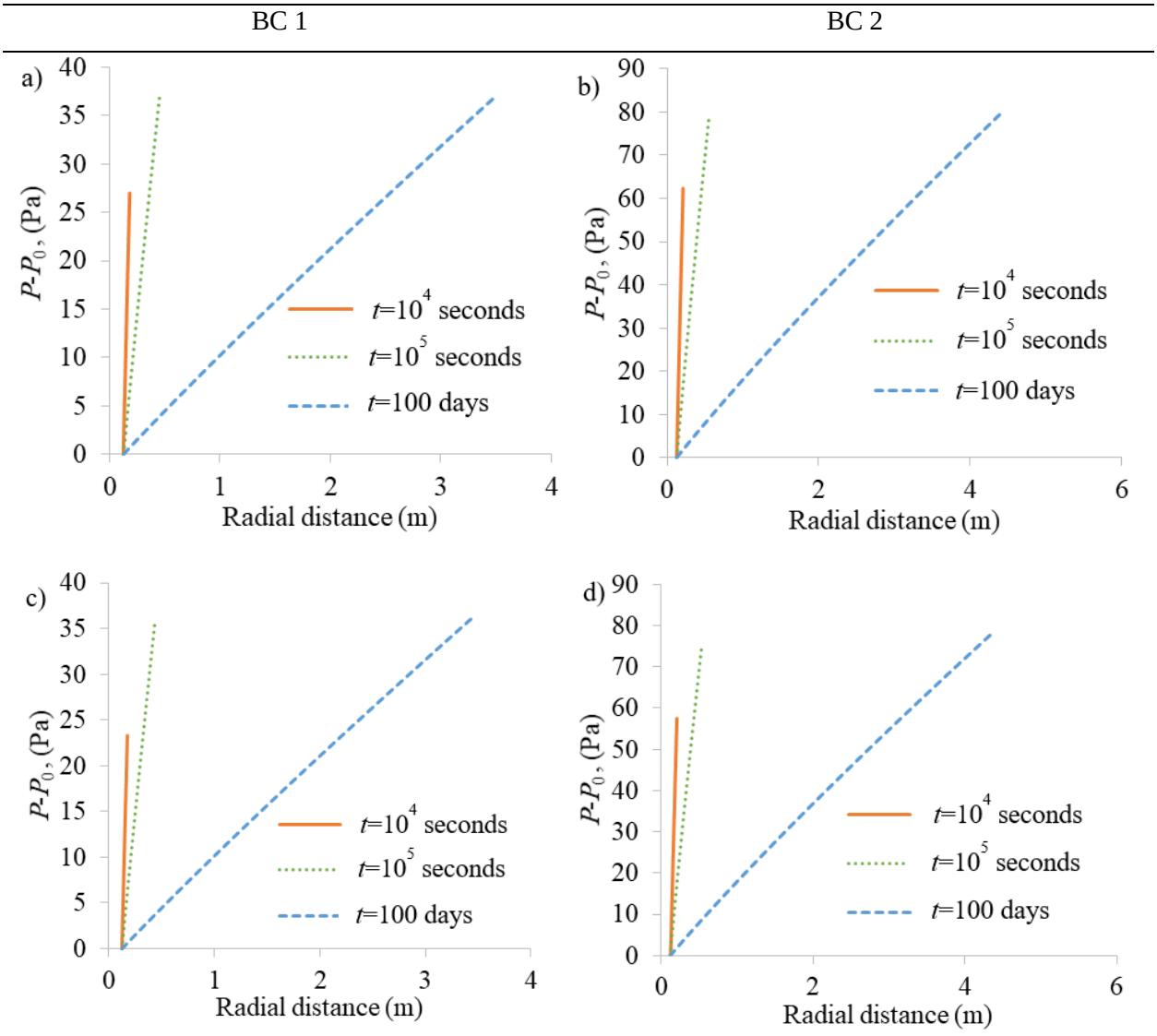

Figure 24. Pressure distribution in the dissociated zone at different time frames for two initial and boundary conditions (i.e., BC 1: a and c, BC 2: b and d). a) and b) are for hot water injection into annulus, and c) and d) are for hot water injection into the inner tube.

Figure S5 shows the total volume of produced gas (m^3) under STP conditions, and input heat (MJ/m^2) in two models with their specific operation schemes, considering the two initial and boundary conditions over 100 days. The produced gas volume is almost the same for both models, with slightly higher values for the case with hot water injection into the annulus, due

to the direct heat transfer from heat source to reservoir. Beier et al. (Beier et al. 2013), who analytically investigated borehole heat exchangers and verified their results against experiments, reported the same heat transfer to the earth following injection into the inner tube or annulus. Holmberg et al. (Holmberg et al. 2016) performed and validated a set of numerical investigations on underground coaxial borehole heat exchangers and reported that different flow directions have almost the same efficiency. Figures S5c and S5d also show a negligible difference between the amount of heat transfer to the reservoir following injection into the inner tube or annulus. The produced gas and the input heat are higher under BC 2 than BC 1. The energy efficiency is higher in the model with BC 2 than that with BC 1 as shown in Figure 25, demonstrating that lowering the pressure at the wellbore and increasing the inlet temperature simultaneously result in more efficient gas production during dissociation. Over time, the sediment matrix of Zone I becomes wider and absorbs a larger part of the input heat, causing reduction of the energy efficiency slope. This phenomenon causes the decrease in the dissociation rate (Figure 21a), which also causes the energy efficiency rate to drop over time (Figure 25) due to the continuous input heat increase from the wellbore to the reservoir (Figure S5). However, the energy efficiency does not drop because according to the associated formula for the energy efficiency (Equation 41) and Figure S5, the energy retrieved by the total produced gas consumption is higher than the input heat from the wellbore. The results provided in the previous section also show a similar trend for energy efficiency. Li et al. (Li et al. 2016a), who experimentally and numerically investigated gas production from MH using depressurization and thermal stimulation with hot water injection into horizontal wells, reported the net energy, which is the difference between the total retrieved energy by produced gas consumption and the total energy consumption in the dissociation, through MH dissociation is positive and increased continuously, but, the rate of net energy raise decreased. This report also implies a continuous raise and drop respectively in the energy efficiency and its associated rate because the total retrieved energy by produced gas consumption is higher than the total energy consumption in the dissociation. In an experimental work on gas production from MH using depressurization and electrical heating with vertical wells (Li et al. 2018), the same

results also reported using the net energy calculation through the process. Fitzgerald et al. (Fitzgerald and Castaldi 2013) through experiment on MH dissociation using a point heat source reported energy efficiency reduction from a high value over time. Li et al. (Li et al. 2014), who performed experimental study on MH dissociation using thermal stimulation, reported that the energy efficiency increases over 20 minutes after the beginning of the process, then starts to decrease. Li et al. (Li et al. 2011a) designed experimental investigation on gas production from MH dissociation using huff and puff and reported that the energy efficiency raises until the end of the production stage, then drops until the end of the process. The difference between the energy efficiency results of the present work and those of the other work originated from the different model and working conditions, such as direct hot water injection into the reservoir, employing point heat source, and electric heat source, on the other hand, we employed a coaxial heat exchanger as the heat source.

Experimental researches investigated MH dissociation upon thermal stimulation by hot water circulation in a reservoir. For example, Song et al. (Song et al. 2015) by using this method reported the same trend for energy efficiency in their experimental work. The energy efficiency in their work was between 18 and 40. Figure 25c shows a comparison of the energy efficiency results of the previous experimental works and the energy efficiency resulted from the case of hot water injection into the annulus in a shorter time frame. Comparison of gas production results with those of Wang et al. (Wang et al. 2014b), who performed an experimental work employing huff and puff method, shows the similar trend. Their energy efficiency results also shows a good agreement with the present ones (Figure 25c) with an approximate mean difference of 30%, which is due to the huff and puff method employed along heat stimulation method by direct hot water injection into the reservoir in their work. The present results are consistent with the experimental data of Li et al. (Li et al. 2014; Li et al. 2011a), who also employed huff and puff method in a 5.8 L cubic reactor. The calculated energy efficiency of the process was approximately 20.6 at the end of the process and the produced gas had the similar trend as that of the present work. The present energy efficiency results show an approximately 39% and 83% mean difference respectively from results of Li et al. (Li et al. 2011a) and Li et al. (Li et al. 2014) (Figure 25c), although, the

they tend to gradually converge to those reported by them as the dissociation progresses (Figure 25c). These relatively high differences are due to the experimental conditions, for example employing only huff and puff method (Li et al. 2011a) and direct hot water injection into the reservoir accompanied by depressurization in production stage (Li et al. 2014). Wang et al. (Wang et al. 2013) also reported an energy efficiency of between 6 and 20 during their experimental investigations on MH dissociation upon hot water injection using different initial and boundary conditions. According to Figure 25c, their energy efficiency results differ approximately 39% from those of the present study. This could be due to the direct hot water injection into the reservoir and a small depressurization effect applied in their work in production stage. Additionally, the present energy efficiency tends to converge to their results over time (Figure 25c). The associated difference between the present results and those of the previous works could be due to some experimental conditions, such as direct hot water circulation into the reservoir or other thermal stimulation methods (e.g., huff and puff) or they combination with depressurization. It also should be noted that the wellbore structure, geometry, and performance mechanism (inside thermal and fluidic processes), which have been considered in the present study, have also noteworthy effects on those differences.

Selim and Sloan (Selim and Sloan 1990) in their analytical work reported an energy efficiency between 6.4-11.2, which remained constant during the process. Some of the assumptions in their work, which are mentioned earlier, are the reasons of the difference between the present results and theirs.

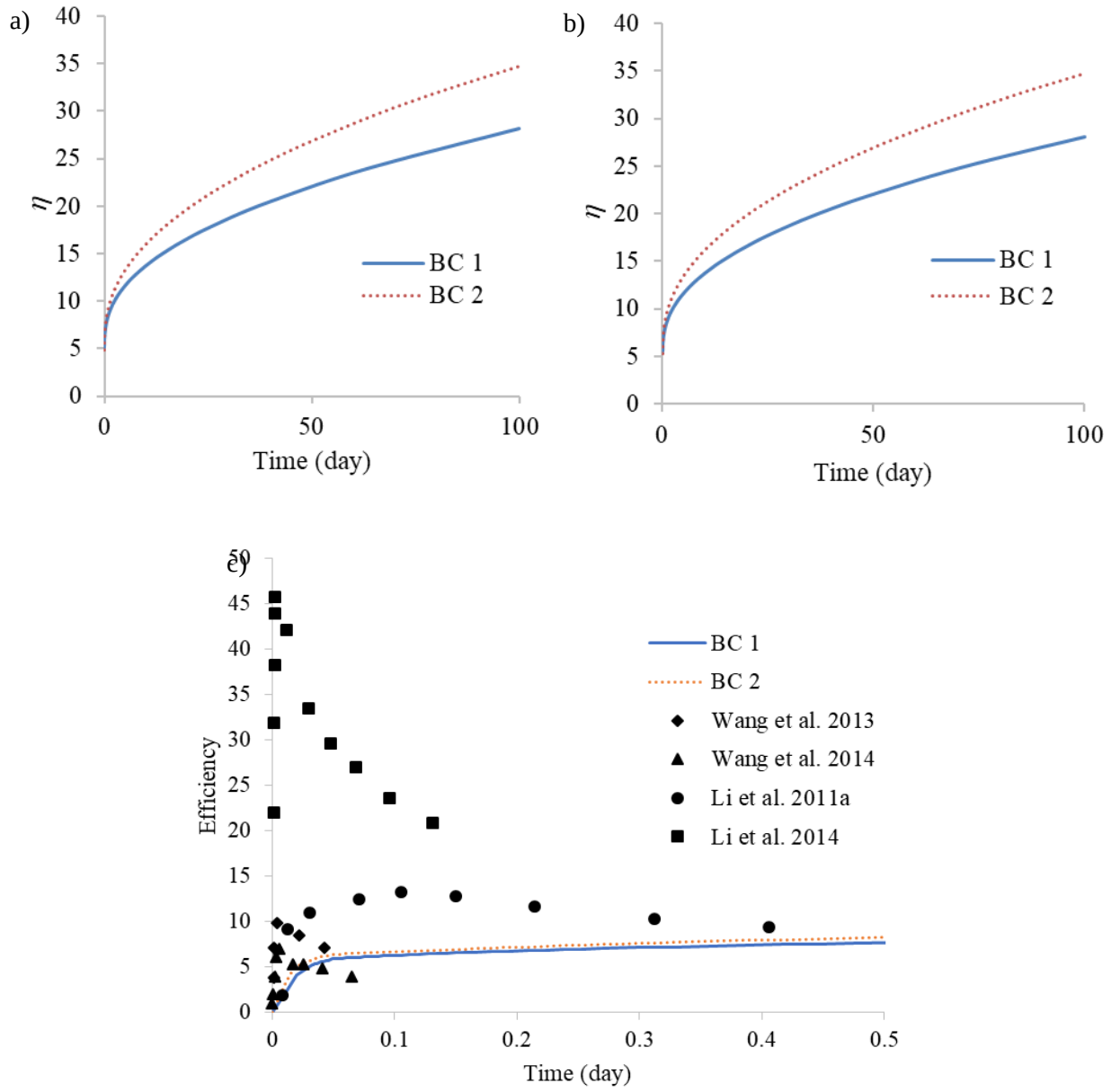

Figure 25. Energy efficiency during hydrate dissociation for the two BCs in the model with hot water injection into the a) annulus and b) inner tube after 100 days of process. c) energy efficiency of the case with hot water injection into the annulus in a shorter time frame compared to the results of the previous experimental works.

A parametric study has been designed based on the parameters listed in Table 7, to investigate the effect of various characteristics of reservoir and wellbore on the dissociation

process. From Figures 26 and 27: i) the higher the thermal diffusivities and conductivities of Zone I, the higher the dissociation rate and gas production will be; ii) the lower the thermal diffusivities and conductivities of Zone II, the higher the dissociation rate will be, on the other hand, higher thermal diffusivities and lower thermal conductivities induce more gas production; iii) the dissociation rate and gas production have almost no connection to the permeability and gas viscosity; and iv) the porosity of the media has a direct relation to the dissociation rate, in contrast, it has an inverse relation with the gas production.

Figure S7 in Appendix C displays the input heat from the wellbore to the reservoir during the parametric study of the reservoir's characteristics. Higher thermal conductivity in Zone I induces significantly higher amounts of input heat from the reservoir (Figure S7a). Higher thermal diffusivity (lower heat capacity while the density is constant) induces less heat storage in the media (lower input heat), which in turn, causes more heat transfer to the dissociation front. Thus, increasing the thermal diffusivity and thermal conductivity of Zone I increases the dissociation rate (Figure 26a) and gas production level (Figure S6a). Lower thermal diffusivity of Zone II increases the dissociation rate (Figure 26b) due to greater storage of the transferred heat to this zone from the dissociation interface, which in the end, will be released and consumed for dissociation. Increasing the thermal conductivity of Zone II causes faster heat transfer to this zone from the moving interface, reducing the dissociation rate and gas production. Increasing the thermal diffusivity of Zone II reduces heat storage in this zone, increasing heat consumption for dissociation and raising gas production (Figure S6b). Figure S7b shows that decreasing the thermal diffusivity and increasing the thermal conductivity of Zone II, resulting in more input heat for the same reason stated for input heat increment induced by the same change in thermal conductivity and diffusivity in Zone I (Figure S7a). However, the amount of input heat increment is much lower for the case of Zone II than that of Zone I due to the direct contact of Zone I with the wellbore. Conduction heat transfer and input heat from the wellbore decrease for higher porosities (Figure S7c), ultimately causing a reduction in the dissociation rate (Figures 26c and 26d). Furthermore, higher porosity increases the amount of MH trapped in the pores, eventually increasing the amount of gas produced (Figures S6c and S6d).

Figures 27a and 27b clearly show the direct relation between energy efficiency and thermal diffusivity in Zones I and II, caused by the rise in gas production and drop in input heat induced by increasing the thermal diffusivity. On the other hand, the energy efficiency has an inverse relation with the thermal conductivity of Zones I and II, perhaps due to: i) higher input heat induced by the higher thermal conductivities of Zone I (Figure S7a); and ii) the lower gas production caused by the higher thermal conductivities of Zone II (Figure S6b).

Similar parametric studies by Selim and Sloan (Selim and Sloan 1990) and those of the previous models (3.1 and 3.2) reported similar results for the rate of dissociation (Figure 26). Zhao et al. (Zhao et al. 2015) mathematically showed that increasing the thermal conductivity had a direct positive effect on a dissociation process based on thermal stimulation. They also reported that almost no change occurred in the dissociation by changing the relative permeability of water and gas, due to the negligible impact that the convection heat transfer of water and gas has on the process. Zhao et al. (Zhao et al. 2014) in another numerical work showed that increasing the sediments' thermal conductivity caused a higher gas generation rate at the beginning of dissociation employing depressurization. Both of their works were verified by the experimental data of Masuda's work (MASUDA 1999). Tsimpanogiannis and Lichtner (Tsimpanogiannis and Lichtner 2007), who performed a similar parametric study on MH dissociation upon thermal stimulation, showed that the higher the thermal conductivity of the porous media, the higher the MH dissociation will be. Moridis et al. (Moridis et al. 2004) numerically showed that a higher initial formation temperature, well temperature, and formation thermal conductivity increased the amount of gas production at the Mallik site. They also reported that the dissociation is not affected by the formation permeability and the specific heat of the rock and MH. It is also shown in Figures 26 and S6 (the dissociation rate (β) has a direct relation to the amount of produced gas). It should be noted that some of different working conditions, such as direct hot water circulation into the reservoir, the duration of experiments, and model parameters (i.e., hydrate saturation) may have caused the differences between the results of the experimental works and those of the present work.

Table 7. Range of parameters assumed in the parametric study.

Reservoir parameters	
Porosity, ϕ	0.1 to 0.5
Permeability, k, μm^2	0.1 to 5
Thermal diffusivity of Zone I, α_I, $\mu m^2/s$	1×10^6 to 5×10^6
Thermal conductivity of Zone I, k_I, W/(m.K)	3 to 7
Thermal diffusivity of Zone II, α_{II}, $\mu m^2/s$	4×10^5 to 8×10^5
Thermal conductivity of Zone II, k_{II}, W/(m.K)	1 to 5
Gas viscosity, μ, Pa.s	10^{-4} to 10^{-6}
Wellbore parameters	
Water flow rate, V_f, m^3/s	0.0004 to 0.006
Inlet temperature, T_i, K	330 to 365
Thickness of MH reservoir, h, m	15 to 80
Outer radius of the wellbore, r_7, m	0.114 to 0.174
Only the annulus radius, r_7, m	0.114 to 0.164
Only the inner tube radius, r_2, m	0.013 to 0.053

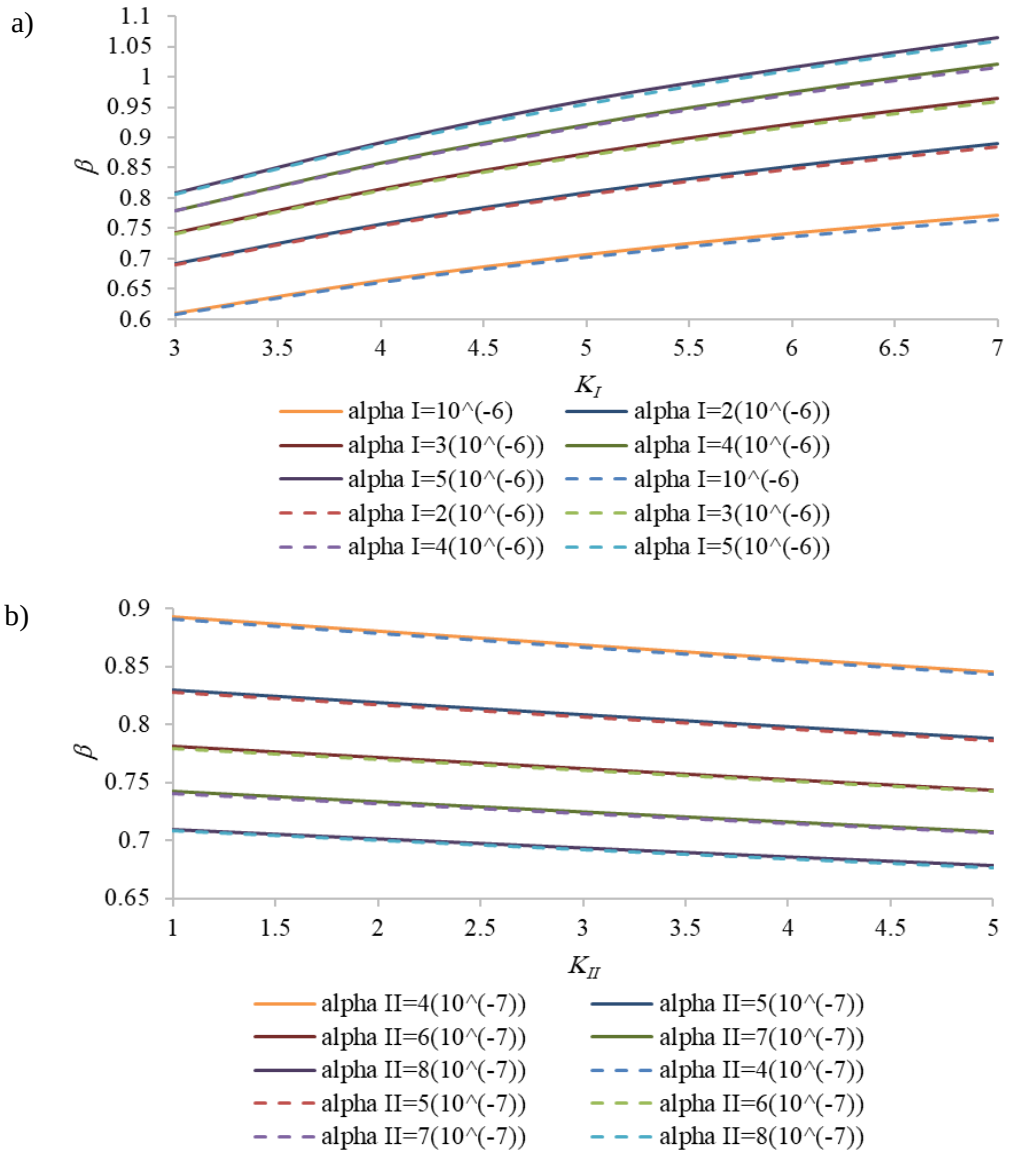

Figure 26. The effect of various parameters on the interface movement after 100 days dissociation considering both operating schemes: a) thermal diffusivity and thermal conductivity of Zone I, b) thermal diffusivity and thermal conductivity of Zone II, c) porosity with various permeabilities, and d) porosity with various gas viscosities.

Solid lines and dashed lines respectively represent the operating schemes of hot water injection into annulus and into the inner tube.

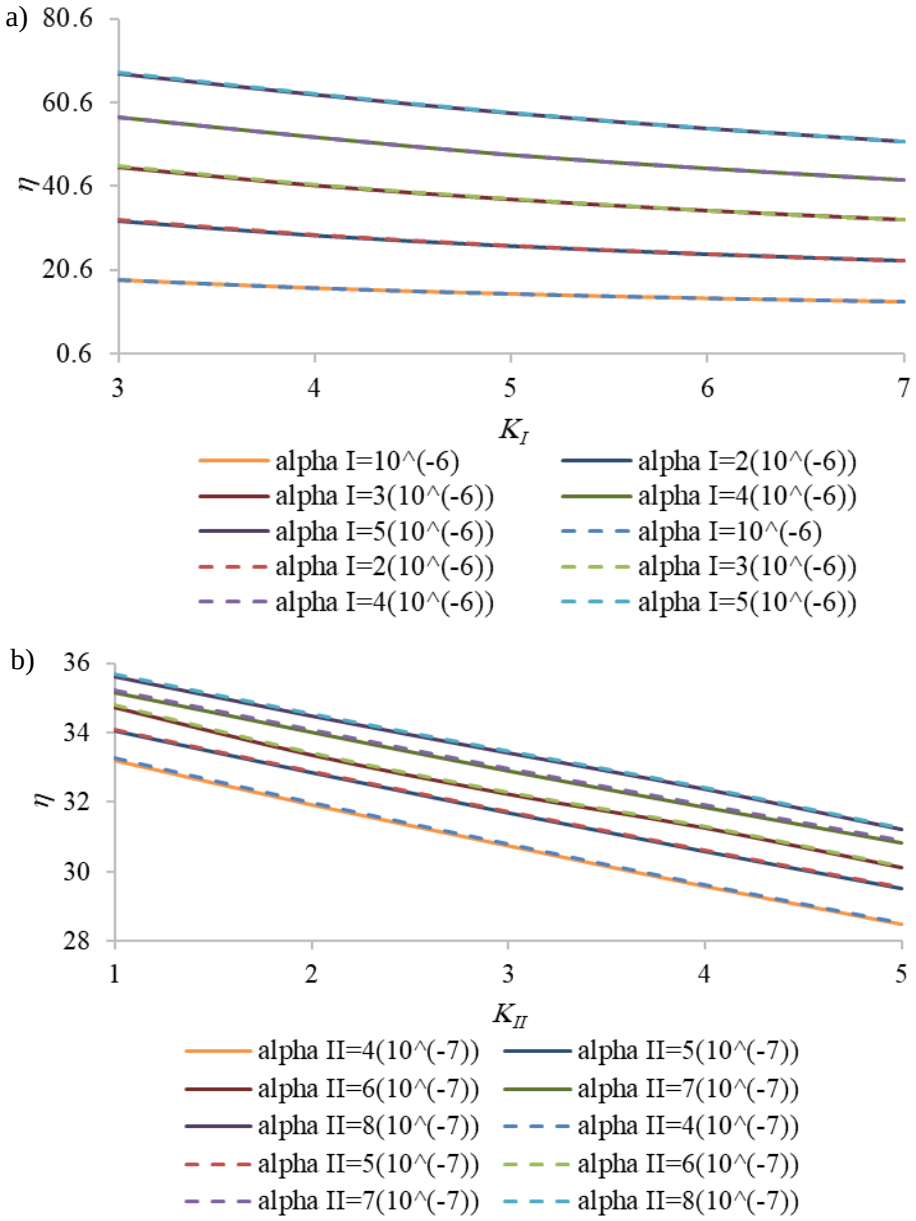
a)
80.6
60.6
40.6
20.6
0.6
η
3
4
5
6
7
K_I
alpha I=10^(-6)
alpha I=2(10^(-6))
alpha I=3(10^(-6))
alpha I=4(10^(-6))
alpha I=5(10^(-6))
alpha I=10^(-6)
alpha I=2(10^(-6))
alpha I=3(10^(-6))
alpha I=4(10^(-6))
alpha I=5(10^(-6))
b)
36
34
32
30
28
η
1
2
3
4
5
K_{II}
alpha II=4(10^(-7))
alpha II=5(10^(-7))
alpha II=6(10^(-7))
alpha II=7(10^(-7))
alpha II=8(10^(-7))
alpha II=4(10^(-7))
alpha II=5(10^(-7))
alpha II=6(10^(-7))
alpha II=7(10^(-7))
alpha II=8(10^(-7))

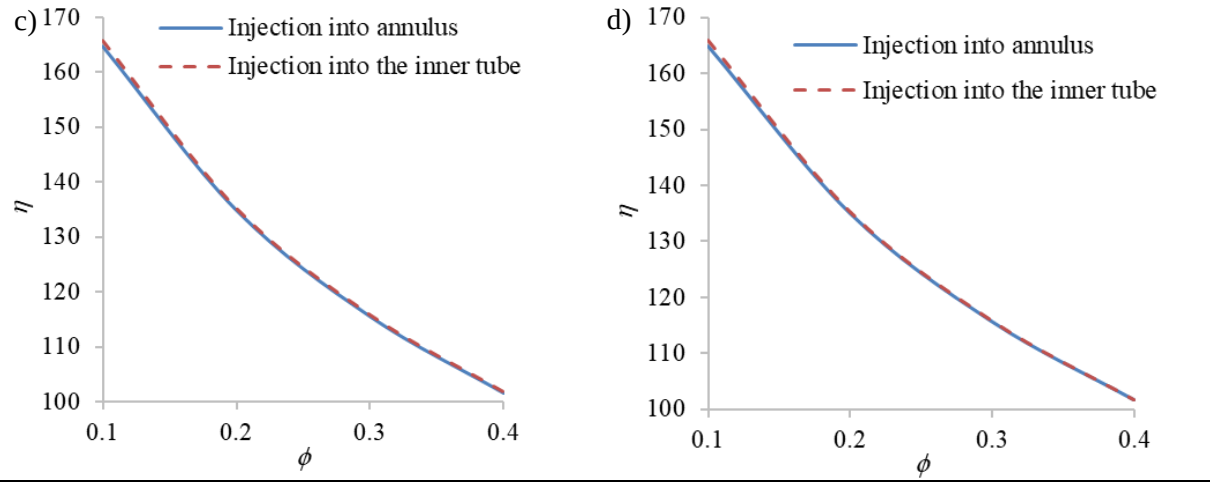

Figure 27. Energy efficiency after 100 days dissociation considering both heat sources and various parameters: a) thermal diffusivity and thermal conductivity of Zone I, b) thermal diffusivity and thermal conductivity of Zone II, c) porosity with various permeabilities, and d) porosity with various gas viscosities.

Solid lines and dashed lines respectively represent the operating schemes of hot water injection into annulus and into the inner tube.

Figures 28, 29, S8, and S9 show the results of the parametric study examining how the wellbore parameters (Table 7) affect dissociation. They highlight the following points: i) a higher wellbore radius (annulus and inner tube with the same amount) increases the dissociation rate (Figure 28a) and gas production level (Figure S8a) because the contact surface enlargement affects the process significantly; ii) the dissociation rate decreases in reservoirs with larger thickness (Figure 28b), whilst, the gas production increases due to the contact surface enlargement (Figure S8b); iii) enlarging the annulus radius, while the inner tube's radius is fixed, has a direct relation on the dissociation rate (Figure 28c) and produced gas (Figure S8c) due to the contact surface enlargement; iv) higher inner tube's radii, while keeping the annulus's radius fixed, has almost no effect on the dissociation process. Raymond et al. (Raymond et al. 2015) through analytical investigations, revealed that increasing the inner tube's radius has little effect on the thermal resistance of coaxial borehole heat exchangers; v) higher inlet temperatures has a direct and noteworthy impact on

both the dissociation rate (Figure 28e) and produced gas (Figure S8e); vi) the dissociation rate and gas production increase initially in response to a transition to higher water flow rates, but they tend to remain almost unchanged after a certain water flow rate.

Increasing the wellbore radius reduces the velocity of the hot water flow inside the wellbore, which in turn reduces the mean temperature inside the wellbore. As a consequence, the input heat from the wellbore to the reservoir drops as well (Figure S9a). The energy efficiency of the process decreases as the wellbore radius increases (Figure 29a) because the ratio of produced gas to the input heat also decreases.

A higher reservoir thickness decreases the input heat (Figure S9b), due to the reduction in the mean temperature inside the wellbore induced by longer wellbores. Holmberg et al. (Holmberg et al. 2016) also reported that the deeper coaxial borehole heat exchangers are not good at heat transfer into the reservoir, but are useful for heat extraction from the reservoir. Raymond et al. (Raymond et al. 2015) analytically proved that longer coaxial boreholes have higher thermal resistances. On the other hand, increasing the reservoir's thickness boosts energy efficiency slightly (Figure 29b) because there is a greater rise in gas production than in input heat. The differences in results between injection into the inner tube and injection into the annulus increases with an increase in the reservoir thickness. Actually, in longer wellbores, hot water injection into the inner tube makes the drop in the flow mean temperature in the annulus become more pronounced because the flow enters the annulus with a lower temperature, while in the other case, the hot water inlet is the annulus, which is in direct contact with the reservoir.

The input heat decreases by increasing only the annulus radius (Figure S9c) due to the same reason stated previously for the effect of the wellbore radius on the input heat. This observation also accords with another analytical study on ground coaxial heat exchangers conducted by Raymond et al. (Raymond et al. 2015). They reported that increasing only the annulus radius reduced the wellbore thermal resistance. In contrast to the higher produced gas induced by bigger annulus radius, the energy efficiency decreases (Figure 29c). Bigger annulus radii while keeping the inner tube's radius fixed will reduce the flow rate in the

annulus significantly, reducing the mean temperature in annulus, and it causes more input heat reduction compared to the case of increasing the radius of both annulus and inner tube together.

The input heat and the energy efficiency increase by increasing the inlet temperature (Figures S9e and 29e). The difference of energy efficiency and input heat results between the two operating schemes tends to get slightly bigger as the inlet temperature increases. Increasing the inlet temperature in the case of hot water injection into annulus directly affects the input heat, but in the other case it causes higher mean temperature in the inner tube, and the associated temperature increase in annulus is not significant.

The input heat increases by increasing the flow rate (Figure S9f), but it converges to almost a fixed value. It can be concluded that the mean temperature inside the wellbore initially increases but increasing the flow rate more than 0.0016 m^3/s almost has no effect on the mean temperature inside the wellbore and the associated input heat to the reservoir. Zanchini et al. (Zanchini et al. 2010), who carried out numerical analysis on the performance of coaxial borehole heat exchangers, showed that the heat transfer capacity of the wellbore would be increased by increasing the flow rate of the wellbore. This is also in line with the results of an analytical work performed by Raymond et al. (Raymond et al. 2015), who showed that the higher flow rates decreased the thermal resistance of coaxial ground heat exchangers. Despite the produced gas increment due to the higher flow rates, energy efficiency of the process reduces (Figure 29f) because the input heat increment is slightly higher than that of the produced gas.

The amount of produced gas and input heat are always higher for the case of injection into annulus than those of the other operating scheme, but, the resulted energy efficiency is always slightly higher for the case of injection into the inner tube except for the cases of studying different flow rates. In fact, by increasing the flow rate in the annulus or in the inner tube, the flow rate would be increased through the wellbore by the same ratio, and it does not depend on hot water inlet.

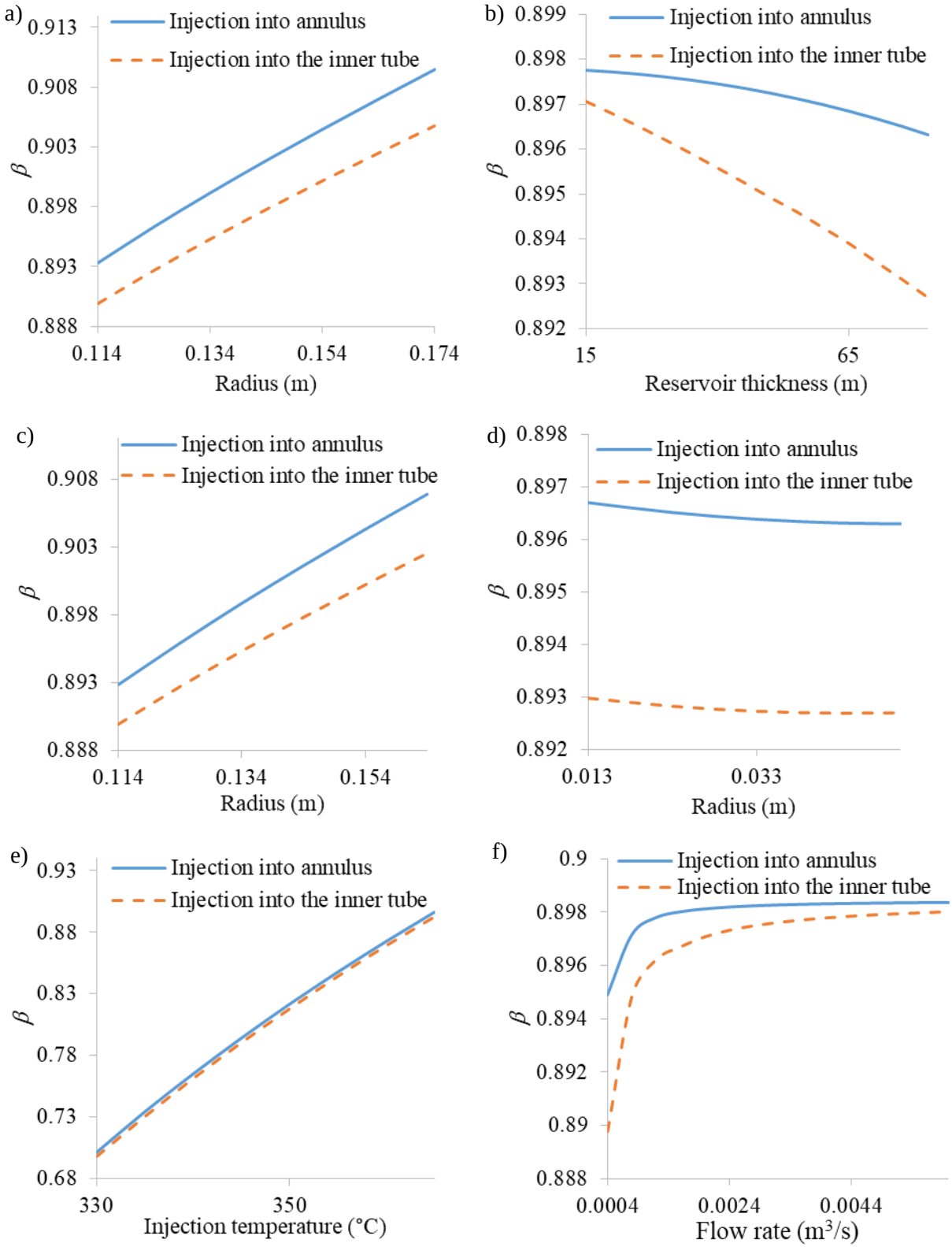
a)
Injection into annulus
Injection into the inner tube
β
0.913
0.908
0.903
0.898
0.893
0.888
0.114
0.134
0.154
0.174
Radius (m)
b)
Injection into annulus
Injection into the inner tube
β
0.899
0.898
0.897
0.896
0.895
0.894
0.893
0.892
15
65
Reservoir thickness (m)
c)
Injection into annulus
Injection into the inner tube
β
0.908
0.903
0.898
0.893
0.888
0.114
0.134
0.154
Radius (m)
d)
Injection into annulus
Injection into the inner tube
β
0.898
0.897
0.896
0.895
0.894
0.893
0.892
0.013
0.033
Radius (m)
e)
Injection into annulus
Injection into the inner tube
β
0.93
0.88
0.83
0.78
0.73
0.68
330
350
Injection temperature (°C)
f)
Injection into annulus
Injection into the inner tube
β
0.9
0.898
0.896
0.894
0.892
0.89
0.888
0.0004
0.0024
0.0044
Flow rate (m³/s)

Figure 28. The effect of various parameters on the interface movement after 100 days dissociation considering both operating schemes: a) the wellbore radius, b) the reservoir thickness, c) the annulus radius, d) the inner tube radius, e) the injection temperature, and f) the flow rate.

Dashed lines and solid lines are respectively representative of the operating schemes of hot water injection into annulus and into the inner tube.

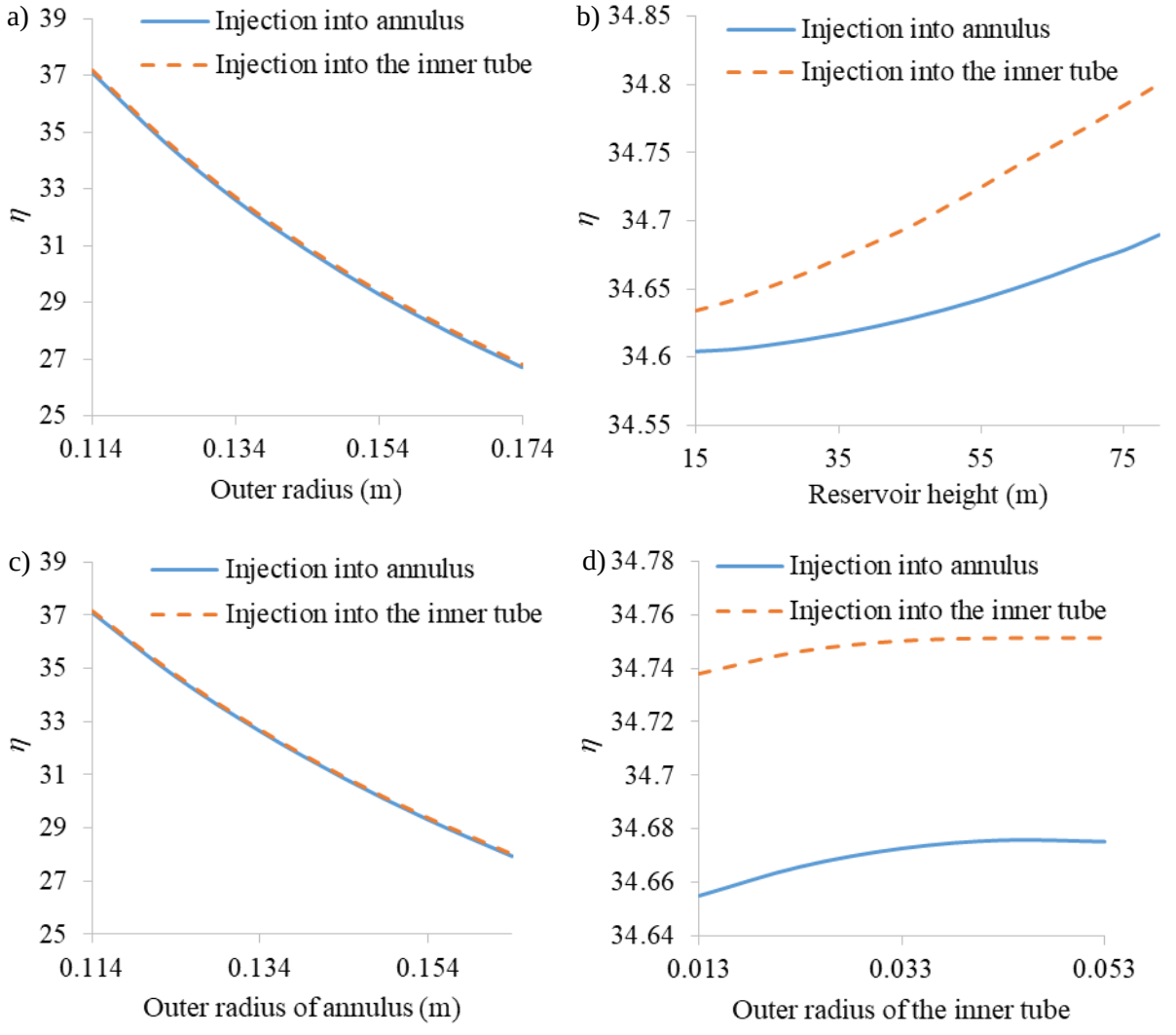

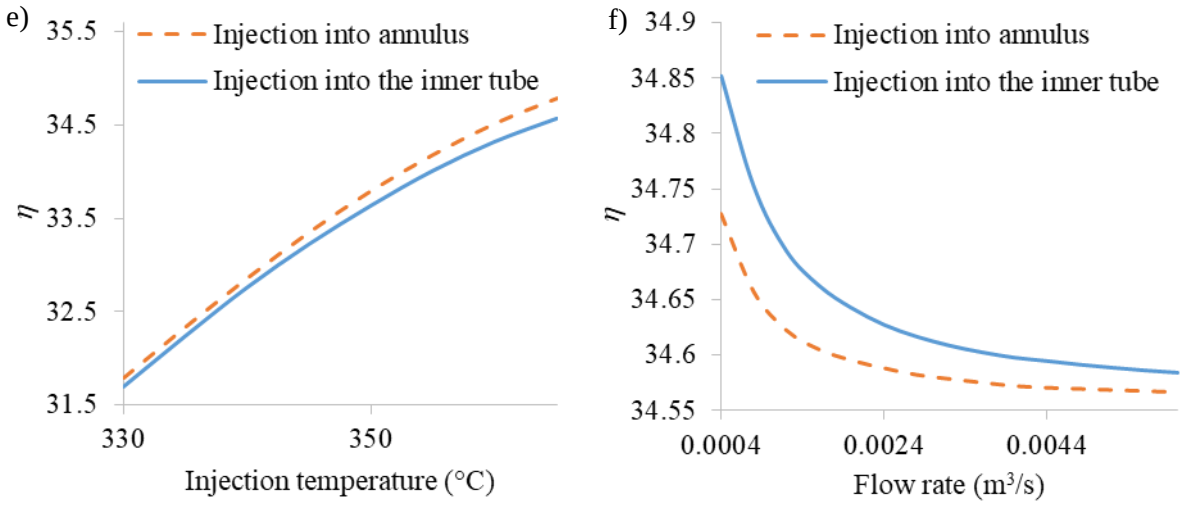

Figure 29. The effect of various parameters on the energy efficiency after 100 days dissociation considering both operating schemes: a) the wellbore radius, b) the reservoir thickness, c) the annulus radius, d) the inner tube radius, e) the injection temperature, f) the flow rate.

Dashed lines and solid lines respectively represent the operating schemes of hot water injection into annulus and into the inner tube.

Chapter 4
Conclusions

Some parts of the thesis are published in two journals: i) the Journal of Petroleum Science and Engineering (Roostaie and Leonenko 2019b) with DOI: 10.1016/j.petrol.2019.106505 and License: CC-BY-NC-ND; and ii) the Energy Journal (Roostaie and Leonenko 2019a) with DOI: 10.1016/j.energy.2019.116815 and License: CC-BY-NC-ND. This thesis has resulted in another paper (Roostaie and Leonenko 2020) (arXiv preprint: arXiv:2001.04900) and submitted to the Energy Conversion and Management Journal.

The present study was designed to determine different aspects of MH dissociation upon thermal stimulation employing wellbore heating. For the first time, Cartesian and radial analytical models respectively in Cartesian and Radial coordinates have been developed. Different types of heat sources are considered, such as line heat-source, wellbore heat-source with external layers (casing, cement, and gravel). This work also investigated how a coaxial wellbore structure as the heat-source affects the dissociation process. The analytical models coupled operational conditions of the heat source and the associated MH dissociation in the reservoir. Heat and mass transfer in both wellbore and reservoir as well as the convection heat transfer in the coaxial wellbore are taken into account. Two operating schemes for coaxial wellbore-heating are considered: i) hot water supply into the inner tube; and ii) hot water supply into the annulus section. The effects of various parameters of wellbore and reservoir as well as different boundary conditions on dissociation are also evaluated. Two main factors are considered to assess the production process performance: i) dissociation rate (β), and ii) energy efficiency of the process (η). Taken together, the most important findings to emerge from the results are as follows:

- The rate of dissociation and process efficiency are dependent on wellbore structure (e.g., thickness, composition), which are design parameters. Well thickness causes a reduction in the dissociation front speed and produced gas amount compared to the cases without considering the well thickness.

- Using a wellbore heat-source causes a reduction in the dissociation rate and the produced gas compared to those of the other case with line heat-source.
- Temperature at the wellbore surface changes over time due to the different temperatures inside the wellbore induced by convection and conduction heat transfer of the hot water flow inside the wellbore. It is also affected by the heat conduction from wellbore to reservoir, which is dependent on the wellbore outer structure.
- As a result, pressure and temperature at the dissociation front are not constant during dissociation.
- The different operating schemes in a coaxial wellbore (i.e., different water inlets) have approximately the same outcome with negligible differences due to the model conditions.
- The dissociation process has direct relation to the temperature of the reservoir and the inlet water, but it has an inverse relation to the wellbore pressure.
- In the cases without considering a coaxial wellbore heat-source, increasing the wellbore temperature and decreasing its pressure simultaneously increase the dissociation rate and produced gas while reduces the energy efficiency. Thus, more information on the initial and boundary conditions including wellbore structure (number of layers, thicknesses, and thermal properties) is essential to establish a greater degree of accuracy on this matter and to improve the energy efficiency of the process.
- In the coaxial wellbore case, increasing the inlet water temperature while decreasing wellbore's pressure increases the dissociation rate and the produced gas. It also increases the energy efficiency despite some of the previous works' reports. This could be due to the inconstant wellbore temperature in the present work. Hence, more information about the heat source operating conditions can help increasing the accuracy on this matter.
- Different wellbore radii, water inlet temperatures and flow rates along with various properties, such as thermal diffusivities, porosities, thermal conductivities, and reservoir thicknesses have significant effects on the process. On the other hand, some

of the reservoir and wellbore parameters, such as inner tube radius, reservoirs permeability, and gas viscosity, have almost no impact on the process. Thus, a thorough investigation on the reservoir properties and applicable heat source characteristics is necessary before performing a field work.

- There is a good agreement between the present results and previous experimental and mathematical studies, validating the assumptions made in the model development.

This project provided an important opportunity to advance the understanding of MH dissociation a basis for future investigations, as the analytical model introduced in this study appears to be the first work to investigate MH dissociation upon wellbore heating in radial coordinates. Prior to this study it was difficult to make predictions about how the wellbore's properties and structure, through which heat transfer to the reservoir occurs, affect the dissociation. For example, the heat input and the resulted energy efficiency can be calculated, which are great assessments for the process. The presented analytical approach takes into account, for the first time: i) both Radial and Cartesian coordinates with wellbore and line heat sources; ii) coupling the heat transfer through the wellbore structure, consisting of multiple layers with different thermal properties, and the associated thermal response in MH dissociation and methane production; iii) coupling the heat transfer process inside the coaxial wellbore and the associated thermal response in the reservoir which governs the dissociation and methane production. This coupling also allows further analysis on wellbore heat-source optimization to have higher energy efficiency in gas production from MH; and iv) a more comprehensive model compared to the previous study (Selim and Sloan 1990). Consequently, the models are more reliable and closer to the real practical conditions.

Bibliography

Ã–zisik, M.N., Özısık, M.N., and Özışık, M.N. 1993. Heat conduction. John Wiley & Sons.

Acuña, J., and Palm, B. A novel coaxial borehole heat exchanger: description and first distributed thermal response test measurements. *In* Proceedings of the World Geothermal Congress. 2010, p. 7.

Ahmadi, G., Ji, C., and Smith, D.H. 2004. Numerical solution for natural gas production from methane hydrate dissociation. Journal of petroleum science and engineering, **41**: 269-285.

Araujo-Lopez, E., Lopez-Echeverry, J.S., and Reif-Acherman, S. 2018. The Antoine equation of state: Rediscovering the potential of an almost forgotten expression for calculating volumetric properties of pure compounds. Chemical Engineering Science, **177**: 89-109.

Azizi, M.A., Brouwer, J., and Dunn-Rankin, D. 2016. Analytical investigation of high temperature 1 kW solid oxide fuel cell system feasibility in methane hydrate recovery and deep ocean power generation. Applied Energy, **179**: 909-928.

Bayles, G., Sawyer, W., Anada, H., Reddy, S., and Malone, R. 1986. A steam cycling model for gas production from a hydrate reservoir. Chemical Engineering Communications, **47**: 225-245.

Beier, R.A., Acuña, J., Mogensen, P., and Palm, B. 2013. Borehole resistance and vertical temperature profiles in coaxial borehole heat exchangers. Applied Energy, **102**: 665-675.

Braud, H.J., Klimkowski, H., and Oliver, J. 1983. Earth-source heat exchanger for heat pumps. Transactions of the ASAE, **26**: 1818-1822.

Burshears, M., O'brien, T., and Malone, R. A multi-phase, multi-dimensional, variable composition simulation of gas production from a conventional gas reservoir in contact with hydrates. *In* SPE Unconventional Gas Technology Symposium. 1986. Society of Petroleum Engineers.

Carslaw, H., and Jaeger, J. 1959. Conduction of heat in solids: Oxford Science Publications. Oxford, England.

Chen, W., and Hartman, R.L. 2018. Methane Hydrate Intrinsic Dissociation Kinetics Measured in a Microfluidic System by Means of in Situ Raman Spectroscopy. Energy & Fuels, **32**: 11761-11771.

Chen, Z.-Y., Li, Q.-P., Yan, Z.-Y., Yan, K.-F., Zeng, Z.-Y., and Li, X.-S. 2010. Phase equilibrium and dissociation enthalpies for cyclopentane+ methane hydrates in NaCl aqueous solutions. Journal of Chemical & Engineering Data, **55**: 4444-4449.

Chen, Z., Feng, J., Li, X., Zhang, Y., Li, B., and Lv, Q. 2014. Preparation of warm brine in situ seafloor based on the hydrate process for marine gas hydrate thermal stimulation. Industrial & engineering chemistry research, **53**: 14142-14157.

Cheng, W.-L., Huang, Y.-H., Lu, D.-T., and Yin, H.-R. 2011. A novel analytical transient heat-conduction time function for heat transfer in steam injection wells considering the wellbore heat capacity. Energy, **36**: 4080-4088.

Claisse, P.A. 2014. Transport properties of concrete: Measurements and applications. Elsevier.

Collett, T. 1999. Detailed evaluation of gas hydrate reservoir properties using JAPEX/JNOC/GSC Mallik 2L-38 gas hydrate research well downhole well-log displays. Bulletin of the Geological Survey of Canada: 295-311.

Collett, T.S. 2001. AAPG Memoir 74, Chapter 7: Natural-Gas Hydrates, Resource of the Twenty-First Century?

Collett, T.S. Assessment of gas hydrate resources on the North Slope, Alaska, 2008. *In* AGU Fall Meeting Abstracts. 2008.

Dalla Santa, G., Peron, F., Galgaro, A., Cultrera, M., Bertermann, D., Mueller, J., and Bernardi, A. 2017. Laboratory measurements of gravel thermal conductivity: An update methodological approach. Energy Procedia, **125**: 671-677.
Dallimore, S. 2002. Overview of gas hydrate research at the Mallik Field in the Mackenzie Delta, Northwest Territories, Canada.
Davie, M.K., and Buffett, B.A. 2001. A numerical model for the formation of gas hydrate below the seafloor. Journal of Geophysical Research: Solid Earth, **106**: 497-514.
Dittus, F., and Boelter, L. 1930. Publications on Engineering, vol. 2, 443 Berkeley. CA: University of California Press.
Englezos, P. 1993. Clathrate hydrates. Industrial & engineering chemistry research, **32**: 1251-1274.
Feng, J.-C., Wang, Y., Li, X.-S., Li, G., and Chen, Z.-Y. 2015. Production behaviors and heat transfer characteristics of methane hydrate dissociation by depressurization in conjunction with warm water stimulation with dual horizontal wells. Energy, **79**: 315-324.
Fischer, D., Mogollón, J.M., Strasser, M., Pape, T., Bohrmann, G., Fekete, N., Spiess, V., and Kasten, S. 2013. Subduction zone earthquake as potential trigger of submarine hydrocarbon seepage. Nature Geoscience, **6**: 647.
Fitzgerald, G.C., and Castaldi, M.J. 2013. Thermal stimulation based methane production from hydrate bearing quartz sediment. Industrial & engineering chemistry research, **52**: 6571-6581.
Fitzgerald, G.C., Castaldi, M.J., and Zhou, Y. 2012. Large scale reactor details and results for the formation and decomposition of methane hydrates via thermal stimulation dissociation. Journal of petroleum science and engineering, **94**: 19-27.
Florez Anaya, A., and Osorio, M.A. A Successful Gravel-Packing Technique in Vertical and Deviated Wells with Enlarged Open Hole in Cased Completions: A Case Study, Rubiales and Quifa Fields. *In* SPE Heavy and Extra Heavy Oil Conference: Latin America. 2014. Society of Petroleum Engineers.
Gnielinski, V. 1975. New equations for heat and mass transfer in the turbulent flow in pipes and channels. NASA STI/recon technical report A, **75**: 8-16.
Gnielinski, V. 2009. Heat transfer coefficients for turbulent flow in concentric annular ducts. Heat transfer engineering, **30**: 431-436.
Hauge, L., Birkedal, K., Ersland, G., and Graue, A. Methane production from natural gas hydrates by CO2 replacement-review of lab experiments and field trial. *In* SPE Bergen One Day Seminar. 2014. Society of Petroleum Engineers.
Hausen, H. 1959. Neue Gleichungen fur die Warmeubertragung bei freier oder erzwungener Stromung. Allg. Wärmetech, **9**: 75-79.
Hellstrom, G. 1992. Ground heat storage: Thermal analyses of duct storage systems. I. Theory.
Hellström, G. Thermal performance of borehold heat exchangers. *In* Stockton International Geothermal Conference: 16/03/1998-17/03/1998. 1998.
Hellström, G. 2002. Borehole heat exchangers: state of the art 2001.
Holder, G.D., and Angert, P.F. Simulation of gas production from a reservoir containing both gas hydrates and free natural gas. *In* SPE annual technical conference and exhibition. 1982. Society of Petroleum Engineers.
Holmberg, H., Acuña, J., Næss, E., and Sønju, O.K. 2016. Thermal evaluation of coaxial deep borehole heat exchangers. Renewable energy, **97**: 65-76.
Hong, H., Pooladi-Darvish, M., and Bishnoi, P. 2003. Analytical modelling of gas production from hydrates in porous media. Journal of Canadian Petroleum Technology, **42**: 45-56.
Ji, C., Ahmadi, G., and Smith, D.H. 2001. Natural gas production from hydrate decomposition by depressurization. Chemical Engineering Science, **56**: 5801-5814.

Judge, A. Natural gas hydrates in Canada. *In* Proceedings of the 4th Canadian Permafrost Conference. 1982. Citeseer, pp. 320-328.

Kamath, V.A., and Godbole, S.P. 1987. Evaluation of hot-brine stimulation technique for gas production from natural gas hydrates. Journal of petroleum technology, **39**: 1,379-371,388.

Khlebnikov, V., Antonov, S., Mishin, A., Bakulin, D., Khamidullina, I., Liang, M., Vinokurov, V., and Gushchin, P. 2016. A new method for the replacement of CH4 with CO2 in natural gas hydrate production. Natural Gas Industry B, **3**: 445-451.

Khosravi Ghasemi, A.H., Mir, M., Ebrahim, M., Nanvakenari, S., and Movagharnejad, K. 2019. Predicting the Coefficients of Antoine Equation Using the Artificial Neural Network. International Journal of Engineering, **32**: 1353-1357.

Konno, Y., Fujii, T., Sato, A., Akamine, K., Naiki, M., Masuda, Y., Yamamoto, K., and Nagao, J. 2017. Key findings of the world's first offshore methane hydrate production test off the coast of Japan: Toward future commercial production. Energy & Fuels, **31**: 2607-2616.

Kowalsky, M.B., and Moridis, G.J. 2007. Comparison of kinetic and equilibrium reaction models in simulating gas hydrate behavior in porous media. Energy conversion and management, **48**: 1850-1863.

Kraussold, H. 1934. Wärmeabgabe von zylindrischen Flüssigkeitschichten bei natürlicher Konvektion. Forschung im Ingenieurwesen, **5**: 186-191.

Kurihara, M., Sato, A., Funatsu, K., Ouchi, H., Yamamoto, K., Numasawa, M., Ebinuma, T., Narita, H., Masuda, Y., and Dallimore, S.R. Analysis of production data for 2007/2008 Mallik gas hydrate production tests in Canada. *In* International Oil and Gas Conference and Exhibition in China. 2010. Society of Petroleum Engineers.

Lamarche, L., Kajl, S., and Beauchamp, B. 2010. A review of methods to evaluate borehole thermal resistances in geothermal heat-pump systems. Geothermics, **39**: 187-200.

Li, B., Liang, Y.-P., Li, X.-S., and Zhou, L. 2016a. A pilot-scale study of gas production from hydrate deposits with two-spot horizontal well system. Applied Energy, **176**: 12-21.

Li, B., Liu, S.-D., Liang, Y.-P., and Liu, H. 2018. The use of electrical heating for the enhancement of gas recovery from methane hydrate in porous media. Applied Energy, **227**: 694-702.

Li, G., Moridis, G.J., Zhang, K., and Li, X.-S. 2010. Evaluation of gas production potential from marine gas hydrate deposits in Shenhu area of South China Sea. Energy & Fuels, **24**: 6018-6033.

Li, G., Li, X.-S., Li, B., and Wang, Y. 2014. Methane hydrate dissociation using inverted five-spot water flooding method in cubic hydrate simulator. Energy, **64**: 298-306.

Li, M., Fan, S., Su, Y., Ezekiel, J., Lu, M., and Zhang, L. 2015. Mathematical models of the heat-water dissociation of natural gas hydrates considering a moving Stefan boundary. Energy, **90**: 202-207.

Li, S., Zheng, R., Xu, X., and Hou, J. 2016b. Natural gas hydrate dissociation by hot brine injection. Petroleum Science and Technology, **34**: 422-428.

Li, X.-S., Wang, Y., Li, G., and Zhang, Y. 2011a. Experimental investigations into gas production behaviors from methane hydrate with different methods in a cubic hydrate simulator. Energy & Fuels, **26**: 1124-1134.

Li, X.-S., Li, B., Li, G., and Yang, B. 2012a. Numerical simulation of gas production potential from permafrost hydrate deposits by huff and puff method in a single horizontal well in Qilian Mountain, Qinghai province. Energy, **40**: 59-75.

Li, X.-S., Wang, Y., Li, G., Zhang, Y., and Chen, Z.-Y. 2011b. Experimental investigation into methane hydrate decomposition during three-dimensional thermal huff and puff. Energy & Fuels, **25**: 1650-1658.

Li, X.-S., Xu, C.-G., Zhang, Y., Ruan, X.-K., Li, G., and Wang, Y. 2016c. Investigation into gas production from natural gas hydrate: A review. Applied Energy, **172**: 286-322.
Li, X.-S., Yang, B., Zhang, Y., Li, G., Duan, L.-P., Wang, Y., Chen, Z.-Y., Huang, N.-S., and Wu, H.-J. 2012b. Experimental investigation into gas production from methane hydrate in sediment by depressurization in a novel pilot-scale hydrate simulator. Applied Energy, **93**: 722-732.
Liang, H., Song, Y., and Chen, Y. 2010. Numerical simulation for laboratory-scale methane hydrate dissociation by depressurization. Energy conversion and management, **51**: 1883-1890.
Majorowicz, J., and Osadetz, K. 2001. Gas hydrate distribution and volume in Canada. AAPG bulletin, **85**: 1211-1230.
Makogon, I.U.r.F. 1981. Hydrates of natural gas. PennWell Books Tulsa, OK.
Makogon, Y., and Omelchenko, R. 2013. Commercial gas production from Messoyakha deposit in hydrate conditions. Journal of Natural Gas Science and Engineering, **11**: 1-6.
Makogon, Y.F. 1997. Hydrates of hydrocarbons: Pennwell Pub. Comp. Tulsa, Oklahoma.
Mardani, M., Azimi, A., Javanmardi, J., and Mohammadi, A.H. 2018. Effect of EMIM-BF4 Ionic Liquid on Dissociation Temperature of Methane Hydrate in the Presence of PVCap: Experimental and Modeling Studies. Energy & Fuels, **33**: 50-57.
Maruyama, S., Deguchi, K., Chisaki, M., Okajima, J., Komiya, A., and Shirakashi, R. 2012. Proposal for a low CO2 emission power generation system utilizing oceanic methane hydrate. Energy, **47**: 340-347.
Masuda, Y. Numerical calculation of gas production performance from reservoirs containing natural gas hydrates. *In* Annual Technical Conference, Soc. of Petrol. Eng., San Antonio, Tex., Oct. 1997. 1997.
MASUDA, Y. Modeling and experimental studies on dissociation of methane gas hydrates in Berea sandstone cores. *In* Proceedings of the third International Gas Hydrate Conference. 1999.
Max, M., and Dillon, W.P. 1998. Oceanic methane hydrate: the character of the Blake Ridge hydrate stability zone, and the potential for methane extraction. Journal of Petroleum Geology, **21**: 343-358.
McGuire, P.L. Recovery of gas from hydrate deposits using conventional technology. *In* SPE Unconventional Gas Recovery Symposium. 1982. Society of Petroleum Engineers.
Mei, V., and Fischer, S. 1983. Vertical concentric tube ground-coupled heat exchangers. ASHRAE transactions, **89**: 391-406.
Moridis, G., Silpngarmlert, S., Reagan, M., Collett, T., and Zhang, K. 2011. Gas production from a cold, stratigraphically-bounded gas hydrate deposit at the Mount Elbert Gas Hydrate Stratigraphic Test Well, Alaska North Slope: Implications of uncertainties. Marine and petroleum geology, **28**: 517-534.
Moridis, G.J. Numerical studies of gas production from methane hydrates. *In* SPE Gas Technology Symposium. 2002. Society of Petroleum Engineers.
Moridis, G.J., and Reagan, M.T. 2007. Strategies for gas production from oceanic class 3 hydrate accumulations.
Moridis, G.J., and Sloan, E.D. 2007. Gas production potential of disperse low-saturation hydrate accumulations in oceanic sediments. Energy conversion and management, **48**: 1834-1849.
Moridis, G.J., Collett, T.S., Dallimore, S.R., Satoh, T., Hancock, S., and Weatherill, B. 2004. Numerical studies of gas production from several CH4 hydrate zones at the Mallik site, Mackenzie Delta, Canada. Journal of petroleum science and engineering, **43**: 219-238.
Morita, K., Bollmeier, W.S., and Mizogami, H. 1992. Analysis of the results from the downhole coaxial heat exchanger (DCHE) experiment in Hawaii.

Nishikawa, N., Morishita, M., Uchiyama, M., Yamaguchi, F., Ohtsubo, K., Kimuro, H., and Hiraoka, R. 1992. CO2 clathrate formation and its properties in the simulated deep ocean. Energy conversion and management, **33**: 651-657.

Notter, R., and Sleicher, C. 1972. A solution to the turbulent Graetz problem—III Fully developed and entry region heat transfer rates. Chemical Engineering Science, **27**: 2073-2093.

Ntuli, M., Dirker, J., and Meyer, J. Heat transfer and pressure drop coefficients for turbulent flow in concentric annular ducts. *In* 19th International Congress of Chemical and Process Engineering. 2010.

Petukhov, B. 1970. Heat transfer and friction in turbulent pipe flow with variable physical properties. *In* Advances in heat transfer. Elsevier. pp. 503-564.

Petukhov, B., and Roizen, L. Heat Exchange During Gas Flow in Pipes with an Annular Cross Section. *In* Heat and Mass Transfer. 1967. Vol. 1842, p. 56.

Phirani, J., Mohanty, K.K., and Hirasaki, G.J. 2009. Warm water flooding of unconfined gas hydrate reservoirs. Energy & Fuels, **23**: 4507-4514.

Pucknell, J., and Mason, J. Predicting the Pressure Drop in a Cased-Hole Gravel Pack Completion. *In* European Petroleum Conference. 1992. Society of Petroleum Engineers.

Rapp, B.E. 2016. Microfluidics: Modeling, Mechanics and Mathematics. William Andrew.

Raymond, J., Mercier, S., and Nguyen, L. 2015. Designing coaxial ground heat exchangers with a thermally enhanced outer pipe. Geothermal Energy, **3**: 7.

Reeburgh, W.S. 2007. Oceanic Methane Biogeochemistry. Chemical Reviews, **107**: 486-513. doi:10.1021/cr050362v.

Remund, C.P. 1999. Borehole thermal resistance: laboratory and field studies. ASHRAE transactions, **105**: 439.

Rohsenow, W.M., Hartnett, J.P., and Ganic, E.N. 1985. Handbook of heat transfer fundamentals. New York, McGraw-Hill Book Co., 1985, 1440 p. No individual items are abstracted in this volume.

Roostaie, M., and Leonenko, Y. 2019a. Gas production from methane hydrates upon thermal stimulation; an analytical study employing radial coordinates. Energy: doi.org/10.1016/j.energy.2019.116815.

Roostaie, M., and Leonenko, Y. 2019b. Analytical modeling of methane hydrate dissociation under thermal stimulation. Journal of petroleum science and engineering: doi.org/10.1016/j.petrol.2019.106505

Roostaie, M., and Leonenko, Y. 2020. Analytical investigation of gas production from methane hydrates and the associated heat and mass transfer upon thermal stimulation employing a coaxial wellbore. arXiv preprint arXiv:2001.04900.

Ross, M.J., and Toczylkin, L.S. 1992. Hydrate dissociation pressures for methane or ethane in the presence of aqueous solutions of triethylene glycol. Journal of Chemical and Engineering Data, **37**: 488-491.

Ruppel, C.D., and Kessler, J.D. 2017. The interaction of climate change and methane hydrates. Reviews of Geophysics, **55**: 126-168.

Saji, A., Yoshida, H., Sakai, M., Tanii, T., Kamata, T., and Kitamura, H. 1992. Fixation of carbon dioxide by clathrate-hydrate. Energy conversion and management, **33**: 643-649.

Schoderbek, D., Farrell, H., Hester, K., Howard, J., Raterman, K., Silpngarmlert, S., Martin, K., Smith, B., and Klein, P. 2013. Oil & Natural Gas Technology: ConocoPhillips Gas Hydrate Production Test: Final Technical Report. United States Department of Energy, National Energy Technology Laboratory, DE-NT0006553-Final-Technical-Report.

Selim, M., and Sloan, E. 1990. Hydrate dissociation in sediment. SPE Reservoir Engineering, **5**: 245-251.

Sieder, E.N., and Tate, G.E. 1936. Heat transfer and pressure drop of liquids in tubes. Industrial & Engineering Chemistry, **28**: 1429-1435.
Song, Y., Cheng, C., Zhao, J., Zhu, Z., Liu, W., Yang, M., and Xue, K. 2015. Evaluation of gas production from methane hydrates using depressurization, thermal stimulation and combined methods. Applied Energy, **145**: 265-277.
Sparrow, E.M., Patankar, S., and Ramadhyani, S. 1977. Analysis of melting in the presence of natural convection in the melt region.
STOCKER, T., QIN, D., and PLATTNER, G. 2013. Intergovernmental panel on climate change IPCC (2013). Climate Change 2013: the Scientific Basis [R]. Cambridge University Press.
Sun, F., Yao, Y., Li, X., Li, G., and Sun, Z. 2018. A numerical model for predicting distributions of pressure and temperature of superheated steam in multi-point injection horizontal wells. International Journal of Heat and Mass Transfer, **121**: 282-289.
Sun, F., Yao, Y., Li, X., Tian, J., Zhu, G., and Chen, Z. 2017. The flow and heat transfer characteristics of superheated steam in concentric dual-tubing wells. International Journal of Heat and Mass Transfer, **115**: 1099-1108.
Sun, Y., Li, B., Guo, W., Lü, X., Zhang, Y., Li, K., Wang, P., Jin, G., Jia, R., and Qu, L. 2014. Comparative analysis of the production trial and numerical simulations of gas production from multilayer hydrate deposits in the Qilian Mountain permafrost. Journal of Natural Gas Science and Engineering, **21**: 456-466.
Sung, W., Lee, H., Lee, H., and Lee, C. 2002. Numerical study for production performances of a methane hydrate reservoir stimulated by inhibitor injection. Energy Sources, **24**: 499-512.
Tang, L.-G., Li, X.-S., Feng, Z.-P., Li, G., and Fan, S.-S. 2007. Control mechanisms for gas hydrate production by depressurization in different scale hydrate reservoirs. Energy & Fuels, **21**: 227-233.
Tang, L.G., Xiao, R., Huang, C., Feng, Z., and Fan, S.S. 2005. Experimental investigation of production behavior of gas hydrate under thermal stimulation in unconsolidated sediment. Energy & Fuels, **19**: 2402-2407.
Thomson, G.W. 1946. The Antoine equation for vapor-pressure data. Chemical Reviews, **38**: 1-39.
TREHU, A.M. 2006. Gas hydrates in marine sediments: Lessons from scientific ocean drilling. Oceanography, **19**: 124-142.
Tsimpanogiannis, I.N., and Lichtner, P.C. 2007. Parametric study of methane hydrate dissociation in oceanic sediments driven by thermal stimulation. Journal of petroleum science and engineering, **56**: 165-175.
Tsypkin, G. 2001. Regimes of dissociation of gas hydrates coexisting with a gas in natural strata. Journal of engineering physics and thermophysics, **74**: 1083-1089.
Tsypkin, G.G. 2000. Mathematical models of gas hydrates dissociation in porous media. Annals of the New York academy of sciences, **912**: 428-436.
Wan, Q.-C., Si, H., Li, B., and Li, G. 2018. Heat transfer analysis of methane hydrate dissociation by depressurization and thermal stimulation. International Journal of Heat and Mass Transfer, **127**: 206-217.
Wang, H., Li, X., Sepehrnoori, K., Zheng, Y., and Yan, W. 2019a. Calculation of the wellbore temperature and pressure distribution during supercritical CO2 fracturing flowback process. International Journal of Heat and Mass Transfer, **139**: 10-16.
Wang, L., Liu, H., Pang, Z., and Lv, X. 2016a. Overall heat transfer coefficient with considering thermal contact resistance in thermal recovery wells. International Journal of Heat and Mass Transfer, **103**: 486-500.
Wang, P., Zhu, Y., Lu, Z., Huang, X., Pang, S., and Zhang, S. 2014a. Gas hydrate stability zone migration occurred in the Qilian Mountain permafrost, Qinghai, Northwest China: Evidences

from pyrite morphology and pyrite sulfur isotope. Cold regions science and technology, **98**: 8-17.
Wang, X., Dong, B., Wang, F., Li, W., and Song, Y. 2019b. Pore-scale investigations on the effects of ice formation/melting on methane hydrate dissociation using depressurization. International Journal of Heat and Mass Transfer, **131**: 737-749.
Wang, Y., Feng, J.-C., Li, X.-S., and Zhang, Y. 2016b. Experimental and modeling analyses of scaling criteria for methane hydrate dissociation in sediment by depressurization. Applied Energy, **181**: 299-309.
Wang, Y., Li, X.-S., Li, G., Huang, N.-S., and Feng, J.-C. 2014b. Experimental study on the hydrate dissociation in porous media by five-spot thermal huff and puff method. Fuel, **117**: 688-696.
Wang, Y., Feng, J.-C., Li, X.-S., Zhang, Y., and Li, G. 2015. Analytic modeling and large-scale experimental study of mass and heat transfer during hydrate dissociation in sediment with different dissociation methods. Energy, **90**: 1931-1948.
Wang, Y., Feng, J.-C., Li, X.-S., Zhang, Y., and Li, G. 2016c. Large scale experimental evaluation to methane hydrate dissociation below quadruple point in sandy sediment. Applied Energy, **162**: 372-381.
Wang, Y., Feng, J.-C., Li, X.-S., Zhang, Y., and Chen, Z.-Y. 2018. Fluid flow mechanisms and heat transfer characteristics of gas recovery from gas-saturated and water-saturated hydrate reservoirs. International Journal of Heat and Mass Transfer, **118**: 1115-1127.
Wang, Y., Li, X.-S., Li, G., Zhang, Y., Li, B., and Chen, Z.-Y. 2013. Experimental investigation into methane hydrate production during three-dimensional thermal stimulation with five-spot well system. Applied Energy, **110**: 90-97.
Wärmeatlas, V. 1988. Berechnungsblätter für den Wärmeübergang. VDI-Verlag, Düsseldorf.
Weinbaum, S., and Wheeler Jr, H. 1949. Heat Transfer in Sweat-Cooled Porous Metals. Journal of Applied Physics, **20**: 113-122.
Xiong, W., Bahonar, M., and Chen, Z. Development of a thermal wellbore simulator with focus on improving heat loss calculations for SAGD steam injection. *In* SPE Canada Heavy Oil Technical Conference. 2015. Society of Petroleum Engineers.
Xu, E., Soga, K., Zhou, M., Uchida, S., and Yamamoto, K. Numerical analysis of wellbore behaviour during methane gas recovery from hydrate bearing sediments. *In* Offshore Technology Conference. 2014. Offshore Technology Conference.
Yamamoto, K. 2015. Overview and introduction: Pressure core-sampling and analyses in the 2012–2013 MH21 offshore test of gas production from methane hydrates in the eastern Nankai Trough. Marine and petroleum geology, **66**: 296-309.
Yavuzturk, C., and Chiasson, A.D. 2002. Performance analysis of U-tube, concentric tube, and standing column well ground heat exchangers using a system simulation approach. ASHRAE transactions, **108**: 925.
Yousif, M., Li, P., Selim, M., and Sloan, E. 1990. Depressurization of natural gas hydrates in Berea sandstone cores. Journal of inclusion phenomena and molecular recognition in chemistry, **8**: 71-88.
Yousif, M., Abass, H., Selim, M., and Sloan, E. 1991. Experimental and theoretical investigation of methane-gas-hydrate dissociation in porous media. SPE Reservoir Engineering, **6**: 69-76.
Yousif, M.H. Effect of under-inhibition with methanol and ethylene glycol on the hydrate control process. *In* Offshore Technology Conference. 1996. Offshore Technology Conference.
Yuan, Q., Sun, C.-Y., Yang, X., Ma, P.-C., Ma, Z.-W., Liu, B., Ma, Q.-L., Yang, L.-Y., and Chen, G.-J. 2012. Recovery of methane from hydrate reservoir with gaseous carbon dioxide using a three-dimensional middle-size reactor. Energy, **40**: 47-58.

Zanchini, E., Lazzari, S., and Priarone, A. 2010. Improving the thermal performance of coaxial borehole heat exchangers. Energy, **35**: 657-666.

Zhao, J., Liu, D., Yang, M., and Song, Y. 2014. Analysis of heat transfer effects on gas production from methane hydrate by depressurization. International Journal of Heat and Mass Transfer, **77**: 529-541.

Zhao, J., Wang, J., Liu, W., and Song, Y. 2015. Analysis of heat transfer effects on gas production from methane hydrate by thermal stimulation. International Journal of Heat and Mass Transfer, **87**: 145-150.

Zhao, J., Fan, Z., Dong, H., Yang, Z., and Song, Y. 2016. Influence of reservoir permeability on methane hydrate dissociation by depressurization. International Journal of Heat and Mass Transfer, **103**: 265-276.

Zhao, J., Cheng, C., Song, Y., Liu, W., Liu, Y., Xue, K., Zhu, Z., Yang, Z., Wang, D., and Yang, M. 2012. Heat transfer analysis of methane hydrate sediment dissociation in a closed reactor by a thermal method. Energies, **5**: 1292-1308.

Appendix A

In the following, the transformation of the fundamental equations, initial and boundary conditions in terms of λ is provided.

Equation 4: $\frac{d^2T_{II}}{d\lambda^2} + 2\lambda\frac{dT_{II}}{d\lambda} = 0,\ \beta < \lambda < \infty$ (S1)

Equation 6: $\frac{-k_I A_w}{\sqrt{4\alpha_{II}t}}\frac{dT_I}{d\lambda} = \frac{(T_i - T_I)}{R_w},\ \lambda = \lambda_{os}$ (S2)

Equation 8: $P_s = \exp(A - B/T_s),\ \lambda = \beta$ (S3)

Equation 10: $k_{II}\frac{dT_{II}}{d\lambda} - k_I\frac{dT_I}{d\lambda} = 2\phi\rho_H\alpha_{II}Q_{Hd}\beta,\ \lambda = \beta$ (S4)

Equation 14: $\frac{d}{d\lambda}\left(\frac{P}{T_I}\frac{dP}{d\lambda}\right) + \frac{2\phi\alpha_{II}\mu\lambda}{k}\frac{d}{d\lambda}\left(\frac{P}{T_I}\right) = 0,\ \lambda_{os} < \lambda < \beta$ (S5)

Equation 16: $\frac{d^2T_I}{d\lambda^2} + \frac{2\alpha_{II}\lambda}{\alpha_I}\frac{dT_I}{d\lambda} + \frac{C_{pg}km}{2k_I\mu R}\frac{d^2P^2}{d\lambda^2} = 0,\ \lambda_{os} < \lambda < \beta$ (S6)

Equation 17: $\frac{P}{T_I}\frac{dP}{d\lambda} = \frac{2F_{gH}\phi\rho_H\alpha_{II}\mu R\beta}{km},\ \lambda = \beta$ (S7)

And, from equation 13: $T_{II} = T_0,\ \lambda \to \infty$ (S8)

Furthermore, in a previous work reported by Selim et al. (Selim and Sloan 1990), it is stated that due to the very small ratio of $\frac{\rho_g}{\rho_H}$, the rate of hydrate dissociation (dS/dt) is too slow that the transient term in the continuity equation could be neglected (second term in equation S5). In the equation 21, A, B, and C constants are defined using equations S5 and 12 as follows:

$$A = \frac{(T_s - T_i)F}{Ferf\ (a\beta + b) - Ferf\ (b) - D - E} \quad \text{(S9)}$$

$$B = \frac{-A(D+E)}{F} + T_i \quad \text{(S10)}$$

$$C = \frac{T_s - T_e}{erfc(\beta)} \quad \text{(S11)}$$

, where *a*, *b*, *D*, *E*, and *F* are as follows:

$$a = \left(\frac{\alpha_{II}}{\alpha_I} \right)^{1/2} \tag{S12}$$

$$b = \frac{C_{pg} F_{gH} \phi \rho_H \alpha_{II} \beta}{a k_I} \tag{S13}$$

$$D = \frac{-k_I \, 2a \exp(-(a\lambda_{os} + b)^2)}{e\sqrt{\pi}} \tag{S14}$$

$$E = -F(-erf\ (a\lambda_{os} + b) + erf\ (b)) \tag{S15}$$

$$F = \frac{1}{R_w} \tag{S16}$$

In the equation 22, pressure distribution in zone I, the $J(\beta)$, $K(\beta)$, and $L_1(\lambda)$ are defined as follows:

$$J(\beta) = \frac{4F_{gH} \phi \rho_H \alpha_{II} \mu R \beta}{km} \tag{S17}$$

$$K(\beta) = B - A erf\ (b) \tag{S18}$$

$$L_1(\lambda) = \lambda erf\ (a\lambda + b) + \frac{b erf\ (a\lambda + b)}{a} + \frac{\exp(-(a\lambda + b)^2)}{a\sqrt{\pi}} \tag{S19}$$

Now, equation S4 by insertion of the resulted T_I and T_{II} formulas (equation 21 and considering equation 11 becomes:

$$\frac{a k_I (T_i - T_s)}{k_{II} (T_s - T_0)} \underbrace{\left(\frac{F \exp(-(a\beta + b)^2)}{Ferf\ (a\beta + b) - Ferf\ (b) - D - E} \right)}_{G(\beta)} + \underbrace{\left(\frac{-\exp(-\beta^2)}{erfc(\beta)} \right)}_{H(\beta)} = \underbrace{\sqrt{\pi} \phi \rho_H \alpha_{II} \beta}_{I(\beta)} \frac{(c + dT_s)}{k_{II} (T_s - T_0)} \tag{S20}$$

So, temperature at the interface is calculated as follows:

$$T_s = \frac{k_{II} T_0 H(\beta) - a k_I T_i G(\beta) + c I(\beta)}{-a k_I G(\beta) - d I(\beta) + k_{II} H(\beta)} \tag{S21}$$

From the equation 22, the pressure at the dissociation interface (P_s) would be:

$$P_s = \left(P_0^2 + J(\beta) K(\beta) (\beta - \lambda_{os}) + A J(\beta) (L_1(\beta) - L_1(\lambda_{os})) \right)^{1/2} \tag{S22}$$

Now, by implementing the equation 8 (Antoine equation), which is transformed to the following form (equation S23), the exact solution of temperature and pressure distributions will be achieved.

$$\frac{B_a}{A_a - \ln(P_s)} - T_s = 0 \tag{S23}$$

Actually, β is the root of the equation S23 as all the parameters are known at each time except β. By finding β, the temperature and pressure distribution will also be calculated at each time.

The transformed form of the heat flux (equation 24) from the well due to the transformation term of equation 18 is as follows:

$$u_f = \frac{-k_I}{\sqrt{4\alpha_{II} t}} \frac{dT_I}{d\lambda}, \ \lambda = \lambda_{os} \tag{S24}$$

By inserting T_I from equation 21, equation S24 becomes:

$$u_f = \frac{-2ak_I A \exp(-(a\lambda_{os} + b)^2)}{\sqrt{4\alpha_{II} \pi t}} \tag{S25}$$

In order to calculate the total volume of gas produced at STP conditions, the molar quantity of produced gas at each time should be calculated first as follows:

$$V_f = \phi(S_t - S_{t-1}) \tag{S26}$$

$$n_f = F_{gH} \rho_H V_f / m \tag{S27}$$

Equation S26 shows the volume of dissociated hydrate at each time step (*t-1, t*), and equation S27 represents the moles of produced gas at each time step (*t-1, t*). By summing the moles of produced gas at each time step, total moles of produced gas up to time t will be achieved as presented in equation S28.

$$n_{ft} = \sum_{t=0}^{t} n_f \tag{S28}$$

Finally, the total volume of produced gas at STP conditions up to time t will be calculated by using equations S28 and 5 as presented by equation 25.

Appendix B

In the following, the transformation of the fundamental equations, initial and boundary conditions in terms of λ is provided (some of the equations are the same as those of the previous part, Appendix A,).

Equation 31: $\frac{d^2T_{II}}{d\lambda^2}+\left(\frac{2\lambda^2+1}{\lambda}\right)\frac{dT_{II}}{d\lambda}=0,\ \beta<\lambda<\infty$ (S29)

Equation 34: $\frac{-k_I A_w}{\sqrt{4\alpha_{II}t}}\frac{dT_I}{d\lambda}=\frac{(T_i-T_I)}{R_w},\ \lambda=\lambda_{os}$ (S30)

Equation 37: $k_{II}\frac{dT_{II}}{d\lambda}-k_I\frac{dT_I}{d\lambda}=2\phi\rho_H\alpha_{II}Q_{Hd}\beta,\ \lambda=\beta$ (S31)

Equation 40: $T_{II}=T_0,\ \lambda\to\infty$ (S32)

Equation 41: $\frac{d}{d\lambda}\left(\frac{P}{T_I}\frac{dP}{d\lambda}\right)+\frac{2\phi\alpha_{II}\mu\lambda}{k}\frac{d}{d\lambda}\left(\frac{P}{T_I}\right)=0,\ \lambda_{os}<\lambda<\beta$ (S33)

Equation 42: $\frac{d^2T_I}{d\lambda^2}+\left(\frac{2\alpha_{II}\lambda}{\alpha_I}+\frac{1}{\lambda}\right)\frac{dT_I}{d\lambda}+\frac{C_{pg}km}{2k_I\mu R}\frac{d^2P^2}{d\lambda^2}=0,\ \lambda_{os}<\lambda<\beta$ (S34)

And, from equation 43: $\frac{P}{T_I}\frac{dP}{d\lambda}=\frac{2F_{gH}\phi\rho_H\alpha_{II}\mu R\beta}{km},\ \lambda=\beta$ (S35)

Due to the very small ratio of $\frac{\rho_g}{\rho_H}$, the rate of hydrate dissociation (dS/dt) is assumed to be very slow that the transient term in the continuity equation could be neglected (second term in equation S5). (Selim and Sloan 1990).

In the equations 47 and 48, A_1, A_2, B_1, B_2, and C constants are defined using equations S30 and 38 as follows:

$$A_1=\frac{(T_s-T_i)}{Ei(-(a\beta+b)^2)-Ei(-b^2)}$$ (S36)

$$A_2=\frac{(T_s-T_i)F}{-FEi(-(a\beta+b)^2)+FEi(-b^2)+D_1+E_1}$$ (S37)

$$B_1 = B_2 = \frac{T_s - T_e}{Ei(-\beta^2)} \tag{S38}$$

$$C = \frac{A_2(D_1 + E_1)}{F} + T_i \tag{S39}$$

where D_1, and E_1 are as follows:

$$D_1 = \frac{-R_{out} k_I \, 2a \exp(-(a\lambda_{os} + b)^2)}{e\sqrt{\pi}} \tag{S40}$$

$$E_1 = R_w \left(-Ei\left(-(a\lambda_{os} + b)^2\right) + Ei\left(-b^2\right)\right) \tag{S41}$$

The $L_2(\beta)$, $M(\beta)$, $N(\lambda)$, and $K_1(\beta)$ in the equations 50 and 51 (pressure distribution in zone I) are defined as follows:

$$L_2(\beta) = \frac{4F_{gH}\phi\rho_H \alpha_{II} \mu R \beta}{km} \tag{S42}$$

$$M(\beta) = T_i + A_1 Ei\left(-b^2\right) \tag{S43}$$

$$N(\lambda) = \frac{Ei\left(-(a\lambda + b)^2\right)(a\lambda + b) - \sqrt{\pi} erf\,(a\lambda + b)}{a} \tag{S44}$$

$$K_1(\beta) = C + A_1 Ei\left(-b^2\right) \tag{S45}$$

Now, equation S31 by insertion of the resulted T_I and T_{II} formulas for both heat sources (equations 47 and 48) and considering equation 11 becomes:

- Line heat source:

$$\frac{ak_I(T_i - T_s)}{k_{II}(T_s - T_0)} \underbrace{\left(\frac{\exp(-(a\beta + b)^2)}{(a\beta + b)(Ei\left(-(a\beta + b)^2\right) - Ei\left(-b^2\right))} \right)}_{G_1(\beta)} + \underbrace{\left(\frac{\exp(-\beta^2)}{\beta Ei\left(-\beta^2\right)} \right)}_{H_1(\beta)} = \underbrace{\sqrt{\pi}\phi\rho_H \alpha_{II} \beta}_{I(\beta)} \frac{(c + dT_s)}{k_{II}(T_s - T_0)} \tag{S46}$$

- Wellbore heat source:

$$\frac{ak_I(T_i - T_s)}{k_{II}(T_s - T_0)} \underbrace{\left(\frac{-F \exp(-(a\beta + b)^2)}{(a\beta + b)(-FEi\left(-(a\beta + b)^2\right) + FEi\left(-b^2\right) - D_1 - E_1)} \right)}_{G_2(\beta)} + \underbrace{\left(\frac{\exp(-\beta^2)}{\beta Ei\left(-\beta^2\right)} \right)}_{H_1(\beta)} = \underbrace{\sqrt{\pi}\phi\rho_H \alpha_{II} \beta}_{I(\beta)} \frac{(c + dT_s)}{k_{II}(T_s - T_0)} \tag{S47}$$

So, the temperature at the interface based on the equations S46 and S47 for both heat sources is calculated as follows:

- Line heat source:

$$T_s = \frac{k_{II} T_0 H_1(\beta) - a k_I T_i G_1(\beta) + cI(\beta)}{-a k_I G_1(\beta) - dI(\beta) + k_{II} H_1(\beta)} \quad \text{(S48)}$$

- Wellbore heat source:

$$T_s = \frac{k_{II} T_0 H_1(\beta) - a k_I T_i G_2(\beta) + cI(\beta)}{-a k_I G_2(\beta) - dI(\beta) + k_{II} H_1(\beta)} \quad \text{(S49)}$$

From the equations 50 and 51, the pressure at the dissociation interface (P_s) for both heat sources would be:

- Line heat source:

$$P_s = \left(P_0^2 + L_2(\beta) M(\beta)\beta + A_1 L_2(\beta)(N(0) - N(\beta))\right)^{1/2} \quad \text{(S50)}$$

- Wellbore heat source:

$$P_s = \left(P_0^2 + L_2(\beta)(K_1(\beta)\beta - A_2 N(\beta) - (K_1(\beta)\lambda_{os} - A_2 N(\lambda_{os}))\right)^{1/2} \quad \text{(S51)}$$

Now, by inserting the equations S48-S51 in the equation 11 (Antoine equation), which is transformed to the following form (equation S52), then solving it to find β, the exact solution of temperature and pressure distributions will be achieved.

$$\frac{B_a}{A_a - \ln(P_s)} - T_s = 0 \quad \text{(S52)}$$

Actually, equation S52 has only one unknown at each time, which is β.

The equation of heat flux from the wellbore (equation 52) can be transformed to the following form based on the transformation term of equation 44:

$$u_r = \frac{-k_I}{\sqrt{4\alpha_{II} t}} \frac{dT_I}{d\lambda}, \ \lambda = \lambda_{os} \quad \text{(S53)}$$

By inserting T_I from equation 47 into equation S53:

$$u_r = \frac{2 a k_I A_2 \exp(-(a\lambda_{os} + b)^2)}{(a\lambda_{os} + b)\sqrt{4\alpha_{II} t}} \quad \text{(S54)}$$

The number of moles of produced gas at each time step should be calculated as follows in order to calculate the total volume of gas produced at STP conditions:

$$A_s = 2\pi(\frac{S_t + S_{t-1}}{2}) \quad \text{(S55)}$$

$$V_r = \phi\pi(S_t^2 - S_{t-1}^2) \quad \text{(S56)}$$

$$n_r = F_{gH}\rho_H V_r / (A_s m) \quad \text{(S57)}$$

Equation S55 shows the average surface area of the dissociation front at each time step (*t*-1, *t*), and equations S56 and S57 are respectively the volume of dissociated hydrate and the moles of produced gas per average surface area of the dissociation front at each time step (*t*-1, *t*). By summing the moles of produced gas at each time step from the beginning of dissociation to time *t*, the total number of moles of produced gas up to time *t* will be calculated as shown in equation S61.

$$n_{rt} = \sum_{t=0}^{t} n_r \quad \text{(S58)}$$

Finally, by using equations S58 and 5 the total volume of produced gas per average area of the dissociation front at STP conditions up to time *t* will be achieved as presented in equation 50.

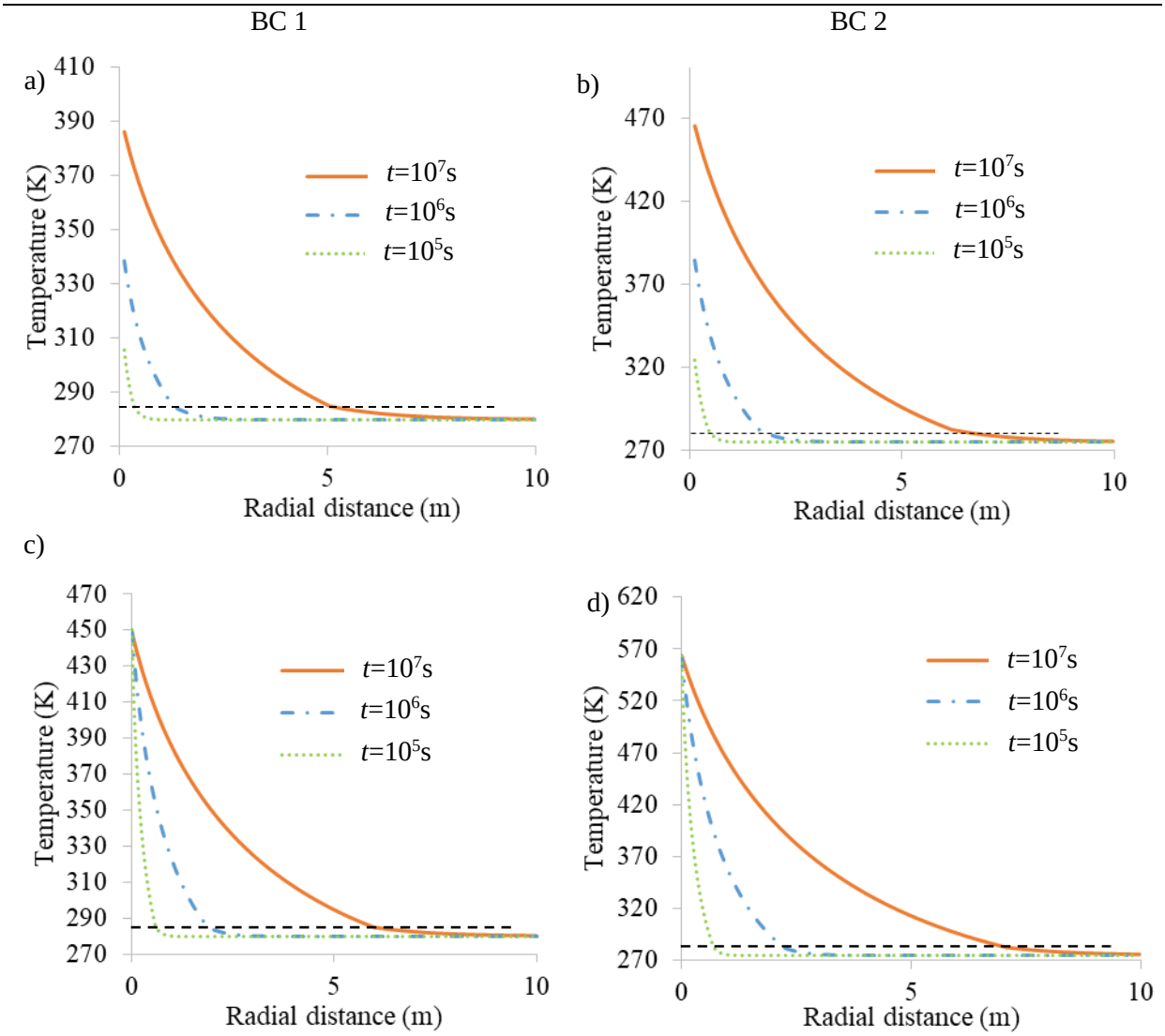

Figure S1. Temperature distribution for case 1 at different time frames for two initial and boundary conditions (BC 1: a and c, BC 2: b and d) considering a and b) wellbore heating, and c and d) Line heat source.

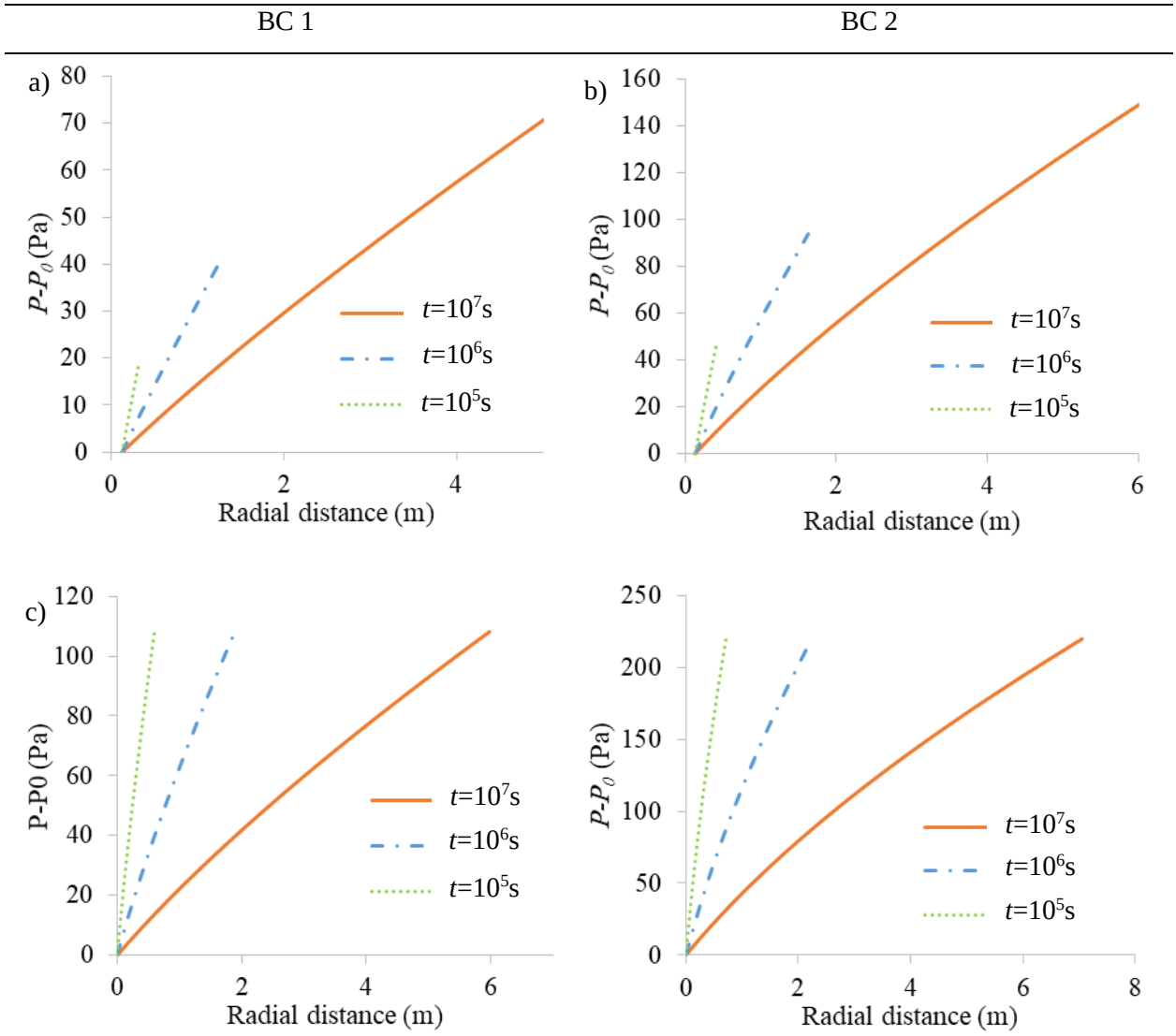

Figure S2. Pressure distribution for case 1 in the dissociated zone at different time frames for two initial and boundary conditions (BC 1: a and c, BC 2: b and d) considering a and b) wellbore heating, and c and d) Line heat source.

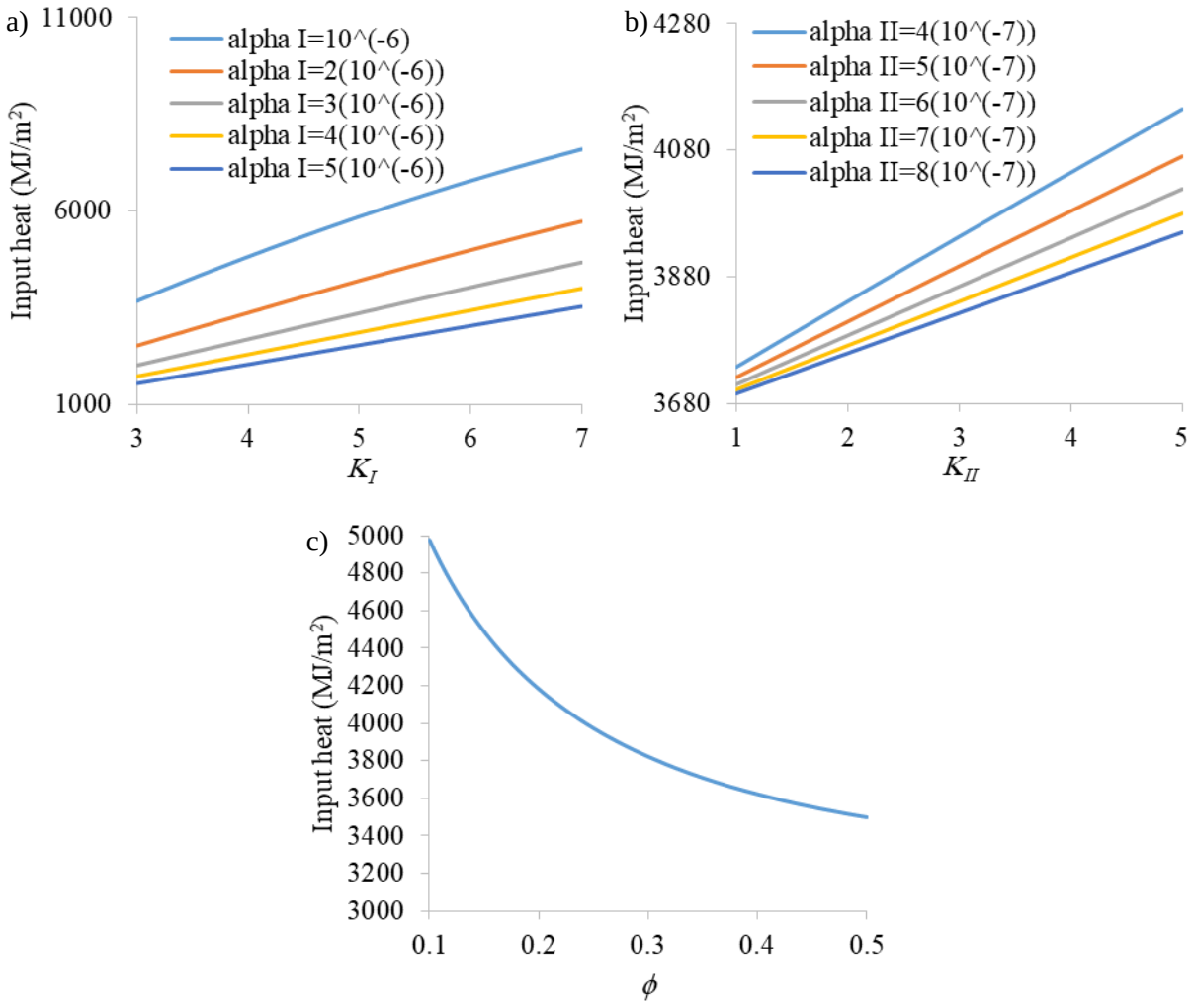

Figure S3. Input heat from the wellbore to the reservoirs after 100 days dissociation in the case with wellbore heating considering various parameters stated in Table 2: a) thermal diffusivity and thermal conductivity of Zone I, b) thermal diffusivity and thermal conductivity of Zone II, and c) various values of porosity with different permeabilities and different gas viscosities.

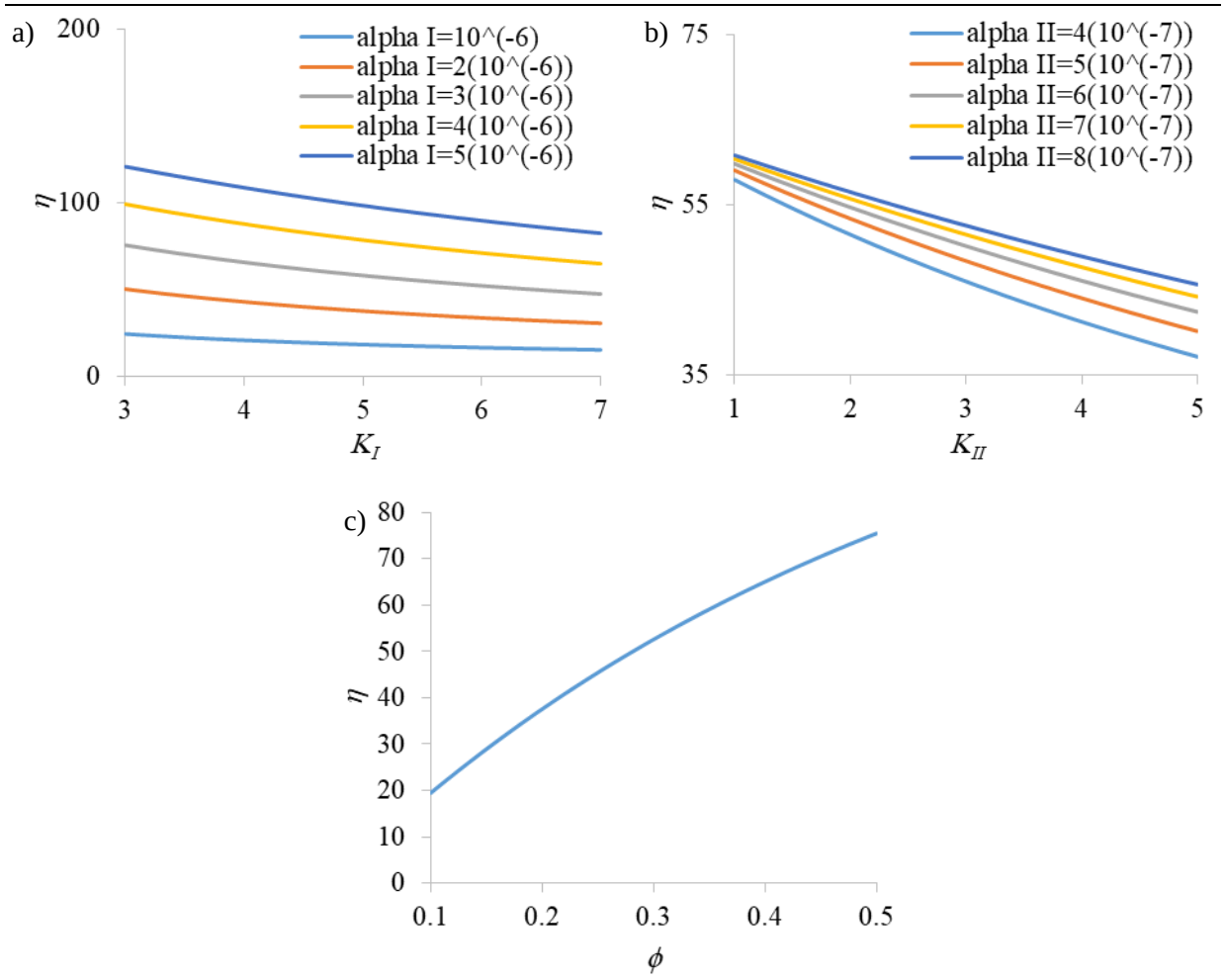

Figure S4. Energy efficiency of the dissociation after 100 days process in the case with wellbore heating considering various parameters stated in Table 2: a) thermal diffusivity and thermal conductivity of Zone I, b) thermal diffusivity and thermal conductivity of Zone II, and c) various values of porosity with different permeabilities and different gas viscosities.

Appendix C

In the following, the solution process of equations 71 and 72 is provided. This process is a little bit different for the two operation models. For the model in which the hot water is injected to the inner tube, T_{fa} is calculated first based on T_{fi} as follows:

$$T_{fa}(z,t) = R_1 C_f V_f \frac{\partial T_{fi}(z,t)}{\partial z} + T_{fi}(z,t) \tag{S59}$$

Then, by inserting equation S2 to equation 72, the resulted expression is:

$$R_1 R_2 (C_f V_f)^2 \frac{\partial^2 T_{fi}(z,t)}{\partial z^2} - R_1 C_f V_f \frac{\partial T_{fi}(z,t)}{\partial z} - T_{fi}(z,t) + T_I(r_7,t) \tag{S60}$$

Equation S60 is a second-order nonhomogeneous differential equation, which can be solved to obtain T_{fi} due to the following initial and boundary conditions: i) injection temperature is fixed and constant through the process ($T_{fi}(h,t)$); and ii) no heat flow occurs at the base of the wellbore ($T_{fi}(0,t) = T_{fa}(0,t) \rightarrow \frac{\partial T_{fi}(0,t)}{\partial z} = \frac{\partial T_{fa}(0,t)}{\partial z} = 0$).

For the other model of how water injection into the annulus, T_{fa} based on T_{fi} is as follows:

$$T_{fa}(z,t) = R_1 C_f V_f \frac{\partial T_{fi}(z,t)}{\partial z} + \frac{R_1}{R_2}(T_{fi}(z,t) - T_I(r_7,t)) + T_{fi}(z,t) \tag{S61}$$

Then, by inserting equation S61 to equation 72, the new expression based on T_{fi} is:

$$R_1 R_2 (C_f V_f)^2 \frac{\partial^2 T_{fi}(z,t)}{\partial z^2} + R_1 C_f V_f \frac{\partial T_{fi}(z,t)}{\partial z} - T_{fi}(z,t) + T_I(r_7,t) \tag{S62}$$

Equation S62 is also a second-order nonhomogeneous differential equation, and can be solved by the same procedure and with the same initial and boundary conditions as those of equation S60.

In the following, some of the transformations of the dissociation's fundamental equations with the initial and boundary conditions in terms of λ is the same as that of the previous part (Appendix B; Equations S29, and S31-S35) except the following equation.

Equation 73: $\frac{-k_I A_w}{\sqrt{4\alpha_{II} t}} \frac{dT_I}{d\lambda} = \frac{(\overline{T_{fa}(t)} - T_I)}{R_w}$, $\lambda = \lambda_{os}$ (S63)

The very small ratio of $\frac{\rho_g}{\rho_H}$ indicates the very slow rate of hydrate dissociation (dS/dt), which neglects the transient term in the continuity equation.

In the equations 73 and 74, A, A_1, B, B_1, and C constants are defined using equations S30 and 38 as follows:

$$A_3 = \frac{(T_s - \overline{T_{fa}(t)})F}{-FEi(-(a\beta+b)^2) + FEi(-b^2) + D_2 + E_1} \quad \text{(S64)}$$

$$B_3 = \frac{A_3(D_2 + E_2)}{F} + \overline{T_{fa}(t)} \quad \text{(S65)}$$

$$C_1 = \frac{T_s(t) - T_0}{Ei(-\beta^2)} \quad \text{(S66)}$$

, where D_2 is as follows:

$$D_2 = \frac{-r_7 k_I \, 2a \exp(-(a\lambda_{os} + b)^2)}{e\sqrt{\pi}} \quad \text{(S67)}$$

The $L_3(\beta)$ and $K_2(\beta)$ functions used in equation 40 (pressure distribution in zone I) are as follows:

$$L_3(\beta) = \frac{4F_{gH}\phi\rho_H\alpha_{II}\mu R\beta}{km} \quad \text{(S68)}$$

$$K_2(\beta) = B_3 + A_3 Ei(-b^2) \quad \text{(S69)}$$

Now, equation S31 by insertion of the resulted T_I and T_{II} formulas and considering equation 11 becomes:

$$\frac{ak_I(\overline{T_{fa}(t)} - T_s(t))}{k_{II}(T_s(t) - T_0)} \underbrace{\left(\frac{-F\exp(-(a\beta+b)^2)}{(a\beta+b)(-FEi(-(a\beta+b)^2) + FEi(-b^2) - D_2 - E_1)} \right)}_{G_3(\beta)} + \underbrace{\left(\frac{\exp(-\beta^2)}{\beta Ei(-\beta^2)} \right)}_{H_1(\beta)} = \underbrace{\sqrt{\pi}\phi\rho_H\alpha_{II}\beta}_{I(\beta)} \frac{(c + dT_s(t))}{k_{II}(T_s(t) - T_0)} \quad \text{(S70)}$$

So, the temperature at the dissociation interface based on equation S70 can be calculated as follows:

$$T_s(t)=\frac{k_{II}T_0H_1(\beta)-ak_I\overline{T_{fa}(t)}G_3(\beta)+cI(\beta)}{-ak_IG_3(\beta)-dI(\beta)+k_{II}H_1(\beta)} \quad \text{(S71)}$$

The pressure at the dissociation interface (P_s) would be calculated from the equation 76:

$$P_s(t)=\left(P_i^2+L_3(\beta)(K_2(\beta)\beta-A_3N(\beta)-(K_2(\beta)\lambda_{os}-A_3N(\lambda_{os})))\right)^{1/2} \quad \text{(S72)}$$

The following equation is a transformation of equation 11 (Antoine equation):

$$\frac{B_a}{A_a-\ln(P_s)}-T_s=0 \quad \text{(S73)}$$

Then, by replacing T_s and P_s in equation S73 with the equations S71 and S72, and solving the resulted expression to find β, the exact solution of temperature and pressure distributions will be achieved. Actually, at each time step, equation S73 has only one unknown, which is β.

The transformed form of equation of heat flux from the wellbore (equation 77) based on the transformation term of equation 44 is:

$$u_r=\frac{-k_I}{\sqrt{4\alpha_{II}t}}\frac{dT_I}{d\lambda},\ \lambda=\lambda_{os} \quad \text{(S74)}$$

By inserting T_I from equation 73 into equation S74:

$$u_r=\frac{2ak_IA_3\exp(-(a\lambda_{os}+b)^2)}{(a\lambda_{os}+b)\sqrt{4\alpha_{II}t}} \quad \text{(S75)}$$

In order to obtain the total volume of gas produced at STP conditions, the produced gas moles at each time step should be calculated. Equations S76 and S77 show respectively the volume of dissociated hydrate and the moles of produced gas per average surface area of the dissociation front at each time step (t-1, t) as shown in equation S76.

$$A_s=2\pi\left(\frac{S_t+S_{t-1}}{2}\right) \quad \text{(S76)}$$

$$V_{rp}=\phi h\pi(S_t^2-S_{t-1}^2) \quad \text{(S77)}$$

$$n_r=F_{gH}\rho_HV_{rp}/(A_sm) \quad \text{(S78)}$$

, where h is the methane hydrate thickness (m). By summing the moles of produced gas at each time step from the beginning of dissociation to time t as shown in equation S79, the total number of moles of produced gas up to that time can be calculated.

$$n_{rt} = \sum_{t=0}^{t} n_r \tag{S79}$$

Finally, by using equations S80 and 5 the total volume of produced gas per average area of the dissociation front at STP conditions up to time t can be achieved as presented in equation 79.

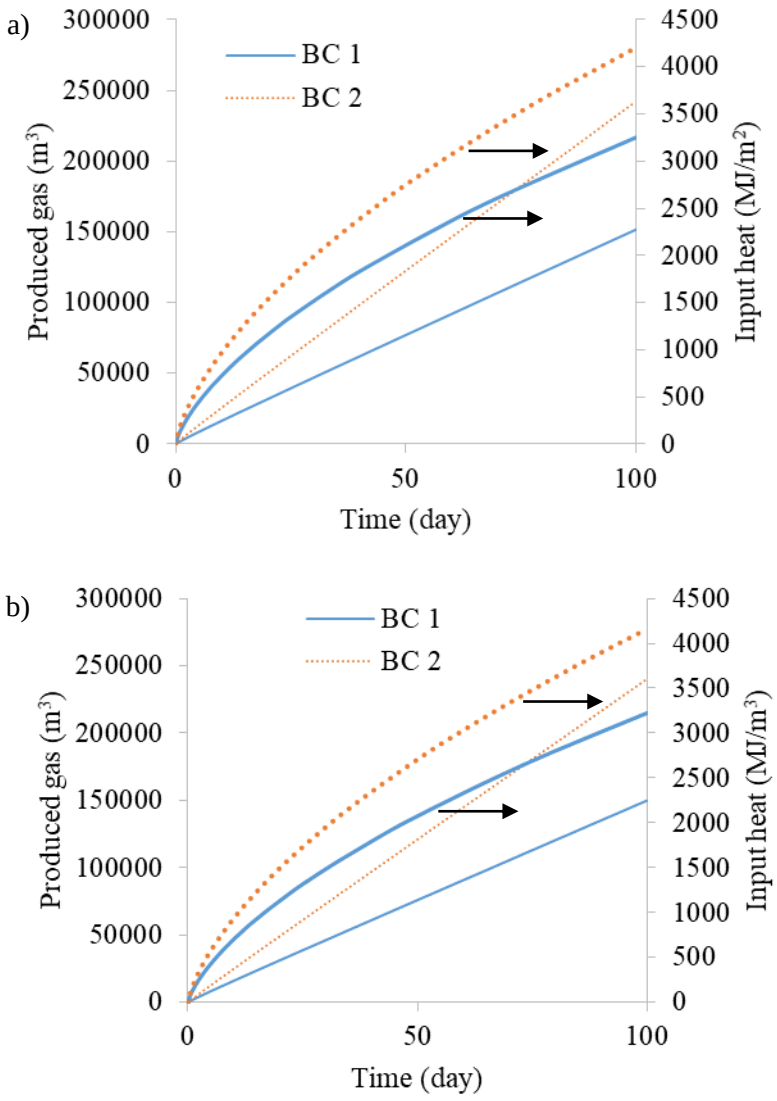

Figure S5. Volume of produced gas and the input heat from the wellbore in the model with hot water injection into the a) annulus and b) inner tube during hydrate dissociation for two BCs. The thicker lines represent the input heat from the wellbore.

a)

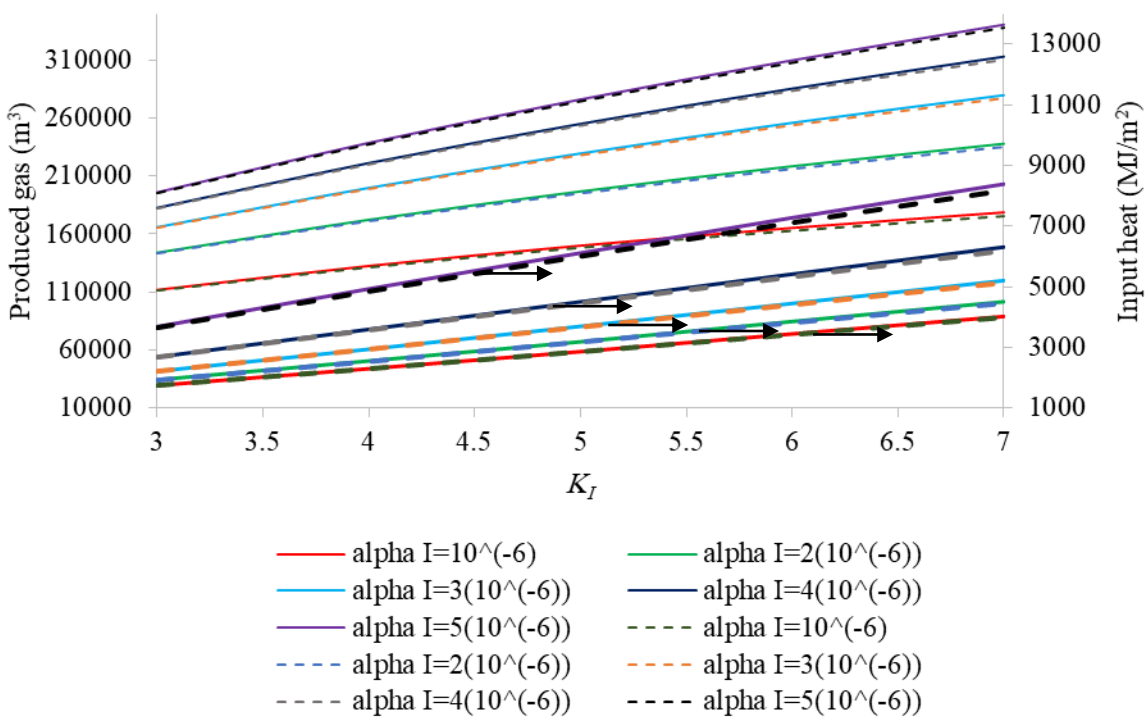
Produced gas (m3)
Input heat (MJ/m2)
KI
alpha I=10^(-6)
alpha I=2(10^(-6))
alpha I=3(10^(-6))
alpha I=4(10^(-6))
alpha I=5(10^(-6))
alpha I=10^(-6)
alpha I=2(10^(-6))
alpha I=3(10^(-6))
alpha I=4(10^(-6))
alpha I=5(10^(-6))

b)

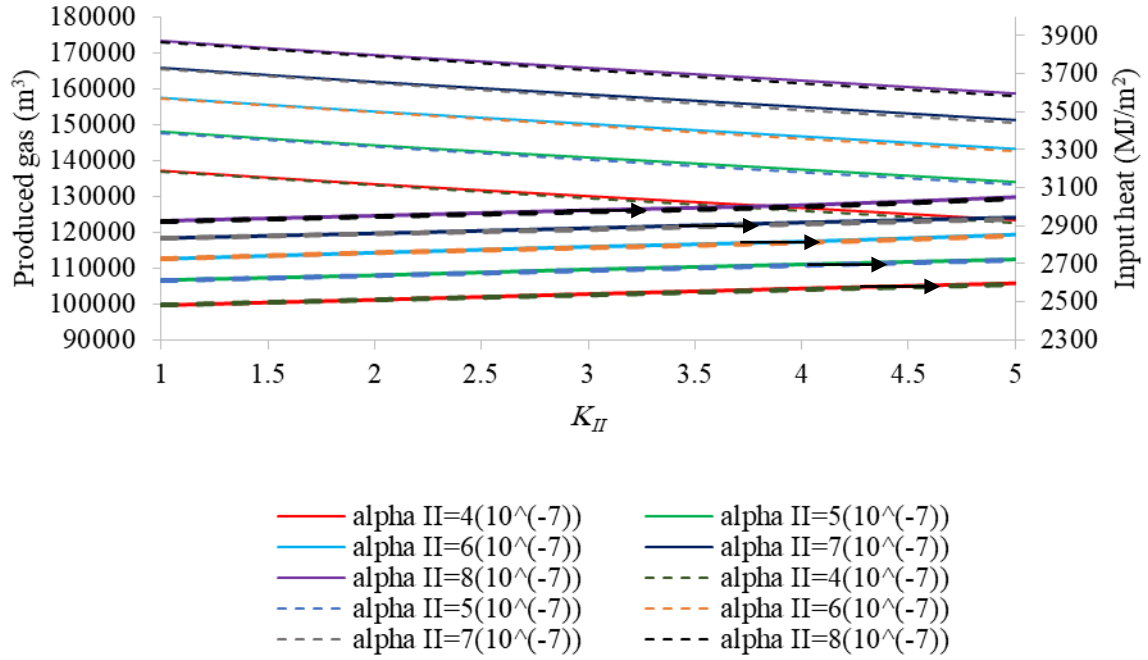
Produced gas (m3)
Input heat (MJ/m2)
KII
alpha II=4(10^(-7))
alpha II=5(10^(-7))
alpha II=6(10^(-7))
alpha II=7(10^(-7))
alpha II=8(10^(-7))
alpha II=4(10^(-7))
alpha II=5(10^(-7))
alpha II=6(10^(-7))
alpha II=7(10^(-7))
alpha II=8(10^(-7))

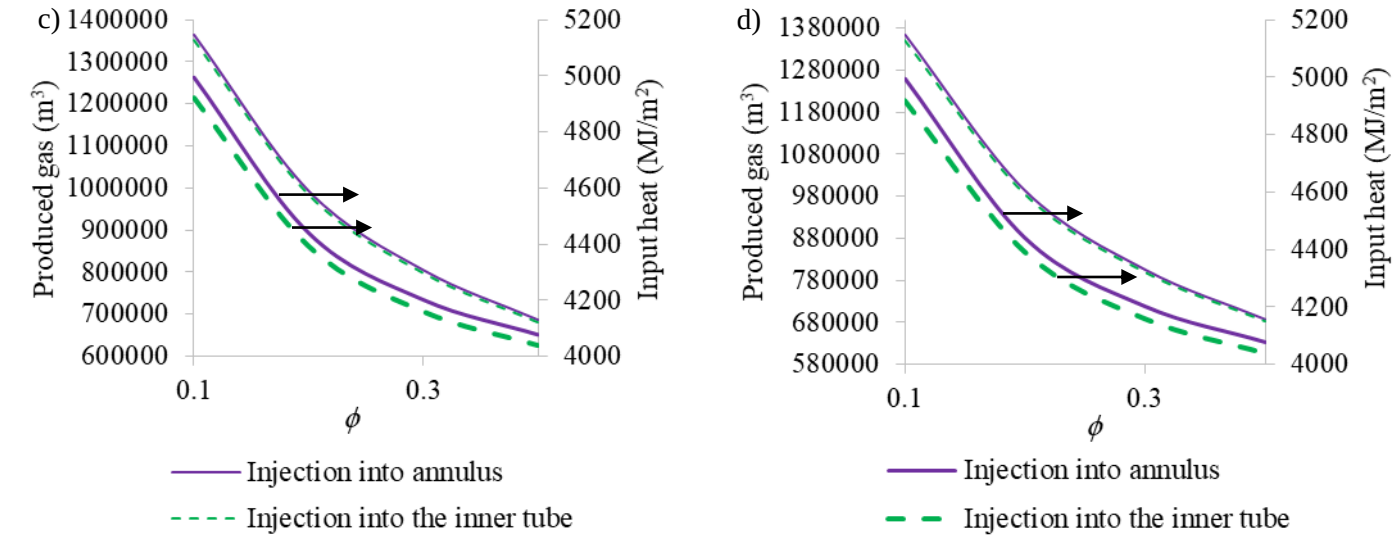

Figure S6. The effect of various parameters on the produced gas and the input heat from the wellbore after 100 days dissociation considering both operating schemes: a) thermal diffusivity and thermal conductivity of Zone I, b) thermal diffusivity and thermal conductivity of Zone II, c) porosity with various permeabilities, and d) porosity with various gas viscosities.

Dashed lines and solid lines are respectively representative of the operating schemes of hot water injection into annulus and into the inner tube. The thicker lines represent the input heat from the wellbore.

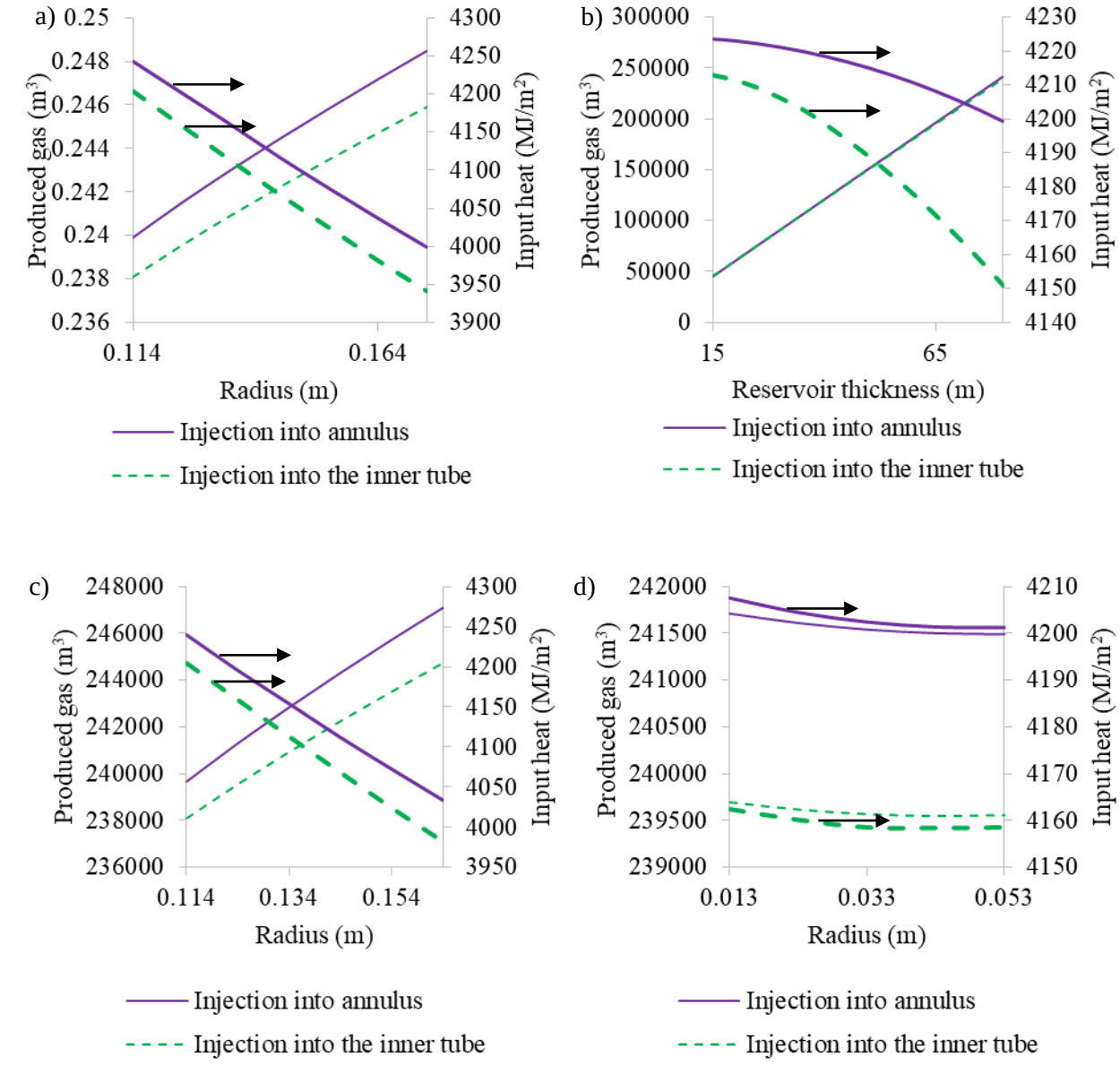
a)
Produced gas (m3)
Input heat (MJ/m2)
0.25
0.248
0.246
0.244
0.242
0.24
0.238
0.236
4300
4250
4200
4150
4100
4050
4000
3950
3900
0.114
0.164
Radius (m)
Injection into annulus
Injection into the inner tube
b)
Produced gas (m3)
Input heat (MJ/m2)
300000
250000
200000
150000
100000
50000
0
4230
4220
4210
4200
4190
4180
4170
4160
4150
4140
15
65
Reservoir thickness (m)
Injection into annulus
Injection into the inner tube
c)
Produced gas (m3)
Input heat (MJ/m2)
248000
246000
244000
242000
240000
238000
236000
4300
4250
4200
4150
4100
4050
4000
3950
0.114
0.134
0.154
Radius (m)
Injection into annulus
Injection into the inner tube
d)
Produced gas (m3)
Input heat (MJ/m2)
242000
241500
241000
240500
240000
239500
239000
4210
4200
4190
4180
4170
4160
4150
0.013
0.033
0.053
Radius (m)
Injection into annulus
Injection into the inner tube

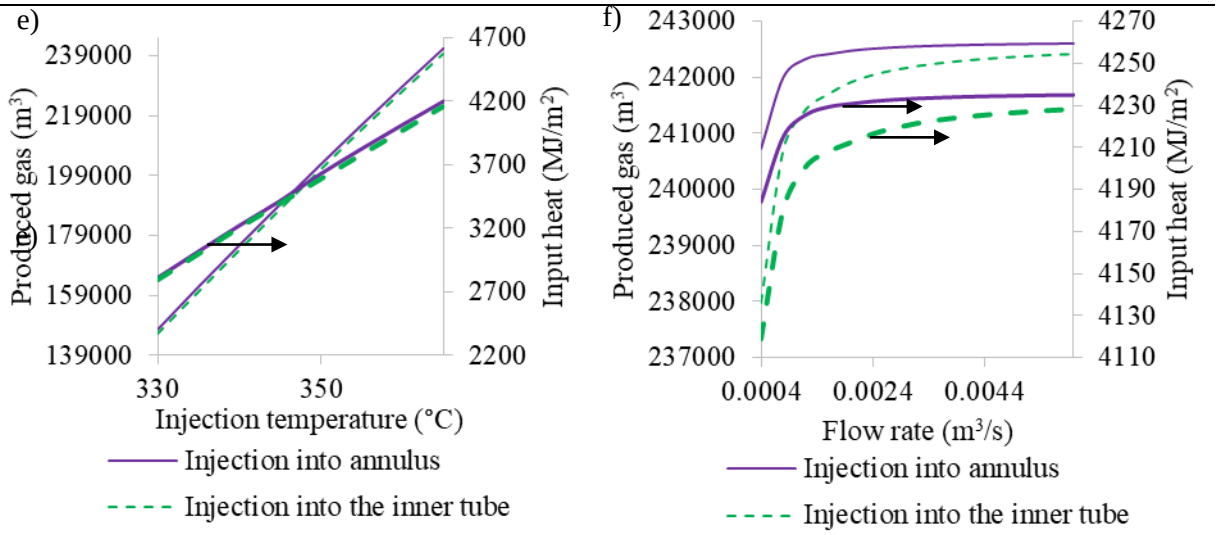

Figure S7. The effect of various parameters on the produced gas and the input heat from the wellbore after 100 days dissociation considering both operating schemes: a) the wellbore radius, b) the reservoir thickness, c) the annulus radius, d) the inner tube radius, e) the injection temperature, and f) the flow rate.

Dashed lines and solid lines are respectively representative of the operating schemes of hot water injection into annulus and into the inner tube. The thicker lines represent the input heat from the wellbore.